## DAMPING OF ELECTROMECHANICAL OSCILLATIONS IN WIDE-AREA POWER SYSTEMS SUCH AS THE TRANS-CANADIAN GRID

#### HAMED GOLESTANI FAR



Department of Electrical and Computer Engineering
McGill University
Montréal, Québec, Canada
March 2010

A thesis submitted to McGill University in partial fulfillment of the requirements for the degree of Doctor of Philosophy in Electrical Engineering

#### **Abstract**

This thesis presents two methods to damp electromechanical oscillations in large power systems such as Trans-Canadian grid. A control method, used in conjunction with Wide Area Measurement System (WAMS), is proposed to damp very low frequency inter-area modes of very large systems. This Global PSS requires knowledge of the eigenvectors of the targeted modes, and only a limited number of power stations are involved in its feedback loop. It does not destabilize other modes, and its robustness is assured. Besides mathematical proof, a series of simulations are conducted to validate the claims of the proposed Global PSS. The second solution is based on fast controllability of Voltage Source Converters (VSCs) connecting Renewable technologies to the power system. In this method, their injected Active and Reactive powers are modulated to improve power system damping. Mathematical formulations are developed to study the effectiveness of damping in relation to injection point along the transmission line. Taking nonlinearity, due to limit on active/reactive output power, into account, trade-offs of feedback gain constants with respect to saturation limits are studied. Phase-plane diagrams give clear picture of this nonlinearity, and simulation results confirm how high damping can be secured.

#### Résumé

Cette présente deux méthodes amortir les oscillations pour électromécaniques dans les grands réseaux électriques tel que le réseau transcanadien. Une méthode de contrôle, utilisé avec un système étendu de measures (Wide Area Measurement System), est proposée pour amortir de très basses fréquences intermodes des très grands réseaux. Ce PSS global exige la connaissance des vecteurs propres des modes ciblés, et seulement un nombre limité de stations d'alimentation sont impliquées dans la boucle de rétroaction. Il ne déstabilise pas les autres modes, et sa robustesse est assurée. En plus de preuves mathématiques, des simulations sont effectuées pour valider les affirmations du PSS global proposé.

La deuxième solution est basée sur la contrôlabilité rapide des convertisseurs à source de tension (Voltage Source Converter) reliant les technologies à énergie renouvelable aux réseaux électriques. Dans cette méthode, l'injection de puissance active et réactive est modulée pour améliorer l'amortissement du réseau électrique. Des formulations mathématiques sont développées pour étudier l'efficacité de l'amortissement en lien avec les points d'injections le long des lignes de transmission. En prenant compte des non-linéarités, causées par la limite d'injection de puissance active/réactive, les compromis pour les gains de rétroaction en rapport avec les limites de saturations sont étudiés. Des diagrammes de plan de phase donnent une illustration claire de cette non-

linéarité et des résultats de simulations confirment comment un amortissement élevé peut être sécurisé.

#### Acknowledgements

I would like to express my sincere gratitude towards my supervisor, Professor Boon-Teck Ooi for his supervision, guidance, encouragement and kindness during the course of this research. His unique approach to research provides deep understanding of the problem, and extends student's limits in finding the solution.

I express my thanks and appreciation to Prof. F.D. Galiana and Prof. Ooi for providing financial support through Natural Sciences and Engineering Research Council of Canada (NSERC) grant. I would also like to thank other member of my committee Prof. Michalska.

Special thanks to Dr. Hadi Banakar. I am forever indebted to him for his guidance, encouragement and kindness.

Thanks to Prof. Louis-A. Dessaint for providing access to Hypersim in École de technologie supérieure (ÉTS).

Thanks to all the professors in Power research group, Profs. F.D. Galiana, Prof. Boon-Teck Ooi, and Prof. Geza Joos. Finally, thank to all my friends in Power research group for their helpful feedback and support. Also, I would like to express my extended and special thanks to my family for their support, understanding and patience.

#### Table of Contents

AbstractI
RésuméII
AcknowledgementsIV
Table of Contents V
Table of FiguresXI
List of TablesXV
NomenclatureXVI
CHAPTER 1- Inroduction
1.1 Introduction
1.1.1 Background on Definition of Thesis Topic
1.1.2 Review on Electromechanical Oscillations in Power System 4
1.2 Methodologies of Research
1.2.1 Function Analysis
1.2.2 Eigenfunctions
1.2.3 Numerical Analysis
1.2.4 Phase-Plane Method
1.3 Organization of Thesis
CHAPTER 2- Damping Inter-area oscillations by Multiple Modal Selectiv-
ity Method14
2.1 Introduction

2.2	Background	.16
2.2.1	Dynamics of Linear Systems	.16
2.2.2	Modal Analysis [63, 66]	.18
2.2.3	Linear feedback	.19
2.3	Method of Multiple Modal Selectivity	.21
2.3.1	Perfect Decoupling	.21
2.3.2	Practical Case	.22
2.3.3	Negative Real Numbers for Diagonal Elements	.23
2.4	Test System Modal Properties	.24
2.4.1	Test Power System	.25
2.4.2	Open Loop Properties	.27
2.4.3	Mode Shapes of Right Eigenvectors	.29
2.4.4	Mode Shapes of Left Eigenvectors	.29
2.4.5	Implementing Linear Independence	.29
2.5	Implementation	.31
2.5.1	Imposed Requirements	.31
2.5.2	Control Center Level Implementation	.33
2.5.3	Plant Level Implementation	.34
2.6	Selection of Controlling Generators	.35
2.6.1	Maximizing Damping	.35
2.6.2	Maximizing Decoupling	.35

2.7 Co	nclusion37
CHAPTER	3- Multiple Modal Selectivity Method: Test Results38
3.1 Int	roduction39
3.1.1	Γests of Multiple Selectivity39
3.1.2	Γests on Robustness39
3.2 Res	sults from Numerical Tests40
3.2.1 S	Simulations – No Decoupling40
3.2.2 H	Eigenvalue Evaluation – No Decoupling42
3.2.3 S	Simulations – With Decoupling43
3.3 Per	rformance on Power Systems with Realistically Modeled Gener-
ators	
3.3.1	Γests on a16-machine 68-bus System (Eigen-analysis)44
3.3.2	Γest by 4-Generator System (Time-domain Simulation)46
3.4 Ro	bustness of the Method48
3.4.1 S	Sensitivity of Mode Shapes to a disconnected local line50
3.4.2 S	Sensitivity of Mode Shapes to disconnected tie-line51
3.4.3	Γime Domain Proof of Robustness51
3.4.4 H	Proof by Eigenvalue Evaluations56
3.5 Con	nclusion57
9 K 1 T	Dahuatnasa 57

CHAPTER 4- Damping Capability of Renewable Rnergies as Affected by
Point of Insertion58
4.1 Introduction
4.2 Complex Power Load In Transmission Line63
4.2.1 Dynamic Equation of System64
4.3 Phase Plane Method67
4.3.1 Phase-Plane Diagram68
4.3.2 System without Damping69
4.3.3 Limit Cycles
4.3.4 Unstable Operating Region
4.4 Concept of Nonlinear Damping70
4.4.1 Damping by Modulating Active Power70
4.4.2 Damping by Modulating Reactive Power
4.5 Dependence on Location in Transmission Line
4.5.1 Dependence of Damping on "r"73
4.5.2 Active Power Modulation74
4.5.3 Reactive Power Modulation76
4.6 Conclusion
CHAPTER 5- Nonlinear Damping of Nonlinear Oscillations by Renewable
Γechnologies80
5.1 Introduction 91

5.2 Damping by A Mix of Linear and Nonlinear Feedback	.83
5.2.1 MVA Rating Constraints on Linear Control	.83
5.2.2 Linear Control with "Saturation Blocks"	84
5.3 Bang-bang Nonlinear Damping	84
5.3.1 Limit Cycles	86
5.3.2 Nonlinear Damping of Limit Cycles	87
5.3.3 Validation of Nonlinear Damping Theory	.88
5.3.4 Comparison with Linear Damping	90
5.4 Further Proof of Principle by Simulation	92
5.4.1 Test Conditions	.92
5.4.2 Tests on Active Power Modulation	92
5.5 Non-Electrical Engineering Limits	.97
5.5.1 Limits from Wind-Turbine Manufacturers	97
5.6 Conclusions	99
CHAPTER 6- Summary and Conclusions	.01
6.1 Introduction	.02
6.2 Conclusions of Thesis	.03
6.2.1 Chapter 2	.05
6.2.2 Chapter 3	.06
6.2.3 Chapter 4	.06
6.2.4 Chapter 5	.06

6.3	Future Work	107
Append	lix	108
Appe	endix A: Investigation on Generator Modeling	108
Appe	endix B: Information regarding Validation Test	117
Referen	.ces	119

#### Table of Figures

Figure 2.1 Power System one-line diagram
Figure 2.2 Mode shapes of the sub-matrix $[A_{12}]$ right eigenvectors
<b>Figure 2.3</b> Graphical interpretations of operations $v_1^T u_1$ , $v_2^T u_1$ and $v_9^T u_1$ 30
Figure 2.4 Feedback Loop in Central Control
Figure 2.5 Graphical depiction of terms defining decoupling conditions
Figure 3.1 Modal responses following excitation of all modes for power stations
$\{5,8,11\}$ . No decoupling in targeted slow modes
Figure 3.2 Response of slow modes #1, #2, #3 for excitation of mode #3. Left—
no decoupling $\{5,8,11\}$ ; Right—with decoupling $\{2,5,8,11\}$
Figure 3.3 Mode shapes of three lowest frequencies
Figure 3.4 Electromechanical eigenvalues
<b>Figure 3.5</b> Four-Generator System [71, 73]
Figure 3.6 Simulation of pu speed of G3 after occurrence and clearing of three
phase ground fault
Figure 3.7 Shapes of low frequency modes: (a) intact system; (b) one open local
line)
Figure 3.8 Slow modes damped by Multiple Selectivity Control: (a)Intact system
(b)System with disconnected local line
<b>Figure 3.9</b> Shapes of low frequency modes: (a) intact system; (b) open $1^{st}$ tie-line)
52

Figure 3.10 Slow modes damped by Multiple Selectivity Control: (a)Intact
system (b)System with 1 <sup>st</sup> tie-line disconnected
Figure 3.11 Shapes of low frequency modes: (a) intact system; (b) open $2^{nd}$ tie-
line)53
Figure 3.12 Slow modes damped by Multiple Selectivity Control: (a) Intact
system (b) System with 2 <sup>nd</sup> tie-line disconnected
Figure 3.13 Shapes of low frequency modes: (a) intact system; (b) open 3 <sup>rd</sup> tie-
line)
Figure 3.14 Slow modes damped by Multiple Selectivity Control: (a) Intact
system (b) System with 3 <sup>rd</sup> tie-line disconnected
Figure 3.15 Shapes of low frequency modes: (a) intact system; (b) open 4 <sup>th</sup> tie-
line)
Figure 3.16 Slow modes damped by Multiple Selectivity Control: (a) Intact
system (b) System with 4 <sup>th</sup> tie-line disconnected
Figure 3.17 Slow modes Comparison of eigenvalues of 3 slow modes—intact
system with system with disconnected tie-line (4 cases)
Figure 4.1 2500-second simulation of wind farm, from [82]: (a) wind velocity; (b)
wind farm (24 WTGs) output
Figure 4.2 Auxiliary Power for Damping, from [82]: (a) wind farm power output;
(b) pitch angle of turbine blade; (c) damping power from individual WTG 61
<b>Figure 4.3</b> Complex Power Load at distance $rL$ from $G1$ , $0 < r < 1.0.$

Figure 4.4 Phase-plane representation of Undamped System
Figure 4.5 Phase-plane: damping by $\Delta P_C = K_P \omega_{1-2}$ , $K_P = 10$
<b>Figure 4.6</b> Location Factors (a) $1/S_{1-2}$ , (b) $[(X_2/X_1)-(X_1/X_2)]/S_{1-2}$ 74
<b>Figure 4.7</b> Dependence of $-\sigma_p$ on " $r$ " and $P_1$ ( $P_{C0}$ =-0.2 pu, $Q_{C0}$ =0.0, $ K_p $ =20)75
Figure 4.8 Dependence of $-\sigma_P$ on " $r$ " and $P_{C0}$ (wind farm). ( $P_I$ =0.8 pu, $Q_{C0}$ =0.0
pu, $ K_p =20$ )
<b>Figure 4.9</b> $-\sigma_Q$ as a function of "r" and $P_1(P_{CO}=0.24 \text{ pu}, Q_{CO}=0 \text{ pu}, K_Q=20) \dots 77$
Figure 4.10 $-\sigma_Q$ as a function of "r" and $P_{C\theta}$ (wind farm power), (P1=0.8 pu,
$Q_{C_0}=0 \text{ pu}, \ K_Q=20)$ 77
Figure 5.1 (a) composite phase-plane diagram; (b) regions of no damping; (c)
region of heavy damping
<b>Figure 5.2</b> Oscillation of $\omega_{_{I-2}}$ under Nonlinear Damping by Active Power: $\Delta P_{_{\rm C}}$ =
20, 40, 60, and 80MW
<b>Figure 5.3</b> Oscillation of $\omega_{{}^{1-2}}$ under Nonlinear Damping by Reactive Power $\Delta Q_C$
60, 80, 100, 120 MVAR
<b>Figure 5.4</b> Inverse damping time-vs- $\Delta P_C$ or $\Delta Q_C$
<b>Figure 5.5</b> $\omega_{l-2}$ -vs- $\delta'_{l-2}$ the angular distance, under Linear Gain, $K_p = 20, 40, 60,$
and 80
Figure 5.6 Location r=0.0. Damping from active power modulation (a) phase-
plane; (b) frequency deviation; (c) renewable energy active power93

Figure 5.7 Location r=0.667. Damping from active power modulation (a) phase-
plane; (b) frequency deviation; (c) wind farm active power
Figure 5.8 Location r=0.667 (electrical midpoint). Damping from reactive power
modulation(a)phase plane;(b)frequency deviation;(c)renewable technology
reactive power
<b>Figure 5.9</b> Active power modulation. r=0.0, $K_P = 100$ : (a) frequency deviation; .97
Figure 5.10 Active power modulation of Figure 5.9 added to damping of PSS98
Figure 5.11 Reactive power modulation of Figure 5.8 added to damping of PSS.
99
Figure A.1 Mode shapes corresponding to $f_1$ =0.54 Hz (RR case)
Figure A.2 Mode shapes corresponding to $f_2=1.14$ Hz (RR case)
Figure A.3 Mode shapes corresponding to $f_3$ =1.18 Hz (RR case)
Figure A.4 Mode shapes corresponding to $f_1$ =0.54 Hz (SP case)
Figure A.5 Mode shapes corresponding to $f_2=1.14$ Hz (SP case)
Figure A.6 Mode shapes corresponding to $f_3$ =1.18 Hz (SP case)
Figure B.1 Block diagram of S-Modulator

#### <u>List of Tables</u>

Table 2.1	Power system load and generation data	. 26
Table 2.2	Lines' connectivity and per-unit reactances	. 26
Table 2.3	Modal frequencies and their classification	. 27
Table 3.1	System closed loop eigenvalues ( $\sigma_1 = \sigma_2 = \sigma_3 = -5$ )	. 42
Table A.1		109
Table B.1	Generator parameters	117
Table B.2	Generation and Load powers	117

#### Nomenclature

 $\Delta\omega_{i}$  Rotor speed deviation of synchronous machine i

 $\Delta \delta_i$  Angle deviation of synchronous machine i

 $\omega_i$  Rotor speed of synchronous machine i

 $\delta_i$  Rotor angle of synchronous machine i

 $\omega_{_{S}}, \omega_{_{0}}$  Synchronous speed

 $H_i$  Inertia constant of machine i

 $P_{ei}$  Electrical power of machine i

 $P_{mi}$  Mechanical power of machine i

 $\lambda_i$  i<sup>th</sup> eigenvalue of state matrix [A]

 $\underline{u}_{i}$  i<sup>th</sup> right eigenvector of state matrix [A]

 $\underline{\underline{v}}_i$  i<sup>th</sup> left eigenvector of state matrix [A]

 $\underline{y}$  Output vector

 $\underline{z}$  Input vector

[A] State matrix

[B] Input matrix

[C] Output matrix

[K] Gain matrix

 $-\sigma_k$  Damping coefficient for k<sup>th</sup> mode

 $\omega_{\mathbf{k}}$  Speed of  $\mathbf{k}^{\mathrm{th}}$  mode

 $f_k$  Frequency of  $k^{th}$  mode

 $P_{gi}$  Generated power at bus i

 $P_{di}$  Consumed power at bus i

X Inductive reactance of the line

 $P_{\scriptscriptstyle C}$  Real part of complex load

 $Q_{\mathbb{C}}$  Imaginary part of complex load

 $X_T$  Transformer reactance

 $X_L$  Line reactance

V Magnitude of voltage

 $K_P$  Active power modulation gain

 $K_{O}$  Reactive power modulation gain

 $\sigma_{\scriptscriptstyle P}$  Damping factor from active power modulation

 $\sigma_{\scriptscriptstyle Q}$  — Damping factor from Reactive power modulation

r Distance coefficient

 $S_{rating}$  MVA rating of installed renewable technology

 $P_{{\scriptscriptstyle C.upper}}$  Upper limit of active power

 $P_{C.lower}$  Lower limit of active power

 $P_{co}$  Steady-state active power output of complex load

 $Q_{co}$  Steady-state reactive power output of complex load

 $\Delta P_C$  Modulated active power

 $\Delta Q_C$  Modulated reactive power

 $\Delta Q_{CLIMT}$  Maximum limit of modulated reactive power

 $t_o$  Initial time

 $t_{\scriptscriptstyle f}$  Final time

$\Psi_f$	Field winding flux linkage
$\Psi_d$	Direct axis airgap flux linkage
$\Psi_{kq1}$	First quadrature axis damper winding flux linkage
$\Psi_{kq2}$	Second quadrature axis damper winding flux linkage

 $_{\text{CHAPTER}}\,1$ 

#### INTRODUCTION

#### 1.1 Introduction

#### 1.1.1 Background on Definition of Thesis Topic

This thesis is one of the deliveries of the NSERC Strategic Projects Grant under the title, "Design and Operation Trans-Canadian Power Grids: An Integrated Approach". Professor F.D. Galiana, who is the Principal Investigator, is addressing the Long-term Expansion Planning and Medium-Term Planning Issues and potential benefits. Team member, Professor B.T. Ooi, is responsible for doing research to forestall technical problems which can arise in the Trans-Canadian Grid. The specific problem, assigned to the author of this thesis, is instability associated with electromechanical oscillations. The subject is narrowed further because of consideration to past experience.

#### 1.1.1.1 Status of Power Electronics Research

The power electronics group of Power Energy Research Laboratory has researched on high voltage DC transmission (HVDC), Flexible AC Transmission Systems (FACTS) and Wind Energy. According to Professor B.T. Ooi, each provincial utility can retain the strength of a small system if the interconnections to form the large Trans-Canadian grid are by DC transmission or by back-to-back DC stations, however, they are expensive. Although controllers of Flexible AC Transmission Systems (FACTS), such as the Unified Power Flow Controller (UPFC) and the Static Synchronous Series Compensator (SSSC), are relatively

cheaper, they can also provide decoupling of neighbouring grids. As DC transmission is still an expensive technology, the future Trans-Canadian grid is most likely to be predominantly AC. Such a Trans-Canadian grid can be confronted by lowly damped or even negatively damped electromechanical oscillations; therefore Professor B.T. Ooi has defined instability of AC systems to be the focus of this thesis.

#### 1.1.1.2 NSERC's Suggestion

As suggested to the grantees by NSERC, besides linking the existing provincial power grids and evaluating the economic benefits, desirably the research should also address integrating sustainable energy resources.

#### 1.1.1.3 Status of Wind Power Research

The research group in wind energy of the Power Energy Research Laboratory has advanced to the stage where besides controlling arrays of wind-turbine generators to increase wind power penetration, the complex power outputs can be modulated to improve the dynamic performance of the grid. Since damping of electromechanical oscillations require complex power sources, utilizing wind farms to provide damping dovetails neatly to the long term research program, besides meeting NSERC's wishes.

#### 1.1.2 Review on Electromechanical Oscillations in Power System

Oscillation problems in power system are not new to the electric industry, and they were reported and investigated as early as 1920s [1]. As synchronous generators have very little damping, amortisseur windings were invented to provide damping. Using voltage regulators contributed in steady-state stability [2], and transient stability was improved through the use of high-speed fault clearing and high response exciters. In the early history of electrical engineering, synchronous generators formed small power systems to serve regional loads. A small system is considered to be "strong", because it has large synchronizing power with high frequency electromechanical oscillations. As local power systems interconnect, usually with long ac transmission lines, the synchronizing power is reduced and the frequencies of electromechanical oscillations are lowered [3, 4]. The reduced electromechanical frequencies, due to power system expansion, have the effect of reducing the damping from amortisseur windings. This led to Research and Development in finding damping from speed feedback through field excitation control. The final outcome of this is the Power System Stabilizer (PSS) [5-7]. The PSS has served power systems well for the past decade or two.

#### 1.1.2.1 Challenges Due to Further Power System Growth

Canada and many countries are motivated towards forming extensive intra- and trans-national grids. The new expansions are stimulated by the need: (i) to offer access and liquidity to energy markets, (ii) to provide the infrastructure for integrating alternative energy resources on a large-scale and/or (iii) to address power supply security concerns [8, 9]. Studies conducted on future interconnections estimate that on one hand there will be inter-area frequencies falling well below 0.2 Hz, on the other hand, there will be local oscillations exceeding 4 Hz [10, 11]. There is fear that conventional PSS cannot cope with such a broad frequency range, as they are limited by their bandwidths.

In general, the technologies which can cope are:

- (1) <u>HVDC</u>: Asynchronous links, based on back-to-back HVDC [12-15], enable power to be traded across regions while disturbances from one region are contained within the region. In North America, "HVDC fences" isolate the grid of Eastern USA from that of Western USA, the province of Quebec and the state of Texas [16, 17]. The regional grids remain relatively small and strong so that small signal instability can be suppressed by PSS. The power electronic control of the HVDC stations can also assist in damping. This technology is expensive.
- (2) <u>Flexible AC Transmission Systems (FACTS)</u>: In addition to increasing transient stability limit and offering voltage support, FACTS controllers (Thyristor Controlled Series Compensator (TCSC), Static VAR Compensator (SVC) [18-22], Static Synchronous Series Compensator (SSSC), Static Compensator (STATCOM), and Unified Power Flow

Controller (UPFC)) have the capacity to enhance dynamic performance such as improving system damping [23-34]. So far, not many FACTS controllers have been installed.

(3) Controllability  $_{
m in}$ Frequency Changers of Sustainable Energy Technologies: Sustainable energy technologies output dc power (photovoltaic) or variable frequency ac (variable speed wind turbines). Part of their costliness is due to the necessity to have power electronic frequency changers to convert the output power to the 60 Hz standard [14, 35-39. When the penetration of renewable technologies reaches 20 \% [40], it means that 20% of the grid power will be power electronically controlled. As in FACTS, the fast controllability can be applied to improve system damping. The difference with FACTS is that the 20% of sustainable energy technologies will have already been paid for and will not be added cost.

Although HVDC and FACTS are viable, the thesis will not consider them for reasons already given. In treating the all-AC system, the thesis must review the recent advance in WAM (Wide-Area Measurements) and WAC (Wide Area Control).

#### 1.1.2.2 Wide-Area Measurement (WAM)

A WAM is a measurement system ideally suited for power systems monitoring and control [41-43]. It is based on phasor measurement units (PMUs) [44] that continuously stream data to phasor data concentrators (PDCs) at central locations. The PMU synchronization is achieved via a GPS system that provides precise timing at better than 1μs [45]. Each phasor data concentrator collects and collates time-stamped measurements from many PMUs and rebroadcasts the combined data stream to locations running a range of power grid monitoring and control computer applications [41, 46].

#### 1.1.2.3 Wide Area Control (WAC)

Pioneering publications, notably those of [47, 48], are proposing Wide Area Controls (WAC) which make use of feedback signals taken from phasor measurement units (PMU) which are time-stamped by GPS clocks. Based on the simultaneously measured positions and speeds of selected generators gathered in hierarchical control centers, the requisite damping signals are sent back to the field excitation controllers of participating generators. The method depends on redundant communication links between the hierarchical control center and the selected participating generators. Tests performed on WAMSs have shown that control loop latency, including sensing, computation and activation, can be as short as 60 ms for direct links and up to 200 ms, when secondary links are

involved. But with respect to the time periods of the incipient low oscillating frequency oscillations of the increased-size interconnection, the phase angle is acceptable. One corner stone of the research is that conventional PSS will be damping the oscillations of 0.2 Hz and above.

#### 1.2 METHODOLOGIES OF RESEARCH

#### 1.2.1 Function Analysis

The thesis strives to find analytical proofs and close form analytical solutions, wherever possible.

A close form nonlinear formulation of a new power system archetype model is presented in chapter 4. In chapter 5, the difference between linear and nonlinear damping feedback is highlighted by Lyapunov functions [49-51].

#### 1.2.2 Eigenfunctions

The 2Nx2N [A]-matrix of the power system, made up of N generators, is constructed from the classical model of individual generators. The computation complexity is reduced by analyzing the NxN sub-matrix [A<sub>12</sub>], its eigenvalues and its left- and right- eigenvectors. The properties of right- and left-eigenvectors have led to the Multi-Selectivity Method in chapter 2. Analytical concepts are verified using numerical analysis and digital simulations.

#### 1.2.3 Numerical Analysis

Throughout the thesis, numerical analysis has made use of:

- 1. MATLAB—Simulink: Simulink [52] as an environment for multidomain simulation and model-based design for dynamic and embedded systems is used along with its SimPowerSystems toolbox [53] to model power system. SimPowerSystems extends Simulink with tools for modeling and simulating the generation, transmission, distribution, and consumption of electrical power.
- 2. MATLAB— Matlab is used for small signal stability analysis of interconnected ac power system. For complex power systems, MatNetEig toolbox [54] is used to form the sparse linearized coupled differential algebraic equations describing the systems dynamics in the frequency range of transient power system dynamics. Modal analysis, frequency response, and step response can be calculated using this toolbox in Matlab.
- 3. HYPERSIM— For digital simulations, the author has access to Hydro-Quebec's HYPERSIM, a commercial grade simulation system of TransEnergie (Hydro-Quebec), initially from l'Ecole de Technologie Superieure (ETS) and later from Polytechnique de Montreal. Invaluable to research is the collection of power plant components, based on detail models recommended by IEEE Committee Reports: the generator, the

field excitation system, the power system stabilizer, the boiler, the high pressure, intermediate pressure, and low pressure turbines, as well as the governor and the shaft inertias [55-59].

#### 1.2.4 Phase-Plane Method

Although the phase-plane method [60] is only suitable for 2-dimension analysis, it is useful to demonstrate instability in nonlinear system and nonlinear damping in chapter 4.

#### 1.3 Organization of Thesis

The thesis is organized as follows:

- Damping from Wide-Area Control: Chapters 2 and 3.
- Damping from Complex Power Injection from Sustainable Energy
  Technologies: Chapter 4.
- Nonlinear Damping: Chapter 5.
- Conclusions and Suggestions of Further Work: Chapter 6.

<u>Chapter 2</u> presents the design of the centralized control assuming that the classical [A] matrix is given. The computation burden of evaluating eigenvalues and eigenvectors of [A] increases with N<sup>3</sup>, N being the system order. It is assumed that the Lanczos method [61-63], which enables the eigenvectors of the few lowest frequency modes beyond the range of local PSS, is affordable and accurate. As

the remaining eigenvalues and eigenvectors are unknown, it behoves the design to have very high selectivity [87]. Although, there is safe guard that PSS can damp the high frequency modes, it is preferred the high selectivity will ensure that in damping the selected slow modes, the other modes are not destabilized.

High selectivity is obtained by using the linear independence of left eigenvectors and the right eigenvectors. Three (3) layers of selectivity are incorporated in the design. The first layer is in using the right eigenvector to select the generator stations which are positioned to yield the most sensitive detection of modal disturbance and at the same exert maximum power to suppress the disturbance. The second layer is in applying the left eigenvector as weights to the "observer or [C]" inputs of the centralized controller. By the spatial filtering, the targeted low frequency mode is recognized. Once recognized, the centralized controller sends suppression signal to the selected generators in amounts proportional to the right eigenvector. The right eigenvector in the controllability matrix [B] is third layer of selectivity.

<u>Chapter 3</u> presents results from digital simulations and eigenvalue analysis to validate the claims on the ability to damp the selected low frequency modes without destabilizing the others.

As proof of the robustness of the method, the author's 12-generator test system has been subjected to tests in which every one of the tie lines connecting the 4 areas is assumed to have been severed, one at a time. It is found that the

centralized control continues to damp out the disturbances following the disruptions.

## Controllability in Frequency Changers of Sustainable Energy Technologies: Chapter 4

The frequency changers of sustainable energy technologies are mainly Voltage-Source Converters (VSCs) [36, 38, 64]. They have the same fast controllability of FACTS controllers to inject reactive power to improve power system damping. But whereas FACTS controllers can inject reactive power only, the sustainable energy technologies can inject active power, reactive power and a combination of the two.

The research is directed to finding out the effectiveness of damping in relation to the placement of the injection point along the transmission line. It is found that reactive damping is most effective in the middle of the line while active power is best next to the transformers of the line. The findings of this thesis confirm the investigations by small signal linearization [65].

The difference with the research by [65] lies in the fact the complex power modulator (frequency changers of sustainable energy technologies) is modeled as a nonlinear equation and the close-form algebraic expression is retained throughout the research.

One reason for the retention of the nonlinearity is that prior work has depended on small signal linearization. Consequently, the consequences of large perturbations remain in the dark.

#### Investigating Nonlinear Damping: Chapter 5

The other reason is that in designing injection of active and/or reactive power to augment damping requires tuning of the proportional and integral feedback gains with respect to the saturation limits. Without taking nonlinearity into account, the designer merely gropes by trial and error. Using phase-plane diagrams, this chapter gives a clear picture of the trade-offs of gain constants with respect to saturation limits in securing high damping. Simulations and the method of Lyapunov show that whereas linear damping attenuates exponentially with time, nonlinear damping attenuates linearly with time.

### CHAPTER 2

# DAMPING INTER-AREA OSCILLATIONS BY MULTIPLE MODAL SELECTIVITY METHOD

#### 2.1 Introduction

The research of this chapter is motivated by concern that existing designs in power system stabilizers (PSS) may not have broad enough bandwidth: (i)to damp low frequency inter-area oscillations when interconnected power utilities continue to grow in size and, at the same time, (ii) to damp the high frequency oscillations of local modes. The solution, proposed here, adds a Global PSS (which damps the inter-area modes) to existing PSS (which continue to damp the high frequency local area modes).

In the Global PSS concept, PMU time-stamped information of speeds of selected generators is telecommunicated to a Central Controller which applies the Multiple Modal Selectivity Method to generate feedback commands which are telecommunicated back to the same selected generators to damp the low frequency oscillations. Because the inter-area frequencies fall well below 0.2 Hz, communication delay is negligible in the 5 second period of the oscillations.

The methodology is based on state feedback applied to the linearized [A] matrix of classical small signal stability analysis of the power system. Well aware that all the eigenfunctions of [A] are not often available for high order systems, the method is developed to require knowledge of only the few very low frequency inter-area modes which can be obtained economically by Lanczos-based methods [61-63]. It is possible to get by with the limited knowledge by taking advantage of the properties of left and right eigenvectors. Exploiting the fundamental

properties, 3 levels of selectivity to damp the low frequency modes without destabilizing the others are incorporated in the design: (1) selecting power stations best placed to implement the feedback control; (2) screening the speed signals telecommunicated to central control; (2) modal weighting of the signals feedback telecommunicated back to the few selected stations.

The chapter is organized as follows: Section 2 presents the classical small signal stability analysis framework. Section 3 presents the Multiple Modal Selectivity Method. Section 4 presents a small power system to test the method. Section 5 describes how the method is implemented in central control. Section 6 describes the planning stage to select which power stations are to be included in the control.

#### 2.2 BACKGROUND

#### 2.2.1 Dynamics of Linear Systems

This research follows the standard linearized equations used in steady-state stability analysis of the power system:

$$\begin{bmatrix} \Delta \underline{\dot{\omega}} \\ \Delta \underline{\dot{\delta}} \end{bmatrix} = \begin{bmatrix} [A_{11}] & [A_{12}] \\ [A_{21}] & [A_{22}] \end{bmatrix} \begin{bmatrix} \Delta \underline{\omega} \\ \Delta \underline{\delta} \end{bmatrix}$$
 (2.1)

The N-tuple vectors of rotor speed and angle perturbations are  $\Delta\underline{\omega}$  and  $\Delta\underline{\delta}$ . The N×N sub-matrices of the 2N×2N [A]-matrix are  $[A_{21}]=[I]$ ,  $[A_{11}]=[A_{22}]=[0]$  and  $[A_{12}]$  has the formula:

$$[A_{12}] = \left[ -[diag(\underline{h})]^{-1} \left[ \frac{\partial \underline{P}_e}{\partial \underline{\delta}} \right] \right]$$
 (2.2)

where  $\left|\frac{\partial \underline{P}_e}{\partial \underline{\delta}}\right|$  is the Jacobian of  $\underline{P}_e$  given by DC power flow equations [41]. Note that derivations leading to (2.2) are simplified by assuming that generator speed and its terminal frequency are the same.  $\underline{P}_e$  is linked to dynamics of generators by

$$\frac{2H_{i}}{\omega_{s}}\frac{d\omega_{i}}{dt}=p_{m_{i}}-p_{e_{i}} \qquad \qquad i=1,...,N \tag{2.3} \label{eq:2.3}$$

The diagonal matrix  $[\operatorname{diag}(\underline{\mathbf{h}})]$  is defined as

$$\left[ diag(\underline{h}) \right] = \frac{2}{\omega_S} \begin{bmatrix} H_1 & 0 & . & 0 \\ 0 & H_2 & . & 0 \\ . & . & . & . \\ 0 & 0 & . & H_N \end{bmatrix}$$
 (2.4)

The [A]-matrix is constructed here using (2.3); that is, the generator classical model. Then again, one can use highly detail models to represent generators and their sub-systems dynamics. However, in that case, not much will be gained since, as far as rotor speeds are concerned, the mode shapes of slow inter-area oscillations (to be discussed in Section 2.4.2) will stay largely the same. At the same time, the mathematics will become increasingly unwieldy and the problem dimensionality will grow by many folds.

To halve the dimensionality, the practice is to analyze the N×N sub-matrix  $[A_{12}]$ , instead of the 2N×2N [A]-matrix, and use its eigen properties alone to describe the system dynamics. This practice has been extended to the formulations of this thesis and the correctness of the conclusions reached since the N×N analysis has

been counter-checked by  $2N\times2N$  analysis. Moreover, the predictions are checked numerically in eigenvalues evaluations and time-domain simulations based on (2.1).

#### 2.2.2 Modal Analysis [63, 66]

On diagonalizing [A<sub>12</sub>], one has a N×N diagonal matrix:

$$[diag(\underline{\lambda})] = [V]^{T} [A_{12}][U] \tag{2.5}$$

where the right eigenvector matrix is

$$[U] = [\underline{u}_1, \underline{u}_2, \dots, \underline{u}_N] \tag{2.6}$$

and where the left eigenvector matrix is

$$[V] = [\underline{v}_1, \underline{v}_2, \dots, \underline{v}_N] \tag{2.7}$$

The linear independence property which is the key feature of the method is:

The above relations can also be stated as  $[V]^T[U]=[I]$ . While (2.8) is a general mathematical property, it has been proved in Appendix A of [66] that for the specific case of  $[A_{12}]$ 

$$\underline{v}_{j} = \left[ diag(\underline{h}) \right] \ \underline{u}_{j} \tag{2.9}$$

The eigenvalues in the vector  $\underline{\lambda}$  of (2.5) are all negative real numbers of the form  $-(\omega_k)^2$ . They are reconstituted in the 2N×2N eigenvalue matrix [A] of the [A]-matrix:

$$\begin{bmatrix} \Lambda \end{bmatrix} = \begin{bmatrix} \Lambda_{11} & \Lambda_{12} \\ \Lambda_{21} & \Lambda_{22} \end{bmatrix} \tag{2.10}$$

where  $[\Lambda_{11}]=[\operatorname{diag}(\underline{j}\underline{\omega})]$ ,  $[\Lambda_{22}]=[\operatorname{diag}(-\underline{j}\underline{\omega})]$  and  $[\Lambda_{12}]=[\Lambda_{21}]$  =[0]. This means that the modes have oscillatory frequencies  $\omega_k$ , k=1,2..N, but there is no negative real parts to provide damping. The right and left eigenvectors of (2.6) and (2.7) are all real numbers. They have been used to build the left and right eigenvectors of  $2N\times2N$  [A]-matrix in our in-depth analysis [67], but the concepts of this research can be presented without being encumbered by mathematical correctness.

#### 2.2.3Linear feedback

The standard linearized control feedback equations are:

$$\underline{\dot{x}} = [A]\underline{x} + [B]\underline{z} \tag{2.11}$$

$$\underline{z} = [K]\underline{y} \tag{2.12}$$

$$\underline{y} = [C]\underline{x} \tag{2.13}$$

Following other authors [10, 63, 68], this thesis considers the speed vector  $\Delta \underline{\omega}$  as the feedback signals for damping, which makes the sub-matrix [A<sub>11</sub>] in (2.1) non-zero and allows setting

$$[C] = \begin{bmatrix} [C_{11}] & [0] \\ [0] & [0] \end{bmatrix}$$
 (2.14)

$$[B] = \begin{bmatrix} [B_{11}] & [0] \\ [0] & [0] \end{bmatrix} \tag{2.15}$$

The speed signals received at central control is  $\underline{\mathbf{y}}=[\mathbf{C}_{11}]\underline{\Delta}\underline{\omega}$ , with  $[\mathbf{C}_{11}]$  deciding which stations should be connected to central control. A "connected station" here refers to a power station that is fully equipped to operate as part of a WAMS-based monitoring and control system.

The N×N gain matrix  $[K_{11}]$  is chosen to achieve high selectivity in controlling the targeted modes. Its outputs  $\underline{z} = [K_{11}]\underline{y}$  are relayed to the same stations so that  $[B_{11}] = [C_{11}]$  and the feedback signals  $[B_{11}]\underline{z}$  are added to the first row of (2.1). The presence of the feedback loop changes the original [A]-matrix in (2.1) by  $[\Delta A]$ , where

$$[\Delta A] = \begin{bmatrix} [\Delta A_{11}] & [0] \\ [0] & [0] \end{bmatrix} \tag{2.16}$$

where

$$[\Delta A_{11}] = [B_{11}][K_{11}][C_{11}] \tag{2.17}$$

It can be shown that the matrices [U] and [V] of (2.6) and (2.7) can be applied to  $[\Delta A]$  of (2.16) to yield  $[\Delta \Lambda_{11}]$ , where

$$[\Delta \Lambda_{11}] = [V]^T [\Delta A_{11}][U] \tag{2.18}$$

is a real NxN matrix added to the imaginary diagonal sub-matrix  $[\Lambda_{11}]=[diag(j\underline{\omega})]$  of (2.10). Substituting (2.17) in (2.18)

$$[\Delta \Lambda_{11}] = [V]^T [B_{11}] [K_{11}] [C_{11}] [U]$$
 (2.19)

#### 2.3 METHOD OF MULTIPLE MODAL SELECTIVITY

The Multiple Modal Selectivity Method [87] adds to the advances of Selective Modal Analysis [69, 70]. It is more easily understood by considering first the perfect decoupling of a single mode, the  $k^{th}$  mode. After deriving the key equations, the same equations are applied to the realistic case with minor changes. To show that the derived formulas are specific to the  $k^{th}$  mode alone, subscript (k) has been added to symbols such as  $[\Delta\Lambda_{11}]$  to become  $[\Delta\Lambda_{11(k)}]$ .

#### 2.3.1 Perfect Decoupling

From Lanczos-based method [61], the right and left eigenvectors  $\underline{\mathbf{u}}_k$  and  $\underline{\mathbf{v}}_k$  of the  $k^{th}$  mode (the target mode) have been solved. It is assumed that all N stations are connected to central control so that  $[C_{11}]=[B_{11}]=[I]$ , which is the identity matrix. The damping coefficient is chosen to be  $-\sigma_k$ . Two selectivity stages are implemented through the gain matrix:

$$[K_{11(k)}] = -\sigma_k \underline{u}_k \underline{v}_k^T \tag{2.20}$$

Substituting  $[\mathrm{C}_{\scriptscriptstyle{11}}]{=}[\mathrm{B}_{\scriptscriptstyle{11}}]{=}[\mathrm{I}]$  and (2.20) in (2.19)

$$[\Delta \Lambda_{11(k)}] = -\sigma_k [V]^T \underline{u}_k \underline{v}_k^T [U]$$
(2.21)

The first stage is at the measurement-side, which yields a row vector:

$$v_{i}^{T}[U] = [v_{i}^{T}u_{1}, v_{i}^{T}u_{2}, \dots, v_{i}^{T}u_{N}]$$
 (2.22)-a

The second stage is at the controller-side, which yields a column vector:

$$[V]^T \underline{u}_k = \begin{bmatrix} \underline{v}_1^T \underline{u}_k \\ \underline{v}_2^T \underline{u}_k \\ \vdots \\ \underline{v}_N^T \underline{u}_k \end{bmatrix}$$
(2.22)-b

Therefore, the i-j  $^{th}$  element of  $[\Delta\Lambda_{11(k)}]$  is:

$$\Delta \lambda_{ij(k)} = -\sigma_k(\underline{v}_i^T \underline{u}_k)(\underline{v}_k^T \underline{u}_j) \tag{2.23}$$

Based on (2.8),  $[\Delta\Lambda_{11(k)}]$  entries are all zero except for the  $k^{th}$  element for which  $\Delta\lambda_{kk(k)} = -\sigma_k$ . For the closed loop feedback system of  $[A] + [\Delta A_{(k)}]$ , the  $k^{th}$  eigenvalue is  $\lambda_{kk(k)} = -\sigma_k + j\omega_k$ , and the  $k+N^{th}$  eigenvalue is  $\lambda_{kk(k)} = -\sigma_k - j\omega_k$ . All the other eigenvalues are  $\lambda_{ii} = +j\omega_i$ ,  $\lambda_{i+N,i+N} = -j\omega_i$  (i=1,2..N, i\neq k) and, therefore, have no damping.

#### 2.3.2Practical Case

In practice, it is only affordable to connect a limited number of power stations to the central control. In order to preserve the result of (2.23), the changes required in mathematical modeling are to put zeroes in the diagonal terms of  $[C_{11}]=[B_{11}]\neq[I]$ , where the stations are not connected. This has the consequence that zeroes have to replace the elements in the corresponding rows of the right and left eigenvectors. The changes are conveniently accommodated by defining new N-tuple vectors  $\hat{\underline{u}}_i$  and  $\hat{\underline{v}}_i$  such that:

$$\underline{\hat{u}}_i = [B_{11}]\underline{u}_i \tag{2.24}-a$$

$$\underline{\hat{v}}_i = [C_{_{11}}]\underline{v}_i \tag{2.24}-b$$

For example, when only stations 1, 3, and N are connected,  $\underline{\hat{u}}_i^T = [u_{1i},0,u_{3i},0,...,0,u_{Ni}] \text{ and } \underline{\hat{v}}_i^T = [v_{1i},0,v_{3i},0,...,0,v_{Ni}]. \text{ This also allows the gain matrix to be defined as:}$ 

$$[K_{11(k)}] = -\sigma_k \hat{\underline{u}}_k \hat{\underline{v}}_k^T \tag{2.25}$$

With this remodeling, (2.23) is modified to:

$$\Delta \lambda_{ii(k)} = -\sigma_k(\hat{\underline{v}}_i^T \hat{\underline{u}}_k)(\hat{\underline{v}}_k^T \hat{\underline{u}}_j)$$
(2.26)

The k-k<sup>th</sup> term yields a negative real damping term:

$$\Delta \lambda_{kk(k)} = -\sigma_k (\hat{\underline{v}}_k^T \hat{\underline{u}}_k)^2 \tag{2.27}$$

Since  $(\hat{\underline{v}}_i^T \hat{\underline{u}}_k) \neq 0$  for  $i \neq k$ , and  $(\hat{\underline{v}}_k^T \hat{\underline{u}}_j) \neq 0$  for  $j \neq k$ ,  $[\Delta \Lambda_{11(k)}]$  is a full NxN matrix of real numbers. Therefore, in damping the  $k^{th}$  mode, the other modes are affected. At best, one chooses the locations of the connected stations to minimize the lambda-ratio in the  $[\Delta \Lambda_{11(k)}]$ -matrix:

$$lambda - ratio_{ij(k)} = \frac{\Delta \lambda_{ij(k)}}{\Delta \lambda_{kk(k)}} = \frac{(\hat{\underline{v}}_i^T \hat{\underline{u}}_k)(\hat{\underline{v}}_k^T \hat{\underline{u}}_j)}{(\hat{\underline{v}}_k^T \hat{\underline{u}}_k)^2}$$
(2.28)

The quadratic structures in the numerator and denominator in (2.28) contribute towards making  $[\Delta\Lambda_{11(k)}]$  close to a diagonal matrix. For example, if  $|\hat{\underline{v}}_i^T\hat{\underline{u}}_k|/|\hat{\underline{v}}_k^T\hat{\underline{u}}_k| \leq 0.33$  and  $|\hat{\underline{v}}_k^T\hat{\underline{u}}_j|/|\hat{\underline{v}}_k^T\hat{\underline{u}}_k| \leq 0.33$ , then lambda-ratio<sub>ij</sub> < 0.1.

#### 2.3.3 Negative Real Numbers for Diagonal Elements

From (2.26), the diagonal elements are

$$\Delta \lambda_{ii(k)} = -\sigma_k(\hat{\underline{v}}_i^T \hat{\underline{u}}_k)(\hat{\underline{v}}_k^T \hat{\underline{u}}_i)$$
(2.29)

From (9),  $\underline{\hat{v}}_i = \left[diag(\underline{\hat{h}})\right]\underline{\hat{u}}_i$  and  $\underline{\hat{v}}_k = \left[diag(\underline{\hat{h}})\right]\underline{\hat{u}}_k$ , where  $\left[diag(\underline{\hat{h}})\right]\underline{=}[C_{11}][diag(\underline{h})]$ . On substitution in (2.29), as  $\underline{\hat{u}}_i^T[diag(\underline{\hat{h}})]\underline{\hat{u}}_k = \underline{\hat{u}}_k^T[diag(\underline{\hat{h}})]\underline{\hat{u}}_i$ , it indicates that

$$\Delta \lambda_{ii(k)} \le 0 \qquad i = 1, 2..N \tag{2.30}$$

Since the diagonal elements of  $[\Delta\Lambda_{11(k)}]$  are all not positive, the trace of  $[\Lambda_{11}]+[\Delta\Lambda_{11(k)}]$  does not have a real positive part. While that is insufficient to guarantee stable operation, it indicates that the feedback is unlikely to be destabilizing. This conclusion based on the trace is supported by eigenvalue evaluations of  $[A]+[\Delta A]$ , that is the  $2N\times 2N$  system of (2.1) with the feedback system of (2.16). In every case, the real parts of the complex conjugate pairs of all the eigenvalues have negative real parts. The time domain simulations also show that every mode is positively damped.

#### 2.4 TEST SYSTEM MODAL PROPERTIES

A 12-generator system has been contrived, shown in Figure 2.1, to test the proposed method. Although a small power system, it has the low frequency modes similar to the inter-area modes of large systems and high frequency modes, which the method must not destabilize. The system is intended primarily to bring the ideas across quickly. There is no conceptual barrier in applying the ideas to continental-size grids (USA-Canada, European Union, Brazil, Russia, India, China).

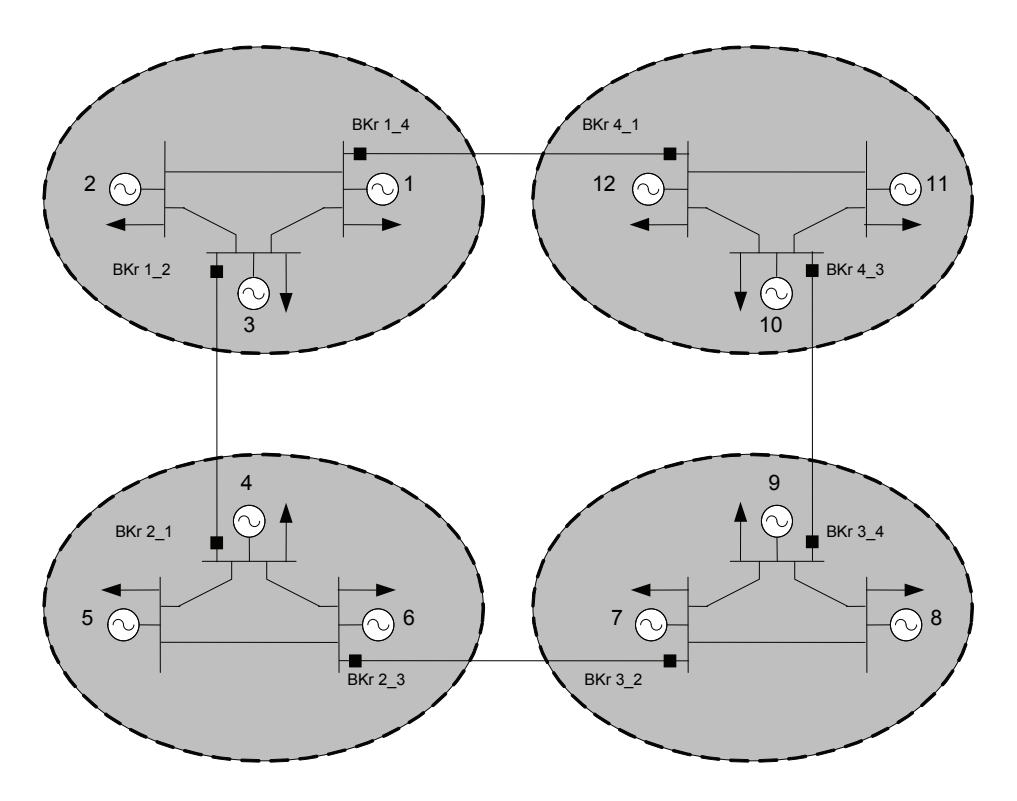


Figure 2.1 Power System one-line diagram

# 2.4.1 Test Power System

The power system of Figure 2.1 consists of four regions, each having 3 generating units, connected by three 69 kV lines. The 4 tie-lines connecting the regions are operating at 115 kV. The generators are all thermal, have round rotors, ideal step-up transformers, and a rating of 250 MVA, which is also chosen to be the system MVA base. Loads are assumed to be fixed power demands with unity power factors.

Table 2.1 Power system load and generation data

Bus No.	Generation		Load	Bus No.	Generation		Load
	H(s)	$P_g(MW)$	$P_{d}(MW)$		H(s)	$P_{g}(MW)$	$P_{d}\left(MW ight)$
1	3.5	200	200	7	4.1	197	220
2	4.1	210	82	8	4.3	205	324
3	3.8	190	160	9	3.6	198	264
4	4.0	200	225	10	3.8	197	130
5	4.2	195	285	11	4.0	200	180
6	4.3	210	110	12	4.5	203	225

Table 2.1 contains the generation and load data, as well as the generators' normalized inertia, for each bus. Resistive losses and shunt capacitances are not modeled in the lines. Table 2.2 lists their inductive reactances and connectivity data.

Table 2.2 Lines' connectivity and per-unit reactances

line	X(pu)	line	X(pu)	Line	X(pu)	Line	X(pu)
1-2	0.655	5-6	0.619	9-7	0.716	3-4	2.466
2-3	0.704	6-4	0.705	10-11	0.680	6-7	2.793
3-1	0.712	7-8	0.629	11-12	0.704	9-10	2.607
4-5	0.632	8-9	0.678	12-10	0.601	12-1	2.827

# 2.4.2 Open Loop Properties

By formulating the [A]—matrix of (2.1) and using eigenanalysis software, the 12 modes are solved. Table 2.3 lists the eigenvalues of the modes, #1, #2..... #11, in ascending orders of their frequencies (all real parts are zero) and classifies them as "slow' and "fast". Mode # 12 is the zero frequency reference.

Table 2.3 Modal frequencies and their classification

Mode	$\omega \; (\mathrm{rad/s})$	f (Hz)	Class	Mode	$\omega \; (\mathrm{rad/s})$	f (Hz)	Class
1	3.15	0.502	slow	7	14.76	2.349	fast
2	3.31	0.527	slow	8	15.08	2.399	fast
3	4.69	0.746	slow	9	15.24	2.426	fast
4	14.16	2.254	fast	10	15.70	2.499	fast
5	14.29	2.275	fast	11	15.99	2.545	fast
6	14.53	2.312	fast	12	0.00	0.000	

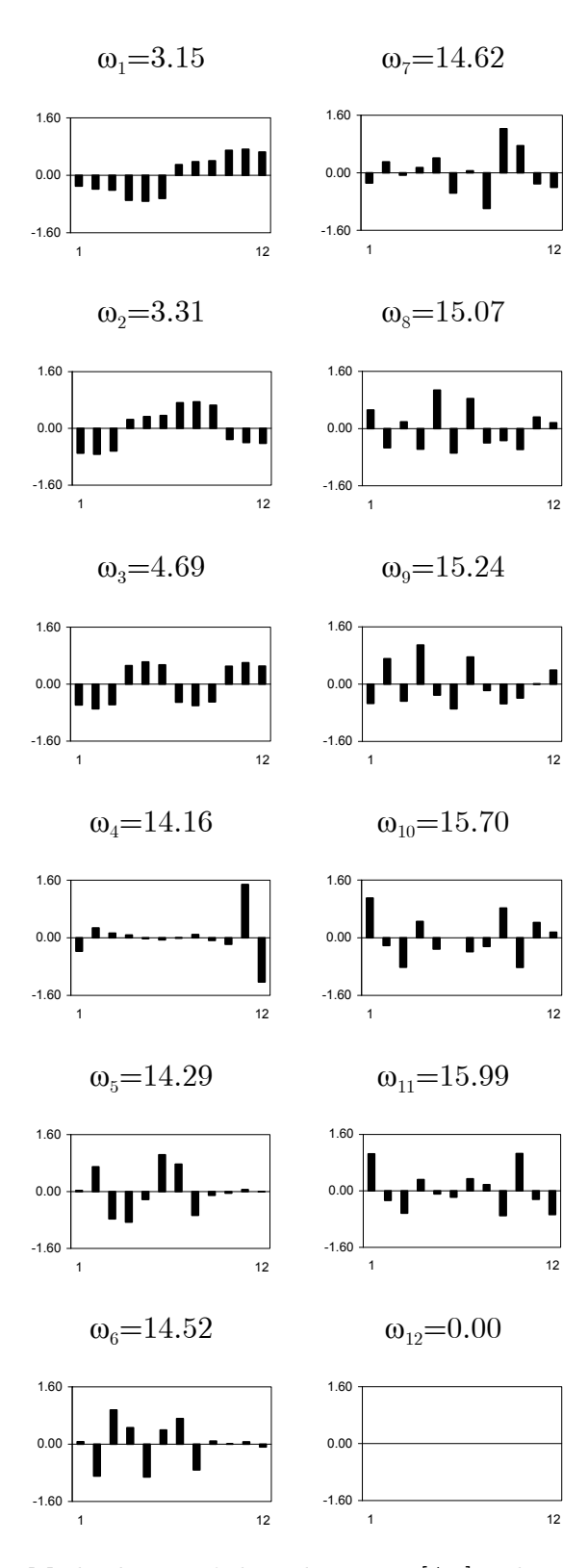


Figure 2.2 Mode shapes of the sub-matrix  $[A_{12}]$  right eigenvectors

#### 2.4.3 Mode Shapes of Right Eigenvectors

The mode shapes in Figure 2.2 are drawn from right eigenvector components of  $[A_{12}]$ . They are presented in order, Mode #1, #2,..., #12, from top to bottom, starting from the left column.

The envelopes of the bars of Mode #1 and #2 have the lowest spatial frequency profile. Mode #3 has the next higher spatial frequency. The lowest spatial frequency correlates with the lowest temporal frequency, a finding that is in good agreement with analytical conclusions of [67].

#### 2.4.4 Mode Shapes of Left Eigenvectors

The left eigenvector mode shapes are not displayed. From (2.9), they are similar to Figure 2.2 since in Table 2.2 the sizes of the inertia constants in  $\underline{\mathbf{h}}$  do not vary significantly.

# 2.4.5 Implementing Linear Independence

#### 2.4.5.1 Perfect case

As described in section 2.3, the Multiple Modal Selectivity Method depends on linear independence of (2.8). Figure 2.3 is a graphical illustration of the inner product operation, for  $\underline{\mathbf{v}}_1^T\underline{\mathbf{u}}_1$ ,  $\underline{\mathbf{v}}_2^T\underline{\mathbf{u}}_1$  and  $\underline{\mathbf{v}}_9^T\underline{\mathbf{u}}_1$ . The 3 rows in the first column of Figure 2.3 depict the same mode shape of  $\underline{\mathbf{u}}_1$  of Mode #1. The interest is to know how Mode #1 can become coupled to itself, to a slow Mode #2 and to fast Mode

#9. The second column shows the mode shapes of  $\underline{v}_1$ ,  $\underline{v}_2$  and  $\underline{v}_9$  in the 3 rows. The bar charts in the last column are the results of multiplying corresponding bars of the two mode shapes on the same row. In the last column, for  $\underline{v}_1^T\underline{u}_1$ , the bars only take positive values and add up to 1 (i.e.  $\underline{v}_1^T\underline{u}_1=1$ ). But, for  $\underline{v}_2^T\underline{u}_1$  and  $\underline{v}_9^T\underline{u}_1$  the bars assume both positive and negative values, so that they tally to zero (i.e.  $\underline{v}_2^T\underline{u}_1=\underline{v}_9^T\underline{u}_1=0$ ).

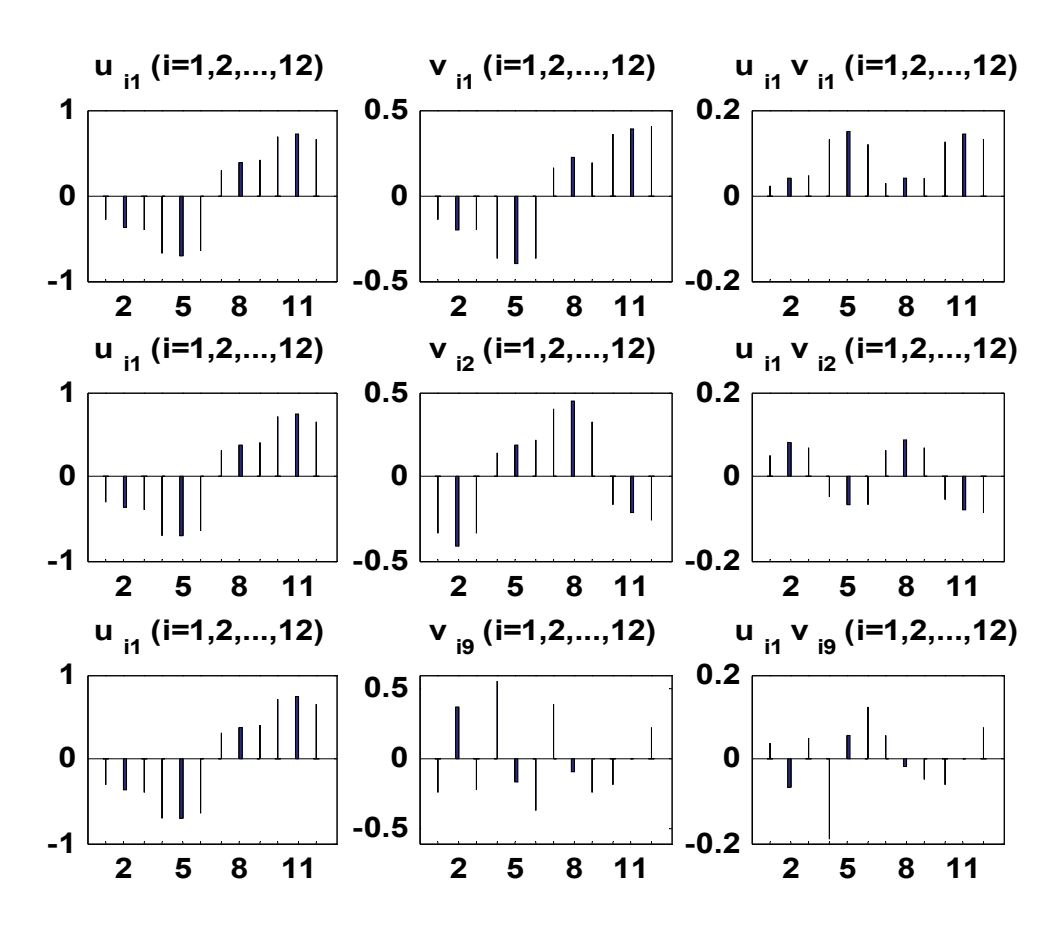


**Figure 2.3** Graphical interpretations of operations  $\underline{v}_1^T\underline{u}_1$ ,  $\underline{v}_2^T\underline{u}_1$  and  $\underline{v}_9^T\underline{u}_1$ .

#### 2.4.5.2 Practical case

Reducing the number of connected stations causes  $\underline{\hat{u}}_i$  and  $\underline{\hat{v}}_i$  to have fewer bars than  $\underline{u}_i$  and  $\underline{v}_i$ . In Figure 2.3, the heavy bars in the first two columns denote  $\underline{\hat{u}}_1$ ,  $\underline{\hat{v}}_1$ ,  $\underline{\hat{v}}_2$ , and  $\underline{\hat{v}}_9$  mode shapes when power stations 2, 5, 8, and 11 are connected. The heavy bars in the first row, third column indicate that a reasonably large value for  $\underline{\hat{v}}_1^T\underline{\hat{u}}_1$  is attainable. The second row, third column indicates that the value of  $\underline{\hat{v}}_2^T\underline{\hat{u}}_1$  is not zero but small. It says that, by connecting stations 2, 5, 8, and 11, modes #1 and #2 are almost decoupled. Finally, one sees that  $\underline{\hat{v}}_9^T\underline{\hat{u}}_1$  is unlikely to be small. The examples show that locating the best stations is critical in moving  $\underline{\hat{v}}_i^T\underline{\hat{u}}_i$  and  $\underline{\hat{v}}_j^T\underline{\hat{u}}_i$ towards 1 and zero, respectively, and, thus, the success of the method.

#### 2.5 IMPLEMENTATION

#### 2.5.1 Imposed Requirements

As PSS can damp the fast modes of Figure 2.1, the Multiple Modal Selectivity Method is required to damp the slow modes (#1, #2, and #3). The slow modes should be decoupled so that oscillation excited in one mode does not disturb another slow mode. The only information available is the right eigenvectors of the slow modes, which have been solved by a Lanczos- based method [61]. The number of power stations connected to central control should not exceed 4.

Knowing  $\underline{\mathbf{u}}_1$ ,  $\underline{\mathbf{u}}_2$  and  $\underline{\mathbf{u}}_3$  the left eigenvectors  $\underline{\mathbf{v}}_1$ ,  $\underline{\mathbf{v}}_2$  and  $\underline{\mathbf{v}}_3$  are computed from (2.9). At this point, the 4 connected power stations are assigned algebraic numbers j, l, m, and n. Their choice is determined by selection based on a performance criterion described in the next section. After determining j, l, m, and n the reduced vectors  $\underline{\hat{u}}_k$ ,  $\underline{\hat{v}}_k$ , k=1,2,3 are formed.

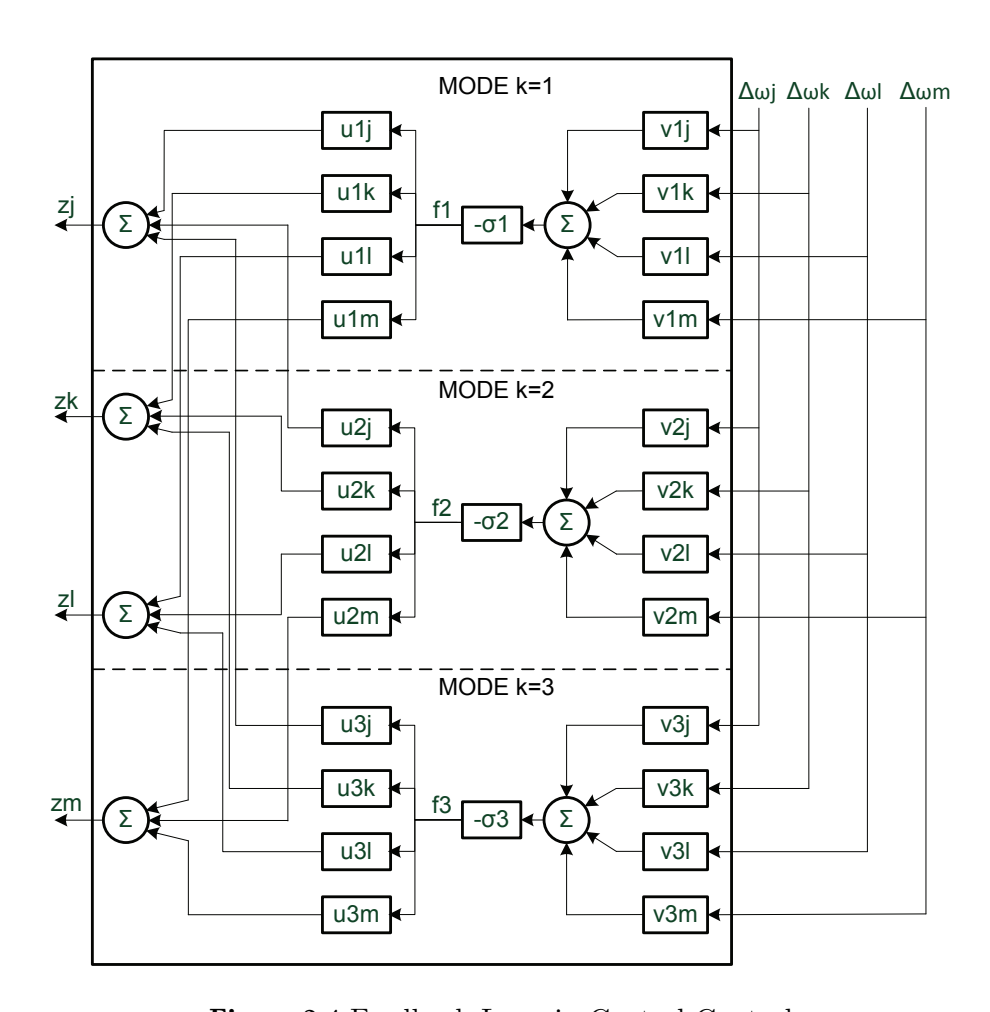


Figure 2.4 Feedback Loop in Central Control

Figure 2.4 shows the central control feedback blocks for Modes #1, #2 and #3, each of which implements  $-\sigma_k \hat{\underline{u}}_k \hat{\underline{v}}_k^T$  (k=1,2,3) as described in section 2.3. The

selected speeds are  $\left\{x_j, x_l, x_m, x_n\right\}$ , the outputs are  $\left\{z_j, z_l, z_m, z_n\right\}$  and the reduced vectors are  $\underline{\hat{u}}_k^T = [0, ..., u_{jk}, 0, ..., u_{lk}, 0, ..., u_{nk}, 0, ..., u_{nk}, ..., 0]$  and  $\underline{\hat{v}}_k^T = [0, ..., v_{jk}, 0, ..., v_{jk}, 0, ..., v_{nk}, 0, ..., v_{nk}, ..., 0]\,.$ 

In controlling 3 modes, the central control of Figure 2.4 requires modifying (2.20) and (2.21) as follows:

$$\begin{split} [K_{11}] &= \sum_{k=1}^{3} [K_{11(k)}] \\ [\Delta \Lambda_{11}] &= \sum_{k=1}^{3} [\Delta \Lambda_{11(k)}] \end{split} \tag{2.31}$$

#### 2.5.2 Control Center Level Implementation

At the control center, the feedback signals,  $[B_{11}]\underline{z} = \hat{\underline{z}}$ , will be calculated from  $\Delta\underline{\omega}^{meas}$ , the measured rotor speed deviations telemetered by WAMS. From (2.17) and (2.20), one has,

$$\underline{\hat{z}} = [B_{11}]\underline{z} = [B_{11}] \left( \sum_{k \in S_m} -\sigma_k \underline{u}_k \underline{v}_k^T \right) [C_{11}] \Delta \underline{\omega}^{meas} \tag{2.32}$$

The index set  $S_m$  contains the target modes. Using definitions (2.24) and bringing  $\Delta\underline{\omega}^{meas}$  inside the summation, (2.32) becomes

$$\hat{\underline{z}} = \sum_{k \in S_m} f_k \hat{\underline{u}}_k \tag{2.33}$$

The weights  $f_k$  in (2.33) are related to the measurements by,

$$f_{\boldsymbol{k}} = -\sigma_{\boldsymbol{k}} \underline{\hat{v}}_{\boldsymbol{k}}^T \Delta \underline{\omega}^{meas} = -\sigma_{\boldsymbol{k}} \sum_{j \in S_t} v_{\boldsymbol{k}, j} \Delta \omega_j^{meas} \tag{2.34}$$

The index set  $S_t$  is holding indices of selected rotor speed telemetries. In Fig. 2.4, the summations on the left form  $f_k$ , k=1,2,3, while the summations on the right

follow (2.33) to generate the control signals  $\left\{z_j,z_l,z_m,z_n\right\}$ , which are the nonzero entries of  $\hat{\underline{z}}$ .

# $\it 2.5.3 Plant\ Level\ Implementation$

Through WAMS, the calculated control signals will be dispatched to power plants whose generators are selected to damp the inter-area oscillations. At the plant level, the control signal will be passed to the Remote Terminal Unit (RTU) of the selected generator for realization. At this point, a few options are available for feeding back the control signal. It can be input via the generator PSS or directly via the generator Exciter input, with the possibility of being combined with the locally generated control signal or used alone. Depending on the choice, "conditioning" of the control signal will be different. Preliminary simulations done by the author on systems with fully modelled generators indicate that, when no local control signal is present, both options can successfully damp the interarea oscillations.

#### 2.6 SELECTION OF CONTROLLING GENERATORS

#### 2.6.1 Maximizing Damping

In order to maximize the damping in all the 3 modes, based on (2.27), the best placement of the 4 stations j, l, m and n corresponds to  $\underline{\hat{u}}_i$  and  $\underline{\hat{v}}_i$  (i=1, 2, 3) which maximize  $\Sigma_{\sigma}$  where

$$\Sigma_{\sigma} = \sum_{i=1}^{3} \hat{\underline{v}}_{i}^{T} \hat{\underline{u}}_{i} \tag{2.35}$$

#### 2.6.2 Maximizing Decoupling

It is highly desirable to have dynamics of the modes decoupled [68]. As has been illustrated in Figure 2.3, the r<sup>th</sup> mode is decoupled from the i<sup>th</sup> mode when  $\hat{\underline{v}}_r^T \hat{\underline{u}}_i$  is small relative to  $\hat{\underline{v}}_i^T \hat{\underline{u}}_i$ . For the 3 slow modes to be as decoupled as possible, it is desirable to have  $\Sigma_{decoup}$  as small as possible.

$$\Sigma_{decoup} = \sum_{r=1}^{3} \sum_{i=1}^{3} |\hat{\underline{v}}_{r}^{T} \hat{\underline{u}}_{i}| - \sum_{i=1}^{3} \hat{\underline{v}}_{i}^{T} \hat{\underline{u}}_{i}$$
 (2.36)

In combining maximum damping and maximum decoupling, the figure of performance used is

$$W = \sum_{\sigma} - \sum_{decoup} \tag{2.37}$$

By exhaustively evaluating all combinations of (j, l, m, n) and ranking W in order of magnitude, one has a range of best values from which to choose. If the power station is not suitably equipped, it is passed over for a lower ranked

member in the list. In selecting 4 out of 12 power stations exhaustively, the number of evaluations is  $\frac{12!}{4!\times 8!}$ . The selection of j, l, m and n by the author is  $\{2,5,8,11\}$ . Figure 2.5 is a 3x3 table presenting the graphical evaluations of  $\hat{\underline{v}}_r^T \hat{\underline{u}}_i$ , r=1,2,3, i=1,2,3. Note that the bars in the diagonal charts – i.e. (a), (e) and (i) – are all positive and add to a high value for good damping in each mode. In the off-diagonal graphs, half of the bars are positive and the other half are negative. The opposite polarities help in ensuring that their algebraic sum is close to zero, to provide decoupling.

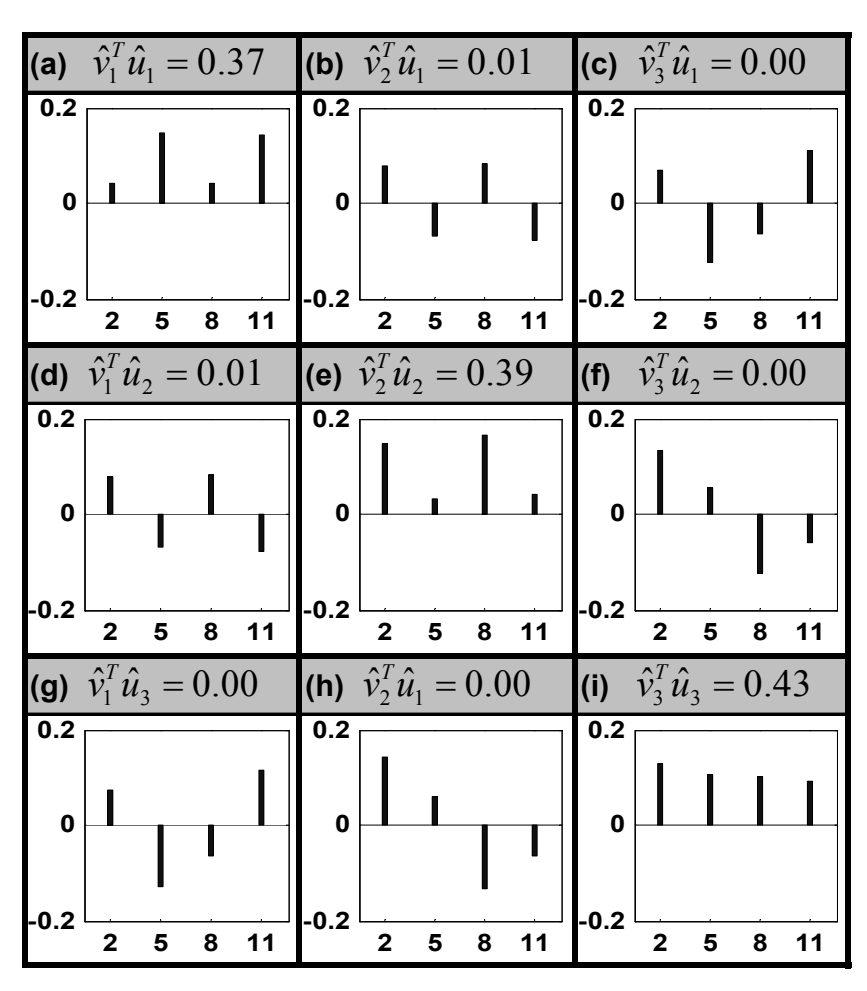


Figure 2.5 Graphical depiction of terms defining decoupling conditions

The quadratic structure of Multiple Modal Selective Method ensures that the decoupling is better than suggested by the results in Figure 2.5 for example, from Figure 2.5(b), the coupling between Mode #1 and #2 is  $\hat{\underline{v}}_2^T \hat{\underline{u}}_1 = 0.01$ . What is finally important is the off-diagonal elements  $\Delta \lambda_{12(1)}$  of the sub-matrix  $[\Delta \Lambda_{11(1)}]$  when compared with diagonal elements  $\Delta \lambda_{11(1)}$ . Taking  $\hat{\underline{v}}_1^T \hat{\underline{u}}_1 = 0.37$  from Fig.5 (a) and applying (2.28), the lambda-ratio<sub>12(1)</sub>=0.01×0.01/(0.37)<sup>2</sup>=0.00073. An attempt has been made to reduce the number of stations from 4 to 3, but the decoupling becomes poor. This is because positive sum with negative sum do not cancel. Figure 2.5 shows this very clearly when power station 2 is removed so

#### 2.7 CONCLUSION

that  $\{2,5,8,11\}$  becomes  $\{5,8,11\}$ .

Besides singling out the targeted modes to be heavily damped, the Multiple Selectivity Method ensures that all the other modes will have their eigenvalues shifted to the left in the complex s-plane (see equations (2.29) and (2.30)). Therefore, the fast modes will never be destabilized on account of the Multiple Selectivity Method. As the fast modes are assumed to be damped by traditional PSS, this is a fail-safe feature.

# CHAPTER 3

MULTIPLE MODAL SELECTIVITY
METHOD: TEST RESULTS

#### 3.1 Introduction

This chapter presents a series of simulation results and eigenvalue evaluations to validate the claims in chapter 2. The chapter is organized as follows:

#### 3.1.1 Tests of Multiple Selectivity

First, tests have been performed on the 12-generators of Figure 2.1 to validate the claims on Multiple Modal Selectivity method. Then more demanding tests have been performed on the well known 16-machine 68 bus System [54] and the 4-Generator System of SymPowerSystems toolbox [71].

#### 3.1.2 Tests on Robustness

Section 3.4 shows that even if  $\underline{\hat{u}}_k$  or  $\underline{\hat{v}}_k$  in  $-\sigma_k \underline{\hat{u}}_k \underline{\hat{v}}_k^T$  of the Central Control of Figure 2.4 is not known accurately, the Global PSS should do its job as long as  $\underline{\hat{v}}_k = [diag(\underline{h})]\underline{\hat{u}}_k$ . Using digital simulations and eigenvalue evaluations, this chapter shows that the Multiple-Selectivity Method provides robust damping as claimed.

The robustness claim is validated by showing that the Global PSS continues to damp the 12-generator system when circuit breakers sever a tie-line of Figure 2.1.

The chapter is organized as follows:

In section 3.2, three of the twelve generators of Figure 2.1 have been chosen to damp the three lowest frequency modes. It should be noted that none of the modes have damping without the Global PSS. The results show that while the Global PSS damps the targeted modes heavily, it also damps the high frequency modes, although very lightly.

Section 3.3.1 presents the results of eigenvalue analysis on a 16-machine 68 bus System. Section 3.3.2 presents simulation of recovery after opening circuit breakers of a faulted line of the 4-Generator System. Robustness of the Global PSS is discussed in section 3.4.

#### 3.2 RESULTS FROM NUMERICAL TESTS

# 3.2.1 Simulations - No Decoupling

In the first instance, simulation results are presented for the case where reducing the number of controlling power stations to 3 is preferred to having 4 controlling stations. The search for the best location of the 3 stations, based on  $W = \Sigma_{\sigma}$ , yields power stations (5, 8, 11). The equations simulated are [A]+[ $\Delta$ A] with excitation due to an arbitrary initial value  $\Delta \underline{\mathbf{x}}(0)$ . The modal graphical displays are obtained from  $\underline{v}_{i}^{T}\underline{\mathbf{x}}(t)$ , i=1,...12.

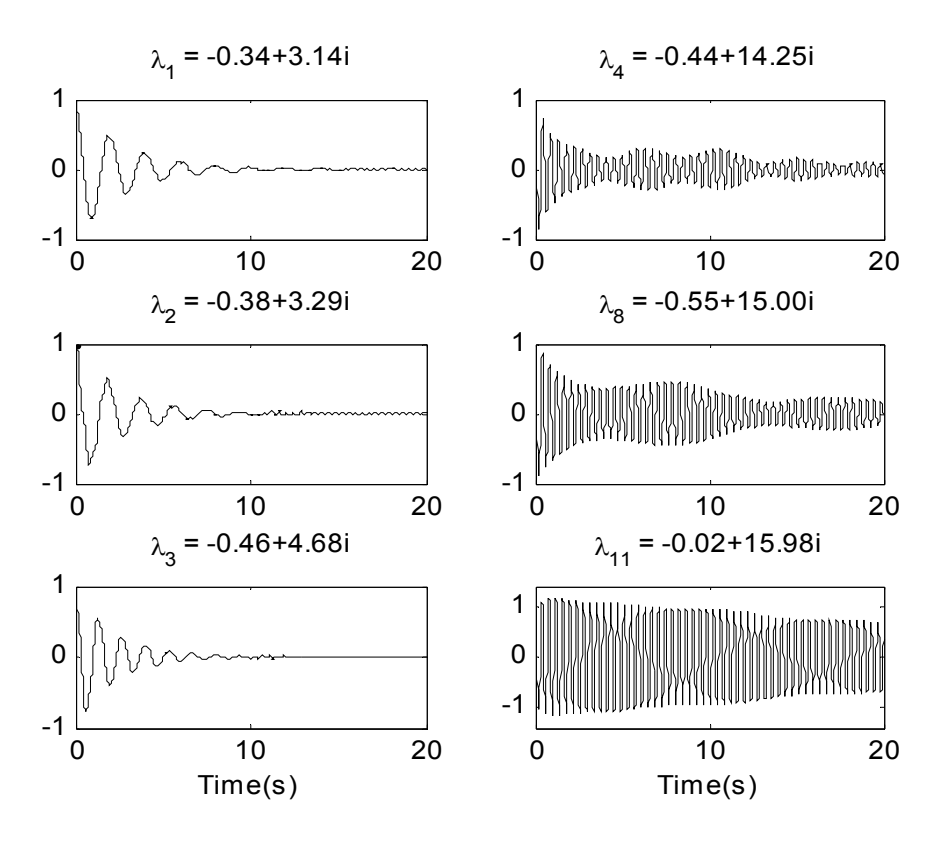


**Figure 3.1** Modal responses following excitation of all modes for power stations {5,8,11}. No decoupling in targeted slow modes.

Figure 3.1 shows the responses of the targeted slow modes #1, #2, #3 (in the left column) together with a sample of the fast modes #4, #8, #11. The simulation results show that the control of Figure 2.4 provides significant damping of the targeted slow modes. The high frequency modes (#4, #8, #11) are also damped, although only lightly. The control experiment consists of repeating the simulation without the controls of Figure 2.4. The results show that none of the modes has damping.

#### 3.2.2 Eigenvalue Evaluation - No Decoupling

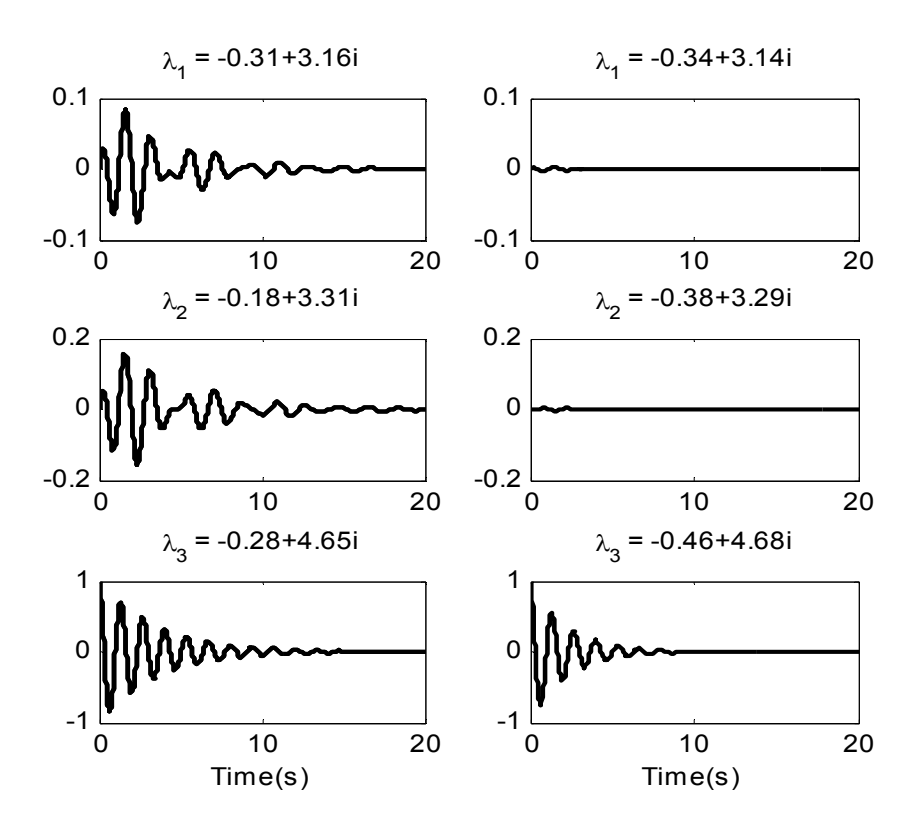
Table 3.1 lists the eigenvalues of [A]+[ $\Delta$ A]. Comparing the modal frequencies in Table 3.1 with those of Table 2.3, the feedback loop does not markedly change the system modal frequencies. But it adds significant damping to the targeted modes (#1,#2, #3), as well as some fast modes.

Table 3.1 System closed loop eigenvalues ( $\sigma_1 = \sigma_2 = \sigma_3 = -5$ )

Mode	$\operatorname{Real}(\lambda)$	$\pm \operatorname{Imag}(\lambda)$	Mode	$\operatorname{Real}(\lambda)$	$\pm \operatorname{Imag}(\lambda)$
1	- 0.3428	3.143	7	- 0. 3841	14.631
2	- 0.3821	3.291	8	- 0.5555	15.003
3	-0.4599	4.679	9	- 0.0537	15.169
4	- 0.4372	14.252	10	- 0.0786	15.666
5	- 0.0830	14.386	11	- 0.0258	15.978
6	- 0.1642	14.5521	12	- 0.0013	

Table 3.1 is only a sample of the extensive tests that has been conducted. In all cases, involving the many sets of parameters of the system, all modes have positive damping; a situation consistent with (2.30), which follows the conclusion that the trace of  $[A]+[\Delta A]$  is always negative.

#### 3.2.3 Simulations - With Decoupling



**Figure 3.2** Response of slow modes #1, #2, #3 for excitation of mode #3. Left—no decoupling {5,8,11}; Right—with decoupling {2,5,8,11}.

Figure 3.2 compares the left hand column, which has the results of "no decoupling" for connecting power stations  $\{5,8,11\}$  with the right hand column, which bears the results of "with decoupling" for connecting power stations  $\{2,5,8,11\}$ .

The simulations are the responses of the the slow modes following excitation of mode #3 only. The excitation of the i<sup>th</sup> mode in isolation is by initial state  $\Delta \underline{\mathbf{x}}(0) = \underline{\mathbf{u}}_3$ . Modes #1 and #2 are virtually undisturbed in the right hand graphs.

Simulation experiments have been performed in which mode #1 is excited in isolation and then with mode #2 excited in isolation. Because the results are similar, they are not presented here. The inability of {5, 8, 11} to provide decoupling is very clear from Figure 2.5. In all the off-diagonal graphs, when the bar of power station 2 is missing, the summation cannot approach zero.

# 3.3 PERFORMANCE ON POWER SYSTEMS WITH REALISTICALLY MODELED GENERATORS

#### 3.3.1 Tests on a 16-machine 68-bus System (Eigen-analysis)

To show that the Multiple Selectivity Method functions in a realistic system where each generator station has detailed models of the alternator, governor system, excitation control and power system stabilizer, the author has turned to eigenvalue analysis of the 16-machine system (86 transmission lines, 68 buses) in MatNetEig toolbox of Matlab, which is available in [54].

The system data for this test, as indicated in [54], has been borrowed from [72]. The objective of the test is to increase the damping of the system three lowest frequency modes. The mode shapes shown in Figure 3.3 correspond to the lowest three modes and can be generated directly using the toolbox applications. Stations #5, #13, #14 and #16 are selected to fulfill the stated objective.

After sorting through hundreds of eigenvalue pairs solved by the MatNetEig toolbox, the eleven electromechanical eigenvalues are identified and plotted as encircled dots in Figure 3.4.

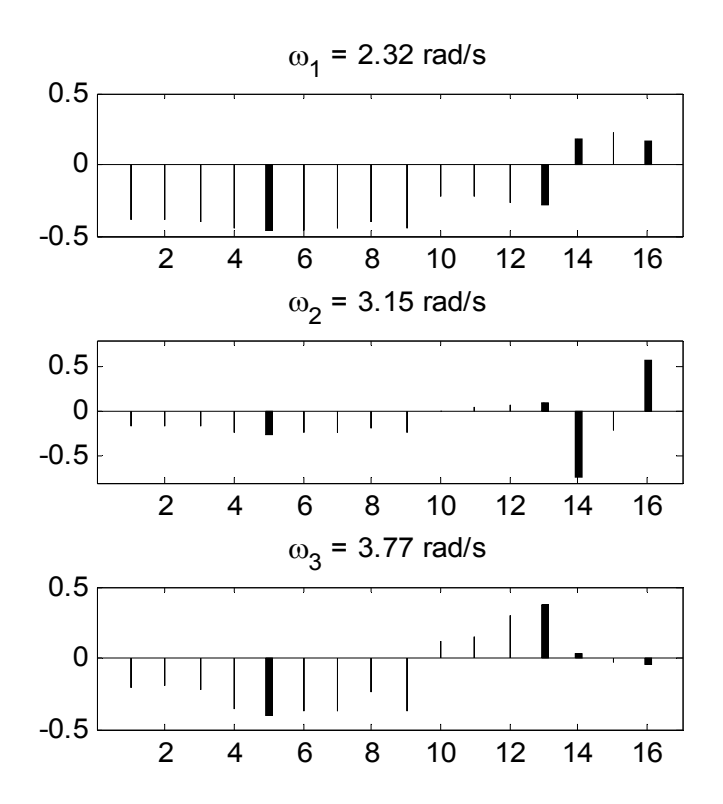


Figure 3.3 Mode shapes of three lowest frequencies

As the feedback loop gains  $\sigma_1 = \sigma_2 = \sigma_3$  are increased from zero, eigenvalues of the 3 target low-frequency modes migrate to the left, indicating increased damping. As predicted by the theory, the other electromechanical modes are only marginally affected by the target modes' movements and remain largely decoupled. Although the 3 modes are lightly coupled, their damping is increased. The increased damping comes from (2.29) and (2.30) which is a feature of the Multiple Modal Selectivity Method. The dynamics of the non-electromechanical modes are

influenced very little by the changes in the dynamics of the electromechanical modes.

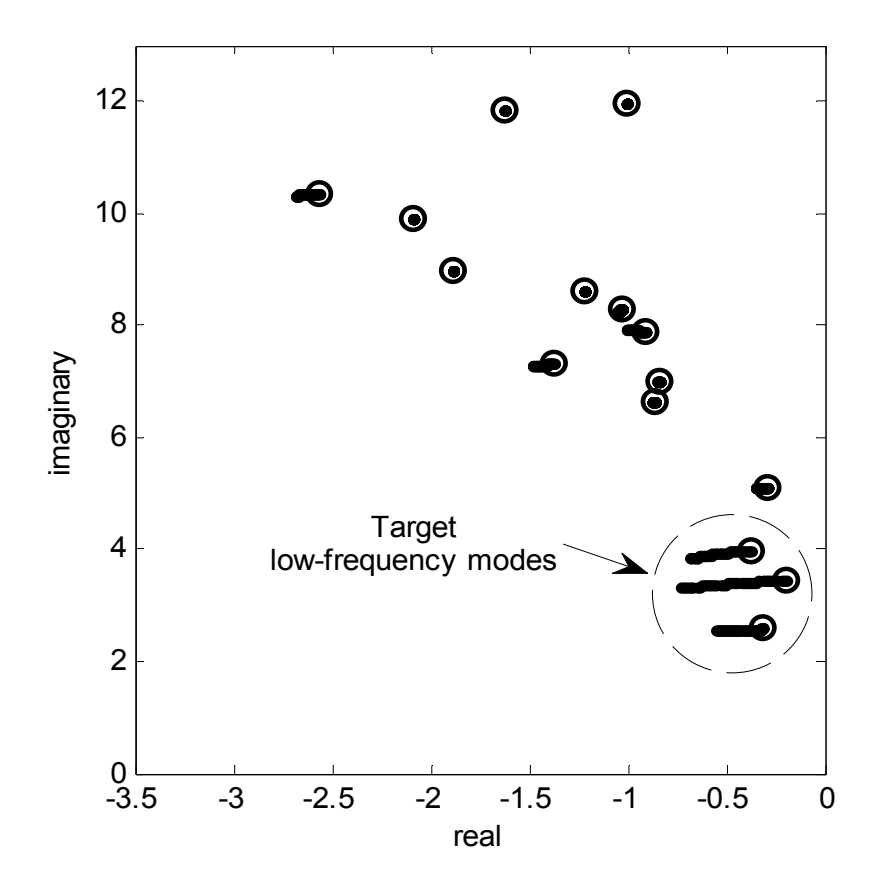


Figure 3.4 Electromechanical eigenvalues

# 3.3.2 Test by 4-Generator System (Time-domain Simulation)

To validate the approach via time-domain simulation, the authors make use of the 4-generator system shown in Figure 3.5 which is taken from [71, 73]. SimPowerSystems toolbox [71] has the same level of detailed modeling of system components as the MatNetEig toolbox. One can readily show that for this case generator and generator sub-system modes are strongly damped by the PSS.

In order to have an electromechanical modal frequency beyond the effective range of the PSS, the normalized inertias of the generators are artificially increased to 100s.

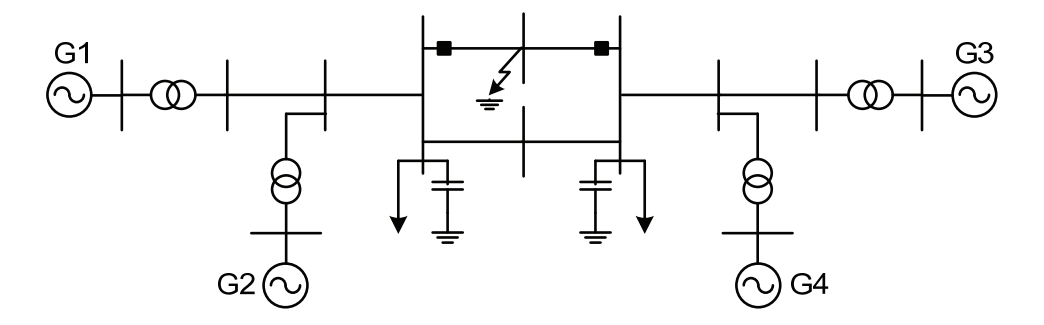
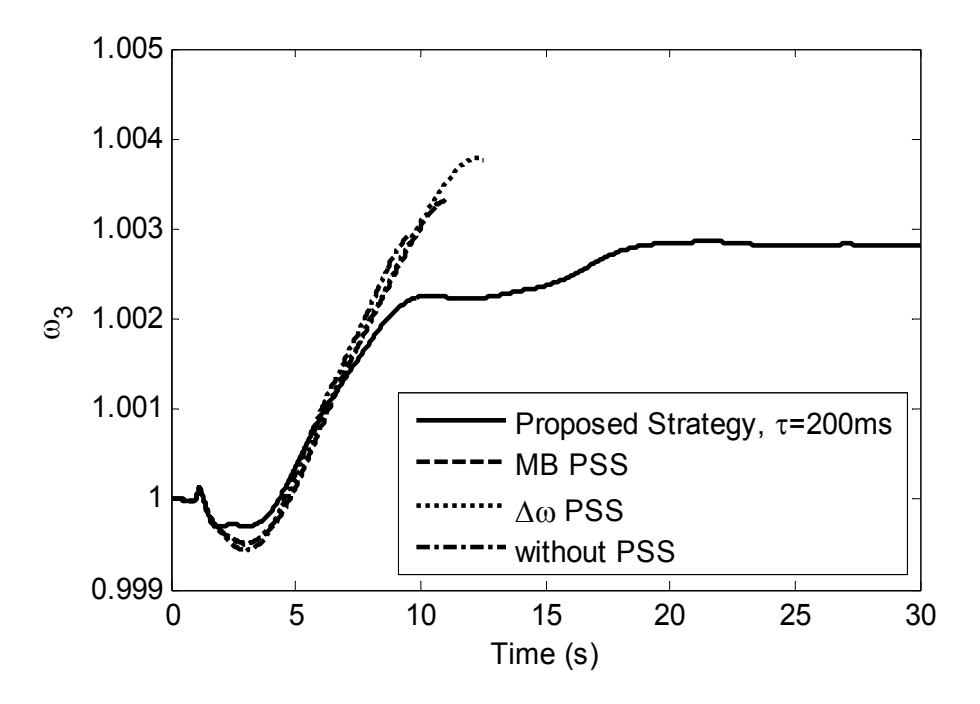


Figure 3.5 Four-Generator System [71, 73]

At a low modal frequency of 0.1 Hz (approaching wide-area oscillation), the simulations in Figure 3.6 show that the system is unstable for 3 cases: without PSS, with speed feedback ( $\Delta\omega$  PSS), and with multi-band PSS (MB PSS).

The test scenario calls for clearing a 3-phase solid ground fault at t=1s at the location shown in Figure 3.5. The system protection clears the fault 133ms later by disconnecting the affected line-section. In applying the Multiple Selectivity Method, the signals generated by the Central Control form the inputs of the PSS on generator  $G_1$  and  $G_3$ . Even with a delay time of 200 ms (representing wide-area control loop latency), the proposed strategy remains stable.

As the above two tests are performed on power systems with fully modeled generators, they support the notion that the Multiple Modal Selectivity Method can be applied to realistic power systems.



**Figure 3.6** Simulation of pu speed of G3 after occurrence and clearing of three phase ground fault.

#### 3.4 ROBUSTNESS OF THE METHOD

In Section 2.3, it has been assumed that the eigenvector  $\underline{\mathbf{u}}_{\mathbf{k}}$  is known precisely. One can replace  $\underline{\mathbf{u}}_{\mathbf{k}}$  by an approximation  $\underline{\mathbf{w}}_{\mathbf{k}}$  and define  $\hat{\underline{u}}_{wk} = \begin{bmatrix} C_{11} \end{bmatrix} \underline{w}_{k}$  and  $\hat{\underline{v}}_{wk} = \begin{bmatrix} diag(\hat{\underline{h}}) \end{bmatrix} \hat{\underline{u}}_{wk}$ . The control gain matrix, in this case, is  $[K_{11(k)}] = -\sigma_{k} \hat{\underline{u}}_{wk} \hat{\underline{v}}_{wk}^{T}$ . From (2.26), one obtains

$$\Delta \lambda_{ii(k)} = -\sigma_k(\hat{\underline{v}}_i^T \hat{\underline{u}}_{w_k})(\hat{\underline{v}}_{w_k}^T \hat{\underline{u}}_i)$$
(3.1)

As  $\underline{\hat{u}}_{i}^{T}[diag(\underline{\hat{h}})]\underline{\hat{u}}_{wk} = \underline{\hat{u}}_{wk}^{T}[diag(\underline{\hat{h}})]\underline{\hat{u}}_{i}$  it follows that  $\Delta\lambda_{ii(k)} \leq 0$  for all i=1,2...N, including i=k. This result is the same as (2.30). As in Section 2.3, the diagonal elements of  $[\Delta\Lambda_{11(k)}]$  are all not positive and the trace of  $[\Lambda_{11}]+[\Delta\Lambda_{11(k)}]$  does not

have a real positive part. Therefore, the system is as stable as in (2.25) when the exact eigenvector  $\underline{\mathbf{u}}_k$  is applied. The eigenvectors change with load which affect [A] in the terms  $V_{i0}V_{j0}\cos(\delta_{i0}-\delta_{j0})$ . In practice, bus voltages are kept close to their nominal values and  $(\delta_{i0}-\delta_{j0})$  hardly goes beyond the range (+15°,-15°). Since  $\cos(0^\circ)=1$  and  $\cos(\pm 15^\circ)=0.965$ , at the extreme this can represent a 4% parameter change.

Not only is Multiple-Selectivity Method robust with respect to small parameter variations but it is robust for major changes such as: (i) a disconnected local line; (ii) a disconnected tie-line.

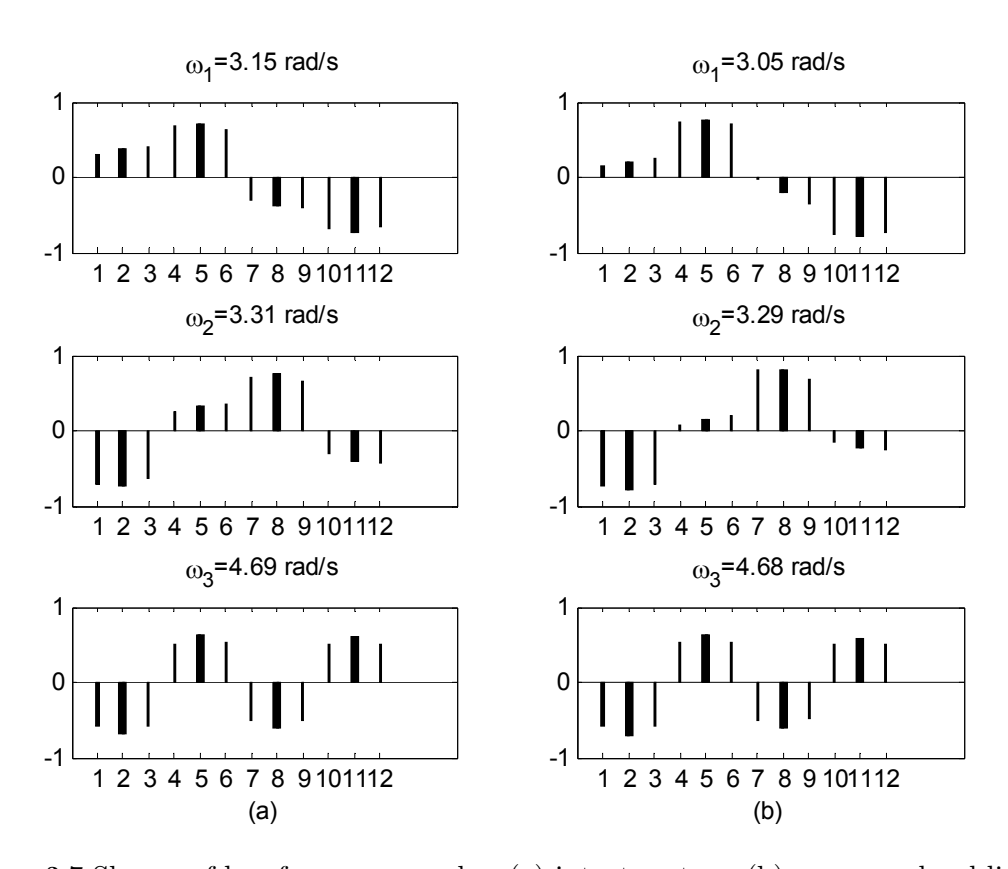


Figure 3.7 Shapes of low frequency modes: (a) intact system; (b) one open local line)

#### 3.4.1 Sensitivity of Mode Shapes to a disconnected local line

Figure 3.7 shows in (a) the original mode shapes of the targeted modes. In (b) it shows the same modes when a local line (in one of the areas) is opened. Although Stations #2, #5, #8 and #11, which are shown with heavy bars, will pick up different numbers from the designed values of the Central Controller of Figure 2.4, from(3.1), the slow modes will still be positively damped. The amount of positive damping is no longer the same, but the difference is not a big amount. Time domain simulation results in Figure 3.8, confirm this.

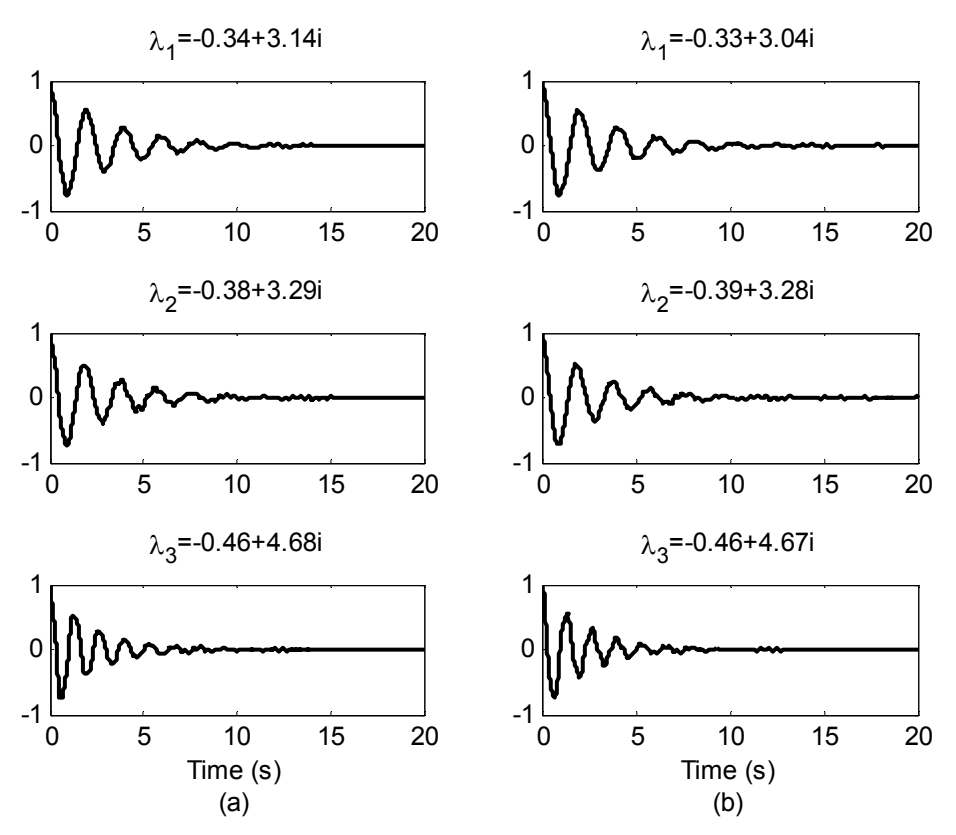


Figure 3.8 Slow modes damped by Multiple Selectivity Control: (a)Intact system (b)System with disconnected local line

#### 3.4.2 Sensitivity of Mode Shapes to disconnected tie-line

In order to leave no doubt that robustness holds for disconnection of tie-lines, results are presented for disconnection of every one of the tie-lines in the 12-generator system of Figure 2.1. To understand why there is the robustness, the targeted mode shapes of the four cases of disconnection of tie-lines (Figure 2.1) are presented in Figure 3.9, 3.11, 3.13, and 3.15. In particular, the stations #2, #5, #8, and #11 are highlighted.

In these Figures, although modes shapes of intact system are different from the systems with open tie-line, the underlying fact which emerges is that the mode shapes reflect the 3 ways in which the 4 areas oscillate against each other. From the oscillations picked up by stations #2, #5, #8, and #11 the central controller of Figure 2.4 recognizes the inter-area oscillations and sends the appropriate damping signals.

#### 3.4.3 Time Domain Proof of Robustness

Figure 3.10 shows the damping of the slow modes when one tie-line has been disconnected. This experiment has been repeated 4 times, each time for one of the 4 tie-lines disconnected. The system is positively damped for each case.

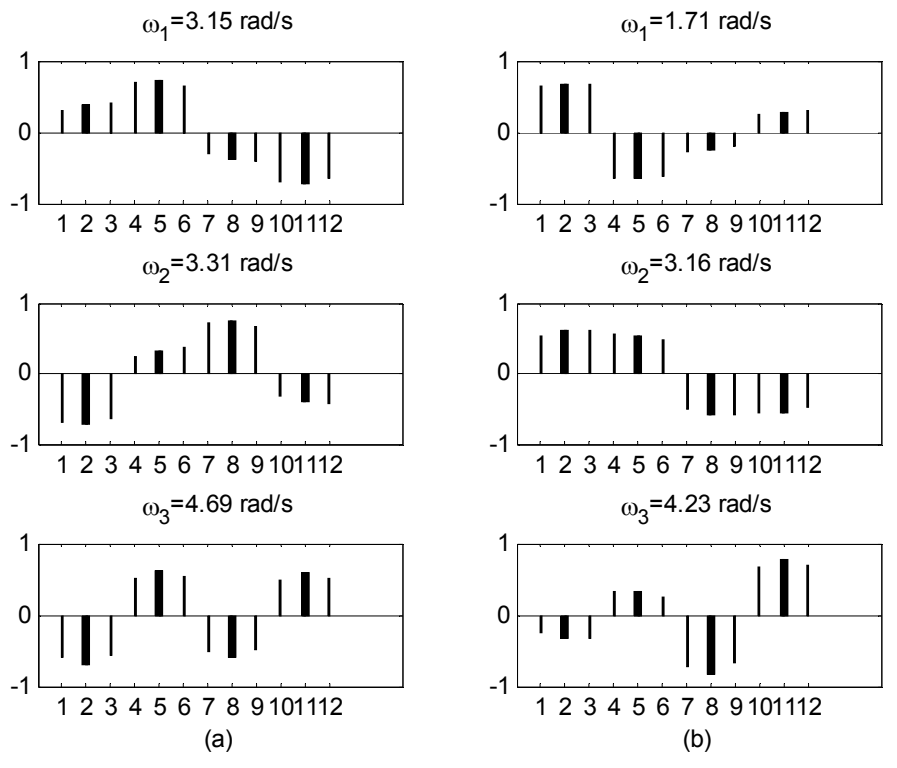


Figure 3.9 Shapes of low frequency modes: (a) intact system; (b) open 1<sup>st</sup> tie-line)

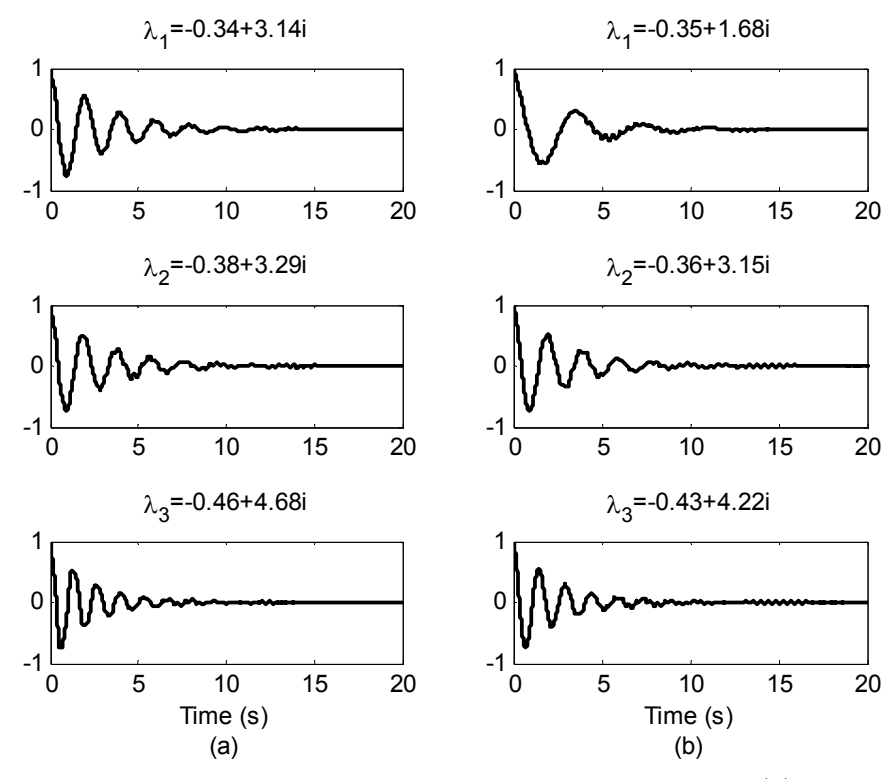


Figure 3.10 Slow modes damped by Multiple Selectivity Control: (a)Intact system (b)System with  $1^{st}$  tie-line disconnected

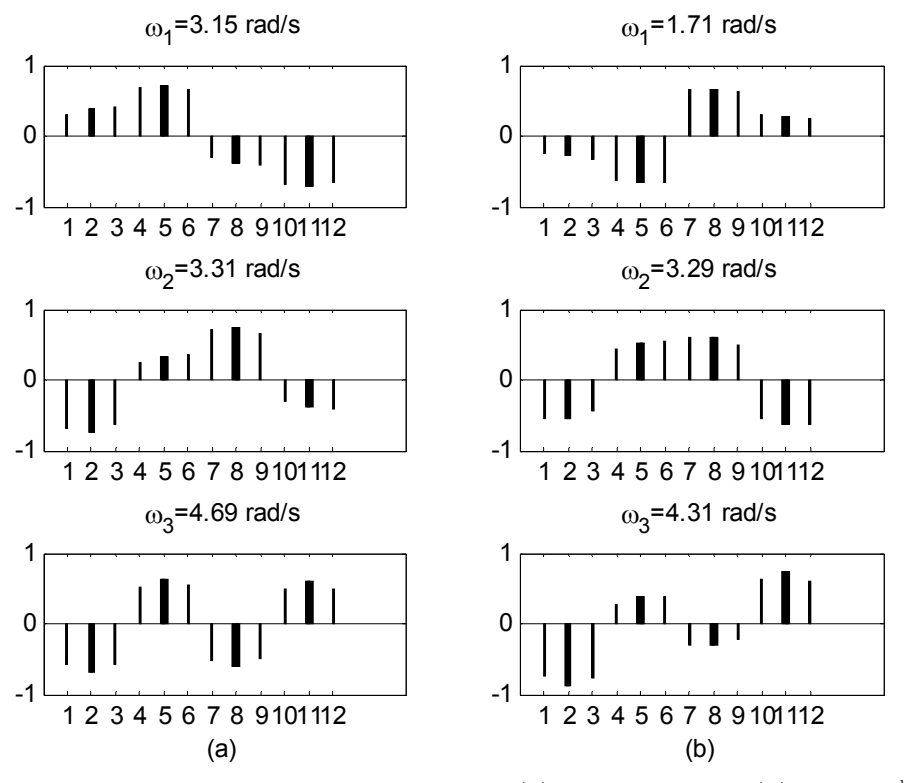


Figure 3.11 Shapes of low frequency modes: (a) intact system; (b) open 2<sup>nd</sup> tie-line)

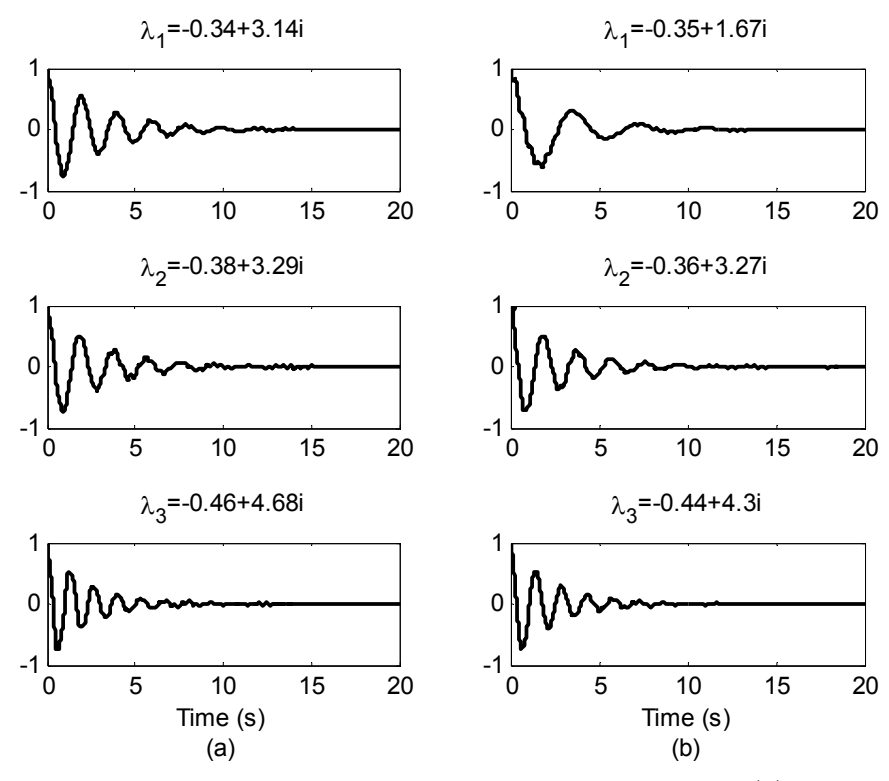


Figure 3.12 Slow modes damped by Multiple Selectivity Control: (a) Intact system (b) System with  $2^{nd}$  tie-line disconnected

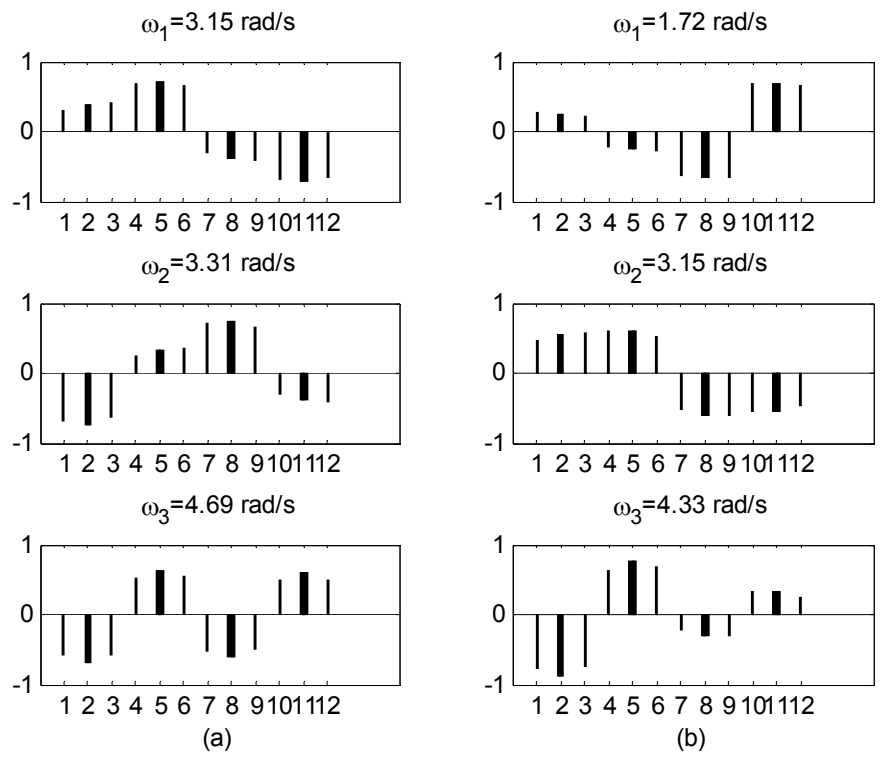


Figure 3.13 Shapes of low frequency modes: (a) intact system; (b) open 3<sup>rd</sup> tie-line)

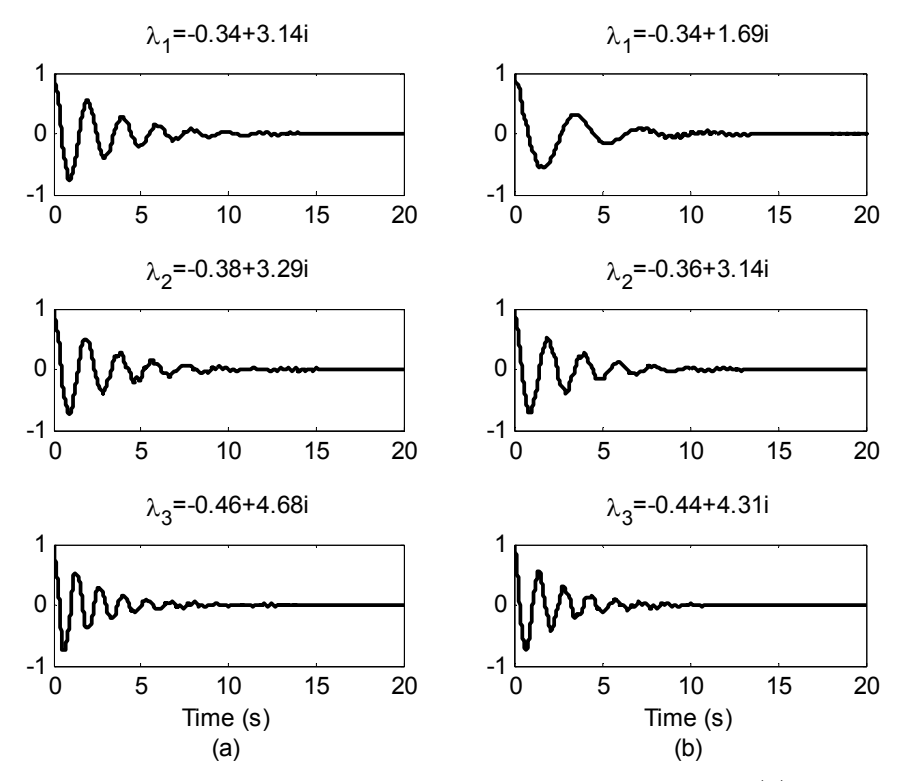
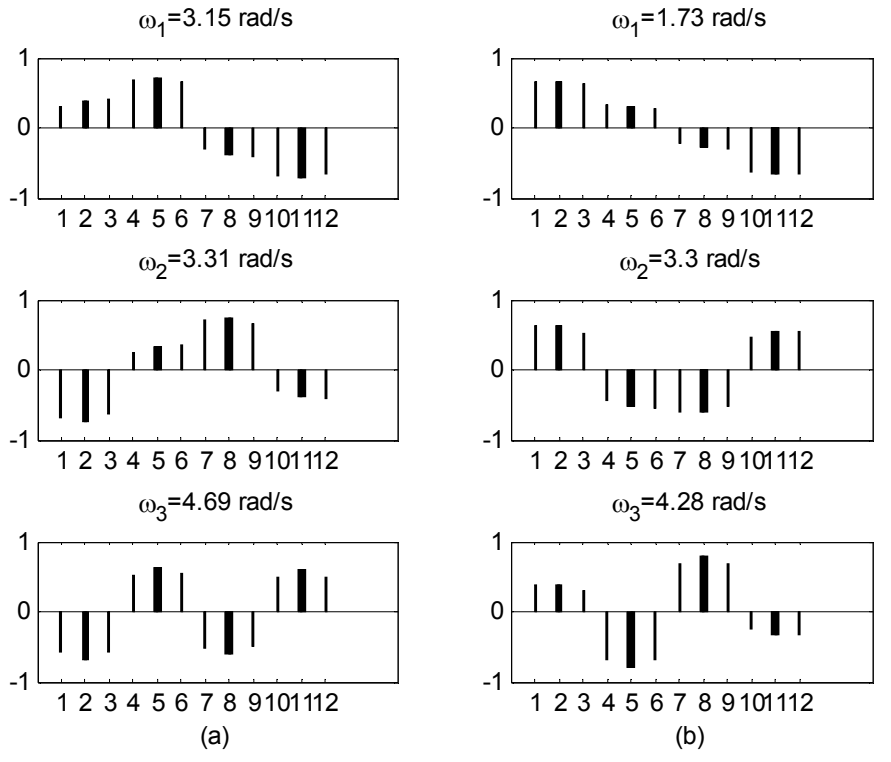


Figure 3.14 Slow modes damped by Multiple Selectivity Control: (a) Intact system (b) System with  $3^{\rm rd}$  tie-line disconnected



 $\textbf{Figure 3.15} \ \text{Shapes of low frequency modes: (a) intact system; (b) open $4^{th}$ tie-line)}$ 

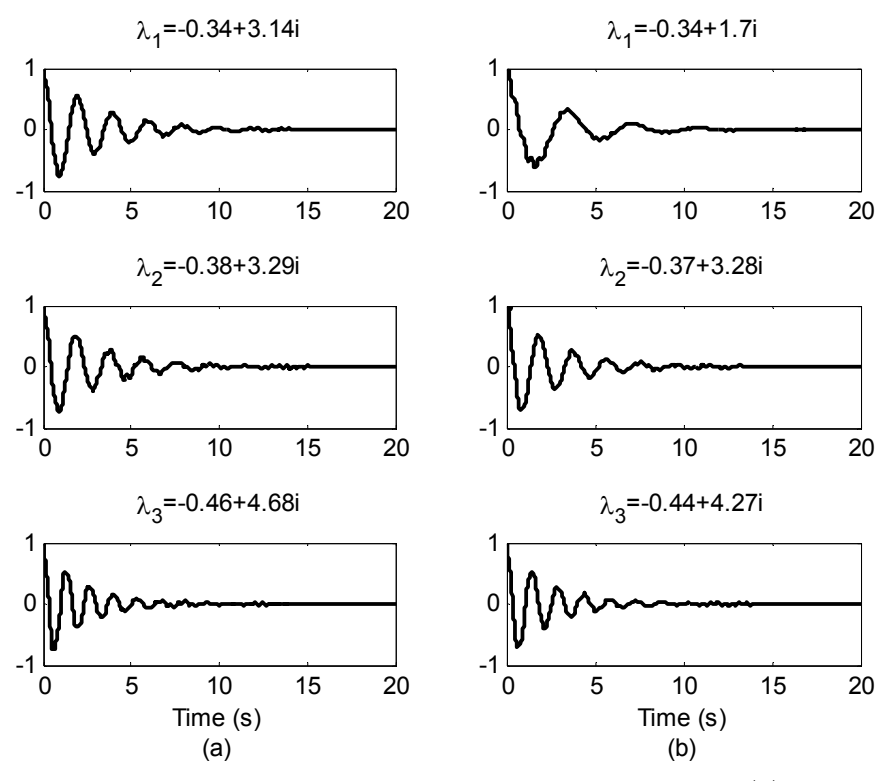


Figure 3.16 Slow modes damped by Multiple Selectivity Control: (a) Intact system (b) System with  $4^{th}$  tie-line disconnected

## 3.4.4 Proof by Eigenvalue Evaluations

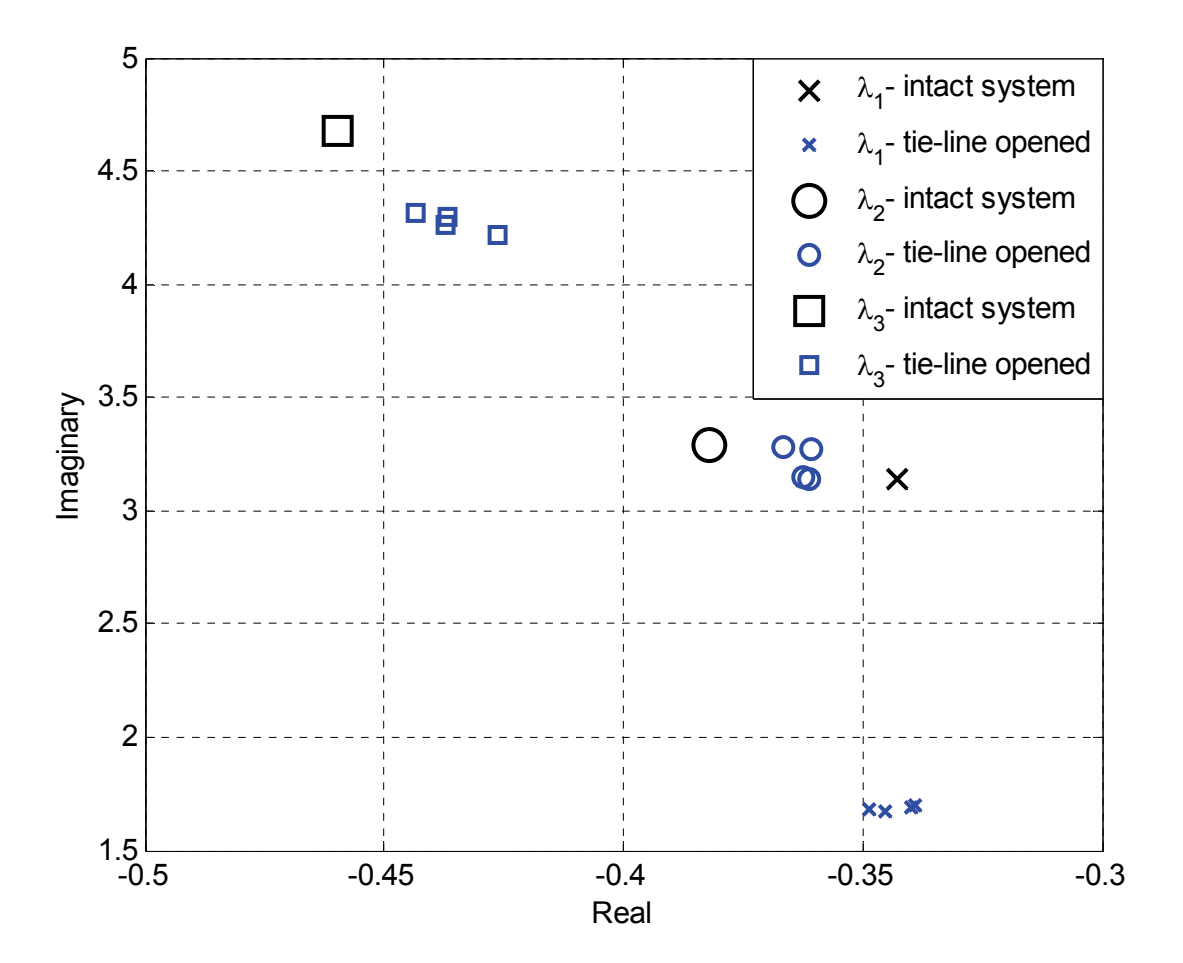


Figure 3.17 Slow modes Comparison of eigenvalues of 3 slow modes—intact system with system with disconnected tie-line (4 cases).

Figure 3.17 plots on the complex s-plane the 3 slow modes identified by square, circle and x symbols. The large symbols are for the intact system. The 4 additional symbols are for the 4 cases of having one of the 4 tie-lines disconnected at one time. Although positively damped, the damping is reduced. The slowest mode has its frequency reduced significantly.

#### 3.5 CONCLUSION

The Multiple Modal Selectivity Method has been presented and its claims have been validated by eigenvalue analysis and simulations in realistic systems involving 16 generators, each modeled by high order equations and equipped with power system stabilizers, etc. The claims are: (i) using WAMS-based controls, central control can damp the very low frequency oscillations of inter-area modes; (ii) the damping of the inter-area modes can be decoupled; (iii) the only information required is the eigenvectors of the target inter-area modes; (iv) only a limited number of power stations are required for providing speed measurements and implementing the control feedback signals; (v) in damping the targeted inter-area modes, the other modes receive positive damping, although PSS is already there to damp the fast modes.

A high order of selectivity is achieved via multiple discrimination stages: (i) speed measurements that provide best feedback signals; (ii) feedback gains that discriminate the observed signal and send control signals selectively; (iii) use power stations best placed to implement the controls.

#### 3.5.1 Robustness

Robustness has been demonstrated in two cases: 1) Disconnection of a local line;
2) Disconnection of a tie-line. This robustness is a significant feature of the Multiple Modal Selectivity Method.

CHAPTER 4

# DAMPING CAPABILITY OF RENEWABLE ENERGIES AS AFFECTED BY POINT OF INSERTION

#### 4.1 Introduction

Control strategies, such as the Multiple Modal Selectivity Method of chapter 2, by themselves are insufficient. In order to damp electromechanical oscillations in a power system, the control signals must be backed by adequate active and/or reactive power. In this respect, when sustainable energy technologies reach high penetration, the power electronically controlled complex powers from their frequency changers (VSCs) can be counted on to help the conventional power plants [35, 37, 74-80]. A preliminary assessment, based on simulation studies on the 39 bus, 10 generator—New England Test System, shows that the damping capability of sustainable energy technologies [81] is determined by their locations. This chapter confirms the simulation studies [65, 81]. It further shows that the locations which affect the damping capability are evident in the algebraic expressions in the close form formulation which is derived in this chapter.

The sustainable energy technology researched on in the Power Energy Research Lab is wind energy. As wind velocity is stochastic, before considering it for damping, research in [82] has established that the output power of a wind farm can be closely controlled. Figure 4.1 shows that there are hourly periods when the output power of a wind farm (comprising 24 wind turbine generators) can be regulated by a combination of power electronic control over the generators and pitch angle control of the wind-turbine blades.

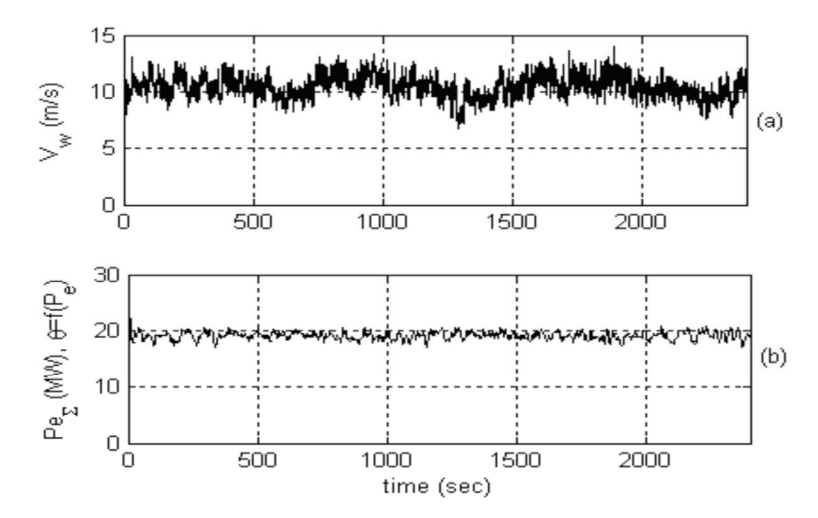


**Figure 4.1** 2500-second simulation of wind farm, from [82]: (a) wind velocity; (b) wind farm (24 WTGs) output.

Furthermore, as Figure 4.2 shows the wind farm can deliver 0.2 Hz auxiliary power, intended for damping operation. In addition to instantaneous power from wind velocity, the research of [82, 83] shows that the kinetic energy in the high inertia wind turbine blades ( H≅4 seconds) possess standby storage power to draw on in the 5 second duration of the Global PSS operation.

The preliminary assessment of [81] has been followed by further validation by simulations [65]. The research of [65] and chapter 2 makes use of small signal linearization. In order to find out if their conclusions apply beyond the assumptions of small signal linearization, this chapter develops a methodology which does not depend on small signal linearization.

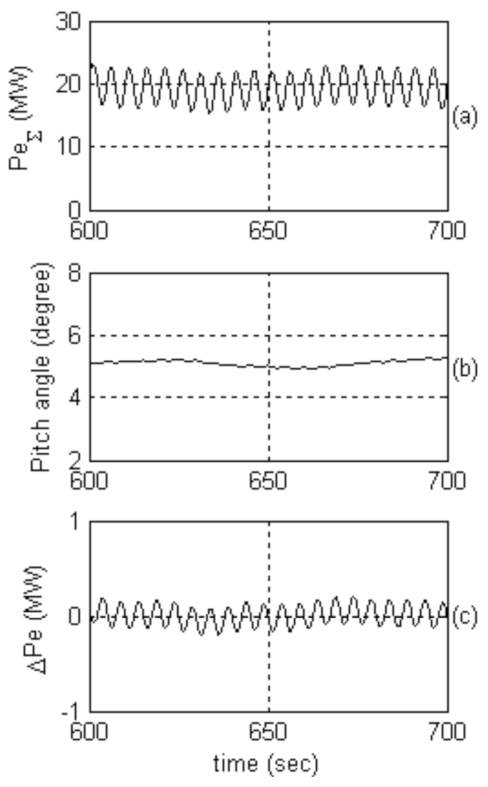


**Figure 4.2** Auxiliary Power for Damping, from [82]: (a) wind farm power output; (b) pitch angle of turbine blade; (c) damping power from individual WTG.

It represents the sustainable energy technology by an ideal complex power load or source (negative load) inserted along a transmission line between two conventional generators and derives a close form formulation of the dynamic interaction.

For decades, power engineers have used the archetype model of a single generator "swinging" against an infinite bus to bring out the concepts of synchronizing power, small signal stability and transient stability (equal area criterion). The derived close form formulation has the potential of being another archetype model from which useful analytical conclusion can be drawn in the future.

In this chapter and in part of chapter 5, the close form nonlinear formulation is retained for two purposes: (i) to confirm the results of [65] which has been obtained from small signal linearization; (ii) to gain analytical insights (which the numerical evaluations of [65] cannot) regarding damping effectiveness in relation to the point of connection of the transmission line.

This chapter is organized as follows:

Section 4.2 derives the nonlinear formulation. Section 4.3 shows that their predictions are better viewed by a phase-plane diagram [60]. Section 4.4 brings out the concept of nonlinear damping using phase-plane diagram. Section 4.5 presents two location factors (see Figure 4.6) to give an analytical explanation for the difference in damping effectiveness by active power modulation and by reactive power modulation.

#### 4.2 COMPLEX POWER LOAD IN TRANSMISSION LINE

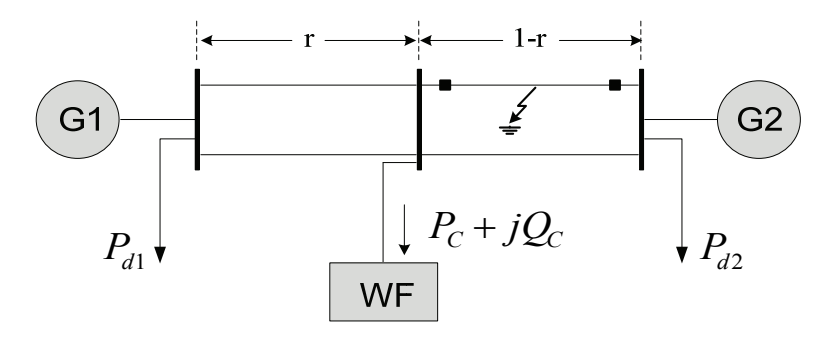


**Figure 4.3** Complex Power Load at distance rL from G1, 0 < r < 1.0.

Figure 4.3 shows a positive complex load  $P_c+jQ_c$  located at distance rL (0< r < 1.0, L is line length) from generator  $G_1$ . In modeling a wind farm, the complex power of the load will be negative. Voltages, complex powers and impedances are per-unitized (for kV-base and MVA-base, see Appendix B). Assuming the reactance of the lossless double line is  $jX_L$  and the transformer reactances on both ends to be  $jX_T$ , the impedance on G1 side is  $jX_1=j(X_T+rX_L)$  and on G2 side is  $jX_2=j(X_T+X_L-rX_L)$ . The voltages of G1 and G2 are  $\tilde{V}_1=V\angle\delta_1$  and  $\tilde{V}_2=V\angle\delta_2$ . As [84] has shown, the power electronic converters of a renewable energy installation can be modeled as a voltage source,  $\tilde{V}_c=V_c\angle\delta_c$ . In simulation tests, a 3-phase-to-ground fault is simulated at a point shown and the circuit breakers on both sides are opened on clearing the fault within 100ms.

#### 4.2.1 Dynamic Equation of System

The prime-mover powers of  $G_1$  and  $G_2$  are  $P_{m1}$ ,  $P_{m2}$  and the load powers are  $P_{d1}$ ,  $P_{d2}$  respectively. For simplicity, it is assumed that the inertia constants are equal, i.e.  $H_1$ = $H_2$ =H. The rotor speeds,  $\omega_1$  and  $\omega_2$ , of generators  $G_1$  and  $G_2$  are governed by Newton's Law of Motion:

$$\frac{2H}{\omega_{0}}\frac{d\omega_{1}}{dt} = P_{m1} - P_{d1} - P_{1} \tag{4.1}$$

$$\frac{2H}{\omega_0} \frac{d\omega_2}{dt} = P_{m2} - P_{d2} - P_2 \tag{4.2}$$

where  $P_1$  and  $P_2$  are the powers transferred by  $G_1$  and  $G_2$  respectively in the direction to the complex load. Defining

$$\delta_{1-2} = \delta_1 - \delta_2 \tag{4.3}$$

$$\omega_{\text{\tiny 1-2}} = \omega_{\text{\tiny 1}} - \omega_{\text{\tiny 2}} \tag{4.4}$$

$$\frac{d\delta_{_{1-2}}}{dt} = \omega_{_{1-2}} \tag{4.5}$$

and subtracting (4.2) from (4.1), one has

$$\frac{2H}{\omega_0} \frac{d\omega_{1-2}}{dt} = (P_{m1} - P_{d1}) - (P_{m2} - P_{d1}) - (P_1 - P_2) \tag{4.6}$$

Assigning the voltages of generators in Figure 4.3 to be  $\tilde{V_1} = V \angle \delta_1$ ,  $\tilde{V_2} = V \angle \delta_2$  and load to be  $\tilde{V_C} = V_C \angle \delta_C$ , the currents from G1 and G2 to the load are:

$$\tilde{I}_{1} = \frac{\tilde{V}_{1} - \tilde{V}_{C}}{jX_{1}} \tag{4.7}$$

and

$$\tilde{I}_2 = \frac{\tilde{V}_2 - \tilde{V}_C}{jX_2} \tag{4.8}$$

The complex power of the load is

$$P_{C} + jQ_{C} = \tilde{V}_{C}(\tilde{I}_{1}^{*} + \tilde{I}_{2}^{*}) \tag{4.9}$$

Substituting (4.7) and (4.8) to the complex conjugate of (4.9)

$$jX_{1}(P_{C} - jQ_{C}) = \tilde{V}_{C}^{*} \left[ (\tilde{V}_{1} - \tilde{V}_{C}) + (\tilde{V}_{2} - \tilde{V}_{C}) \left( \frac{X_{1}}{X_{2}} \right) \right]$$
(4.10)

which can be simplified to:

$$\tilde{V}_{C}^{*} = \frac{jX_{1}(P_{C} - jQ_{C}) + \left(1 + \frac{X_{1}}{X_{2}}\right)V_{C}^{2}}{\tilde{V}_{1} + \frac{X_{1}}{X_{2}}\tilde{V}_{2}}$$
(4.11)

Multiplying  $\tilde{V}_{\scriptscriptstyle C}^*$  by  $\tilde{V}_{\scriptscriptstyle C}$  yields a quadratic equation of  $\,V_{\scriptscriptstyle C}^2$ 

$$\left| \tilde{V}_{1} + \frac{X_{1}}{X_{2}} \tilde{V}_{2}^{2} \right|^{2} V_{C}^{2} = \left[ \left( 1 + \frac{X_{1}}{X_{2}} \right) V_{C}^{2} + X_{1} Q_{C} \right]^{2} + X_{1}^{2} P_{C}^{2}$$

$$(4.12)$$

whose solution is:

$$V_{C}^{2} = \frac{S_{1-2} - Q_{C} + \sqrt{Q_{1-2}^{2} - 2Q_{1-2}Q_{C} - P_{C}}}{\frac{1}{X_{1}} + \frac{1}{X_{2}}}$$
(4.13)

For feasible solution, the argument inside the square root must be positive. Also, the positive root yields a physical solution. In calculating  $V_{\scriptscriptstyle C}^2$ , it is assumed that  $\left| \tilde{V}_{\scriptscriptstyle 1} \right| = \left| \tilde{V}_{\scriptscriptstyle 2} \right| = V$ , and  $S_{\scriptscriptstyle 1-2}$  is defined as:

$$S_{1-2} = V^2 \frac{X_1^2 + 2X_1 X_2 \cos(\delta_1 - \delta_2) + X_2^2}{2X_1 X_2 (X_1 + X_2)}$$
(4.14)

Rewriting (4.11) as

$$\tilde{V}_{C}^{*} = \left(\frac{jX_{1}(P_{C} - jQ_{C}) + \left(1 + \frac{X_{1}}{X_{2}}\right)V_{C}^{2}}{\tilde{V}_{1} + \frac{X_{1}}{X_{2}}\tilde{V}_{2}}\right) \left(\frac{\tilde{V}_{1}^{*} + \frac{X_{1}}{X_{2}}\tilde{V}_{2}^{*}}{\tilde{V}_{1}^{*} + \frac{X_{1}}{X_{2}}\tilde{V}_{2}^{*}}\right)$$
(4.15)

which yields:

$$\begin{split} \tilde{V}_{\scriptscriptstyle C}^* \left[ 2 \left( 1 + \frac{X_1}{X_2} \right) S_{\scriptscriptstyle 1-2} \right] &= \left[ \left( \left( \frac{X_1 + X_2}{X_{\scriptscriptstyle C} X_2} \right) V_{\scriptscriptstyle C}^2 + Q_{\scriptscriptstyle C} \right) + j P_{\scriptscriptstyle C} \right] \\ \times \left[ V \left( \cos(\delta_1) + \frac{X_1}{X_2} \cos(\delta_2) \right) - j V \left( \sin(\delta_1) + \frac{X_1}{X_2} \sin(\delta_2) \right) \right] \end{split} \tag{4.16}$$

Substituting  $V_c^2$  from (4.13) in (4.16) and writing  $\tilde{V}_c^* = V_{CR} - jV_{CI}$ , the real and imaginary parts are:

$$\begin{split} V_{CR} &= V \Bigg[ \Bigg( \frac{X_2 \sin(\delta_1) + X_1 \sin(\delta_2)}{2 \Big( X_1 + X_2 \Big)} \Bigg) \Bigg( \frac{P_C}{S_{1-2}} \Bigg) + \Bigg( \frac{X_2 \cos(\delta_1) + X_1 \cos(\delta_2)}{2 \Big( X_1 + X_2 \Big)} \Bigg) \\ &\pm \Bigg( \frac{X_2 \cos(\delta_1) + X_1 \cos(\delta_2)}{2 \Big( X_1 + X_2 \Big)} \Bigg) \Bigg( 1 - 2 \frac{Q_C}{S_{1-2}} - \left( \frac{P_C}{Q_{1-2}} \right)^2 \Bigg)^{\frac{1}{2}} \Bigg] \end{split} \tag{4.17}$$

$$\begin{split} V_{CI} &= V \Bigg[ - \Bigg[ \frac{X_2 \cos(\delta_1) + X_1 \cos(\delta_2)}{2 \Big( X_1 + X_2 \Big)} \Bigg] \Bigg( \frac{P_C}{S_{1-2}} \Bigg) + \Bigg[ \frac{X_2 \sin(\delta_1) + X_1 \sin(\delta_2)}{2 \Big( X_1 + X_2 \Big)} \Bigg] \\ &\pm \Bigg[ \frac{X_2 \sin(\delta_1) + X_1 \sin(\delta_2)}{2 \Big( X_1 + X_2 \Big)} \Bigg] \Bigg[ 1 - 2 \frac{Q_C}{S_{1-2}} - \left( \frac{P_C}{Q_{1-2}} \right)^2 \Bigg]^{\frac{1}{2}} \Bigg] \end{split} \tag{4.18}$$

The power transferred from G1 to the load is:

$$P_{\scriptscriptstyle 1} = (\frac{V \sin \delta_{\scriptscriptstyle 1}}{X_{\scriptscriptstyle L}}) V_{\scriptscriptstyle CR} - (\frac{V \cos \delta_{\scriptscriptstyle 1}}{X_{\scriptscriptstyle L}}) V_{\scriptscriptstyle CI} \tag{4.19}$$

Substituting  $V_{\it CR}$  and  $V_{\it CI}$  from (4.17) and (4.18),

$$\begin{split} P_{1} &= \frac{V^{2}}{2(X_{1} + X_{2})} \{ [\frac{X_{2}}{X_{1}} + \cos(\delta_{1} - \delta_{2})] \frac{P_{C}}{S_{1-2}} \\ &+ \sin(\delta_{1} - \delta_{2}) [1 + (1 - \frac{Q_{C}}{S_{1-2}} - \frac{P_{C}^{2}}{S_{1-2}^{2}})^{\frac{1}{2}}] \} \end{split} \tag{4.20}$$

By interchanging the subscripts 1 and 2, the real power transferred from G2 is:

$$\begin{split} P_{2} &= \frac{V^{2}}{2(X_{1} + X_{2})} \{ [\frac{X_{1}}{X_{2}} + \cos(\delta_{2} - \delta_{1})] \frac{P_{C}}{S_{2-1}} \\ &+ \sin(\delta_{2} - \delta_{1}) [1 + (1 - \frac{Q_{C}}{S_{1-2}} - \frac{P_{C}^{2}}{S_{1-2}^{2}})^{\frac{1}{2}}] \} \end{split} \tag{4.21}$$

Substituting (4.19) and (4.20) in  $(P_1-P_2)$ , one has the equation embodying the dynamics of Figure 4.3.

$$\begin{split} &\frac{2H}{\omega_0}\frac{d\omega_{_{1-2}}}{dt} = (P_{_{m1}} - P_{_{d1}}) - (P_{_{m2}} - P_{_{d1}}) - \frac{V^2}{2(X_{_1} + X_{_2})} \times \\ &\{(\frac{X_{_2}}{X_{_1}} - \frac{X_{_1}}{X_{_2}})\frac{P_{_C}}{S_{_{1-2}}} + 2\sin(\delta_{_{1-2}})[1 + \sqrt{1 - \frac{2Q_{_C}}{S_{_{1-2}}} - (\frac{P_{_C}}{S_{_{1-2}}})^2}]\} \end{split} \tag{4.22}$$

Equations (4.5) and (4.22) are the key equations of this chapter. They constitute the amended archetype. Putting  $P_C$ =0.0 and  $Q_C$ =0.0, (4.22) reverts to the familiar equation of the existing archetype:

$$\frac{2H}{\omega_0} \frac{d\omega_{1-2}}{dt} = (P_{m1} - P_{d1}) - (P_{m2} - P_{d1}) - \frac{2V^2}{(X_1 + X_2)} \sin(\delta_{1-2})$$
(4.23)

#### 4.3 PHASE PLANE METHOD

Because of the  $\sin(\delta_{1-2})$  term on the right-hand side of (4.22), the equations (4.5) and (4.22) are nonlinear. Dividing (4.22) by (4.5), one has the gradient of  $\omega_{1-2}$  with respect to  $\delta_{1-2}$ 

$$\frac{d\omega_{_{1-2}}}{d\delta_{_{1-2}}} = \frac{Numerator}{Denominator} \tag{4.24}$$

where from (4.22)

$$\begin{aligned} Numerator &= (P_{_{m1}} - P_{_{d1}}) - (P_{_{m2}} - P_{_{d1}}) - \frac{V^2}{2(X_{_1} + X_{_2})} \times \\ &\{ (\frac{X_{_2}}{X_{_1}} - \frac{X_{_1}}{X_{_2}}) \frac{P_{_C}}{S_{_{1-2}}} + 2\sin(\delta_{_{1-2}})[1 + \sqrt{1 - \frac{2Q_{_C}}{S_{_{1-2}}} - (\frac{P_{_C}}{S_{_{1-2}}})^2} ] \} \end{aligned} \tag{4.25}$$

and from (4.5)

$$Denominator = \frac{2H}{\omega_0} \omega_{1-2} \tag{4.26}$$

A graphical approach based on the phase-plane method, as illustrated by Figure 4.4, is applied to view its dynamic characteristics.

## 4.3.1 Phase-Plane Diagram

In the  $\omega_{1-2}$ -vs- $\delta_{1-2}$  plane in Figure 4.4, every co-ordinate point  $(\delta_{1-2}, \omega_{1-2})$  has a value by which the Numerator of (4.25) and the Denominator of (4.26) can be computed. The computed gradient of (4.24) forms the slope of the co-ordinate point. Based on (4.5),  $\delta_{1-2}$  increases with time for  $\omega_{1-2} > 0$ . Therefore, an arrow tip is attached to the gradient so that the trajectories on the upper half-plane move to the right. Applying the same argument to the lower half-plane, the arrow heads are attached so that the trajectories move to the left. From any coordinate point  $(\delta_{1-2}, \omega_{1-2})$  in Figure 4.4, the arrow tip points to the direction of the next position  $(\delta_{1-2} + \Delta \delta_{1-2}, \omega_{1-2} + \Delta \omega_{1-2})$  at a later time.

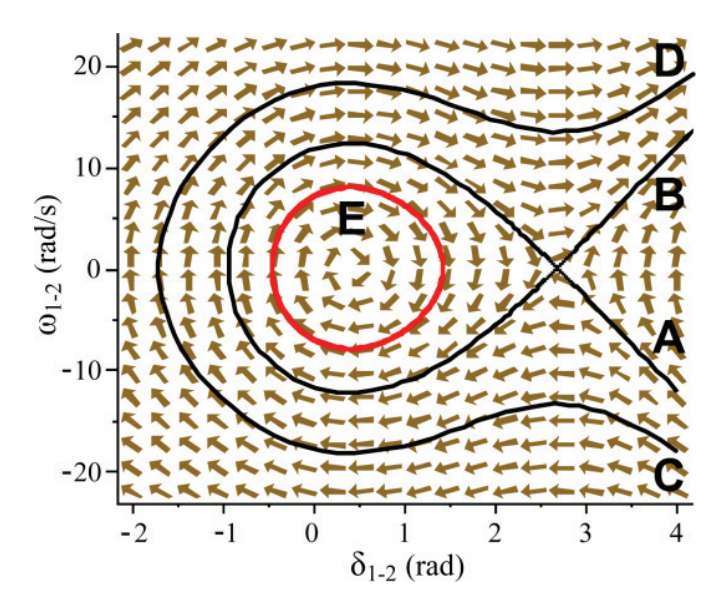


Figure 4.4 Phase-plane representation of Undamped System

# 4.3.2System without Damping

Figure 4.4 is for the case of wind farm power (negative complex power  $P_C = (-P_{C0})$ ,  $Q_C = 0$ ) injected at position r = 0.0 along the transmission line. The numerator of (4.24) is

$$\begin{split} Num &= (P_{m1} - P_{d1}) - (P_{m2} - P_{d1}) - \frac{V^2}{2(X_1 + X_2)} \times \\ &\{ (\frac{X_2}{X_1} - \frac{X_1}{X_2}) \frac{-P_{C0}}{S_{1-2}} + 2\sin(\delta_{1-2})[1 + \sqrt{1 - \left(\frac{-P_{C0}}{S_{1-2}}\right)^2}] \} \end{split} \tag{4.27}$$

and the denominator is from (4.5).

#### 4.3.3 Limit Cycles

Figure 4.4 displays an inner region bounded by a separatrix (line of A and B). A trajectory inside the separatrix, such as from a point E, closes upon itself indicating that the periodic oscillation is undamped (limit cycles) and never converges to the focal point. Within the separatrix, the system is stable.

#### 4.3.4 Unstable Operating Region

After a severe fault, the system can take  $(\delta_{1-2}, \omega_{1-2})$  to a point such as C outside the separatrix. The trajectory C to D is unbounded and strays away from the focus within the separatrix. The objective of the phase-plane diagram is to discover if the wind farm has unexpected instability. Simulations show that with the fast circuit breakers, which can clear a 3-phase to line-to-ground fault within 100 ms, the post-fault states  $(\delta_{1-2}, \omega_{1-2})$  lie within the separatrix so that synchronism is never lost.

#### 4.4 CONCEPT OF NONLINEAR DAMPING

# 4.4.1 Damping by Modulating Active Power

Damping can be produced by introducing a modulated active power term which is proportional to the frequency  $\omega_{1-2}$ . The frequency  $\omega_{1-2}$  can be measured by a phase-lock loop (PLL) and applied to modulate the active power control of the

wind farm using a gain  $K_P$  (dimensionless). From the example of Figure 4.4, one substitutes  $P_C=-(P_{C0}+K_P\omega_{1-2})$  while keeping  $Q_C=0$  (in situations requiring voltage support  $Q_C=Q_{C0}$ ) in (4.25). To bring out the damping coefficient explicitly, one makes the approximation  $\sqrt{1+x}\approx 1+0.5x$  (valid when x<<1.0). Then, one makes a second approximation:  $(1+y)^2\approx(1+2y)$  (valid when y<<1.0). These approximations are made only to bring out the rotation of the gradients in the phase-plane to explain how damping is realized, and they are not the same as the linearization technique of [65, 85].

Numerator of (4.25) has an additional term to Num of (4.27) which is:

$$\begin{split} Numdamp &= \frac{V^2}{2(X_1 + X_2)} \{ (\frac{X_2}{X_1} - \frac{X_1}{X_2}) \frac{(-K_p \omega_{1-2})}{S_{1-2}} \\ &- 2\sin(\delta_{1-2}) [\frac{\left| P_{C0} \middle| K_p \omega_{1-2} \right|}{S_{1-2}^2}] \} \end{split} \tag{4.28}$$

Therefore (4.24) becomes

$$\frac{d\omega_{_{1-2}}}{d\delta_{_{1-2}}} = \frac{Num}{Denominator} + \frac{Numdamp}{Denominator} \tag{4.29}$$

Because  $\omega_{1-2}$  in Numdamp and in Denominator cancel each other, Numdamp/Denominator in (4.29) is independent of  $\omega_{1-2}$ . This second term Numdamp/Denominator, evaluated at operating angle  $\delta_{1-2,0}$ , is defined as the closed-form formula of damping factor from active power modulation,  $\sigma_{\rm p}$  in (4.30).

$$\begin{split} &\sigma_{_{P}} = \frac{Numdamp}{Denominator} \\ &= \frac{\omega_{_{0}}V^{2}}{4H(X_{_{1}} + X_{_{2}})} \{ -(\frac{X_{_{2}}}{X_{_{1}}} - \frac{X_{_{1}}}{X_{_{2}}}) \frac{K_{_{P}}}{S_{_{1-2}}} - 2\sin(\delta_{_{1-2,0}}) [\frac{|P_{_{C0}}|K_{_{P}}}{S_{_{1-2}}}] \} \end{split} \tag{4.30}$$

Using the slopes of Figure 4.4 as the reference, Numdamp/Denominator of (4.29) can be regarded as the term which rotates the slopes to those of Figure 4.5. As time increases, trajectories follow the new slopes, which veer to the right. Thus a trajectory from A converges to the equilibrium at B.

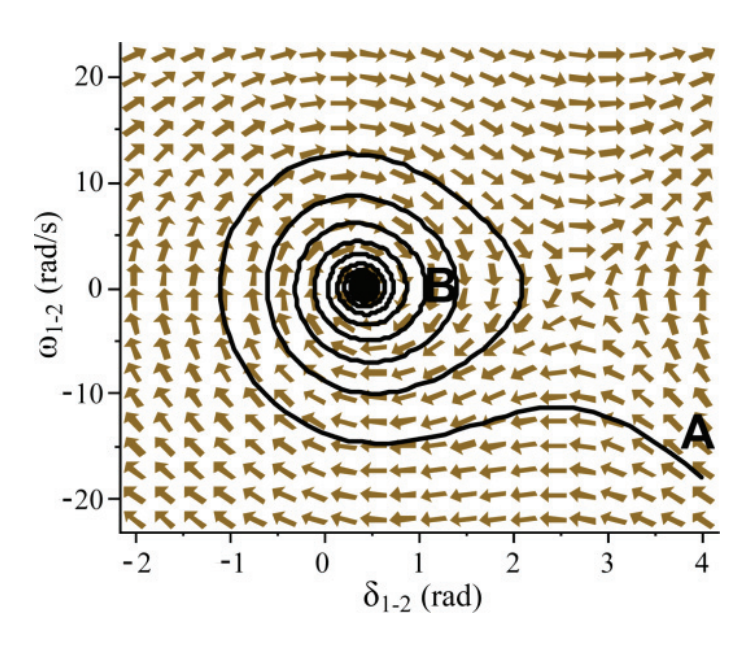


**Figure 4.5** Phase-plane: damping by  $\Delta P_C = K_P \omega_{1-2}$ ,  $K_P = 10$ 

# 4.4.2 Damping by Modulating Reactive Power

Damping by reactive power modulation, using a gain  $K_Q$  (dimensionless), is analysed by using the same technique as in the previous section. By substituting  $P_C=(-P_{C0})$  and  $Q_C=-(K_Q\omega_{1-2})$  in (4.25), the closed-form formula of damping factor due to reactive power modulation is derived and defined as:

$$\begin{split} \sigma_{\scriptscriptstyle Q} &= \frac{Numdamp}{Deno\min ator} \\ &= -\frac{\omega_{\scriptscriptstyle 0} V^2}{4H(X_{\scriptscriptstyle 1} + X_{\scriptscriptstyle 2})} \{\sin(\delta_{\scriptscriptstyle 1-2,0})[\frac{K_{\scriptscriptstyle Q}}{S_{\scriptscriptstyle 1-2}}]\} \end{split} \tag{4.31}$$

#### 4.5 DEPENDENCE ON LOCATION IN TRANSMISSION LINE

## 4.5.1 Dependence of Damping on "r"

The position "r" (0< r < 1.0), enters (4.22), (4.30) and (4.31) as  $X_1=(X_T+rX_L)$  and  $X_2=(X_T+X_L-rX_L)$ .  $\sigma_P$  of (4.30) and  $\sigma_Q$  of (4.31) are dependent on  $X_1$  and  $X_2$  explicitly and on  $S_{1-2}$  (see (4.14)) in the denominators of both equations. The characteristics of  $\sigma_P$  and  $\sigma_Q$  can be understood from the location factors, illustrated by Figure 4.6-(a) and Figure 4.6-(b).

#### 4.5.1.1 Location Factor $1/S_{1-2}$ :

From (4.14)  $S_{1-2}$  is a term similar to reactive power because when  $\cos(\delta_1 - \delta_2) \approx 1.0$ , equation (4.14) becomes

$$S_{1-2} \approx \frac{1}{2} \left( \frac{V^2}{X_1} + \frac{V^2}{X_2} \right) \tag{4.32}$$

Figure 4.6-(a) shows the dependence of  $1\,/\,S_{_{1\!-\!2}}$  on "r".

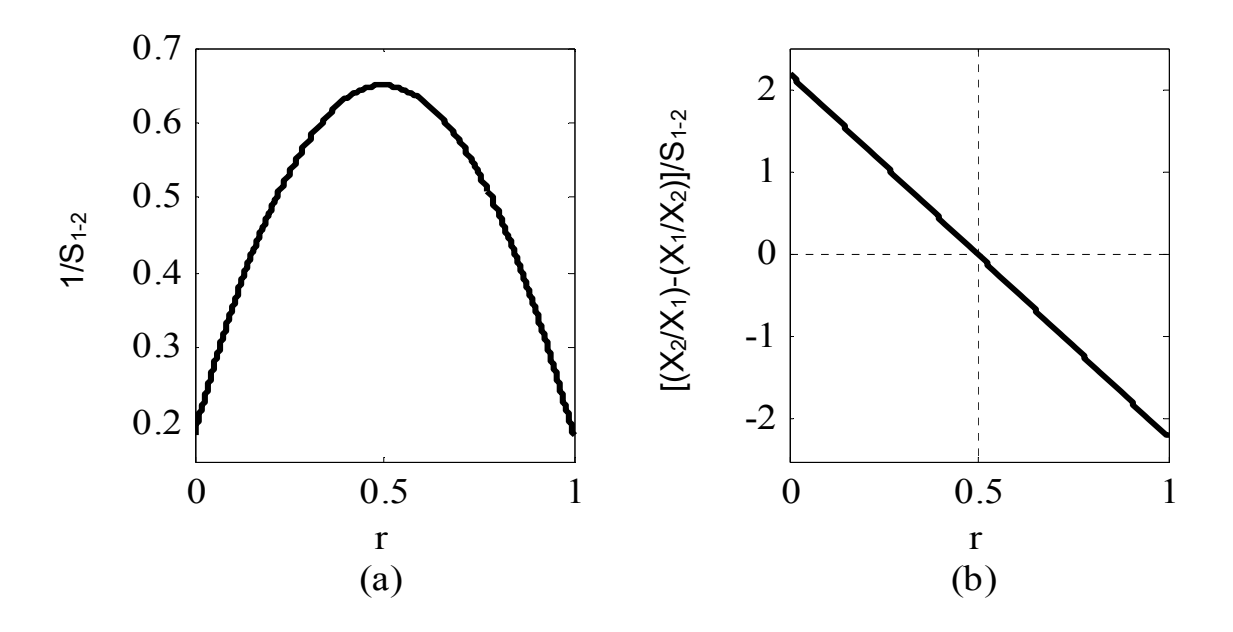


**Figure 4.6** Location Factors (a)  $1/S_{1-2}$ , (b)  $[(X_2/X_1)-(X_1/X_2)]/S_{1-2}$ 

#### 4.5.1.2 Location Factor $[(X_2/X_1)-(X_1/X_2)]/S_{1-2}$ :

 $\sigma_{p}$  of (4.30) is heavily dependent on  $[(X_{2}/X_{1})-(X_{1}/X_{2})]/S_{1-2}$ . Its location factor is displayed in Figure 4.6-(b). The location factors explain how the shapes of  $-\sigma_{p}$  and  $-\sigma_{Q}$  are dependent on "r".

# 4.5.2 Active Power Modulation

In this sub-section,  $P_C=-(P_{C0}+K_P \omega_{1-2})$  and  $Q_C=0.0$ ,  $|K_P|=20$ . Figure 4.7 displays  $-\sigma_P$  plotted as a function of "r". From Figure 4.7, it is apparent that the location factor of Figure 4.6-(b) dominates. This term is the first term on the right-hand side of (4.30). Although the location factor in Figure 4.6-(b) is negative for r> 0.5,  $-\sigma_P$ > 0.0 because the PLL in the wind farm measures  $\omega_{1-2}$  as

a negative value.

#### 4.5.2.1 Dependence on $P_1$ :

The size of  $P_1$ , the active power transmitted from  $G_1$ , enters as the second term on the right-hand side of (4.30) through  $\sin(\delta_{1-2})$ . This second term is multiplied by  $(1/S_{1-2})^2$  which is a small term because it is the square of the ordinate of Figure 4.6-(a). Its addition has little effect on damping as Figure 4.7 shows.

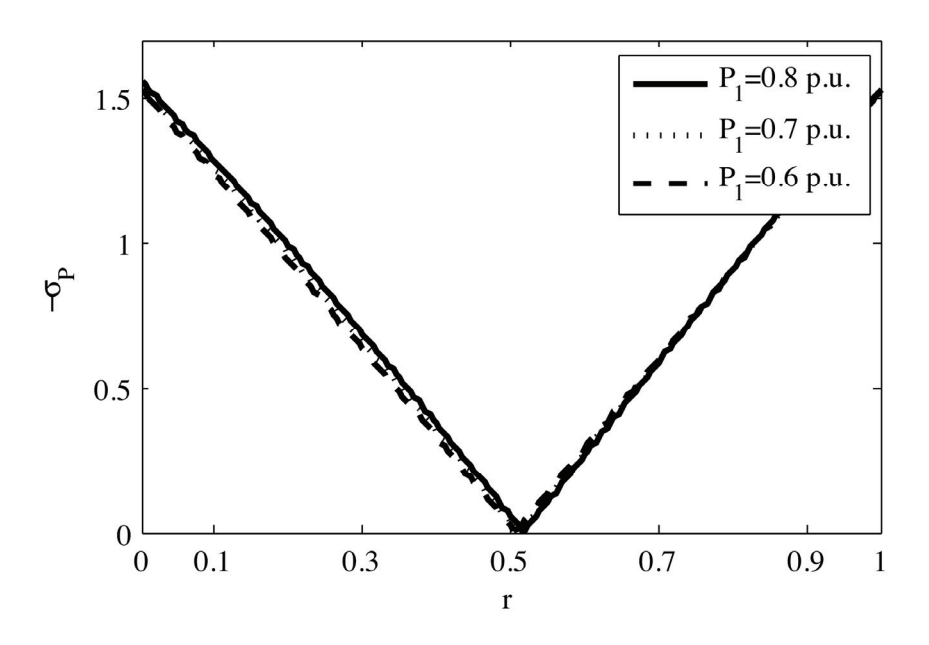


**Figure 4.7** Dependence of  $-\sigma_{P}$  on "r" and  $P_{I}$  ( $P_{C0}$ =-0.2 pu,  $Q_{C0}$ =0.0,  $|K_{P}|$ =20)

#### 4.5.2.2 Dependence on $-P_{C0}$ :

Figure 4.8 shows the influence of  $-P_{C0}$ , the active power of the wind farm. It enters (4.30) as the second term and as already discussed, it is a small term.

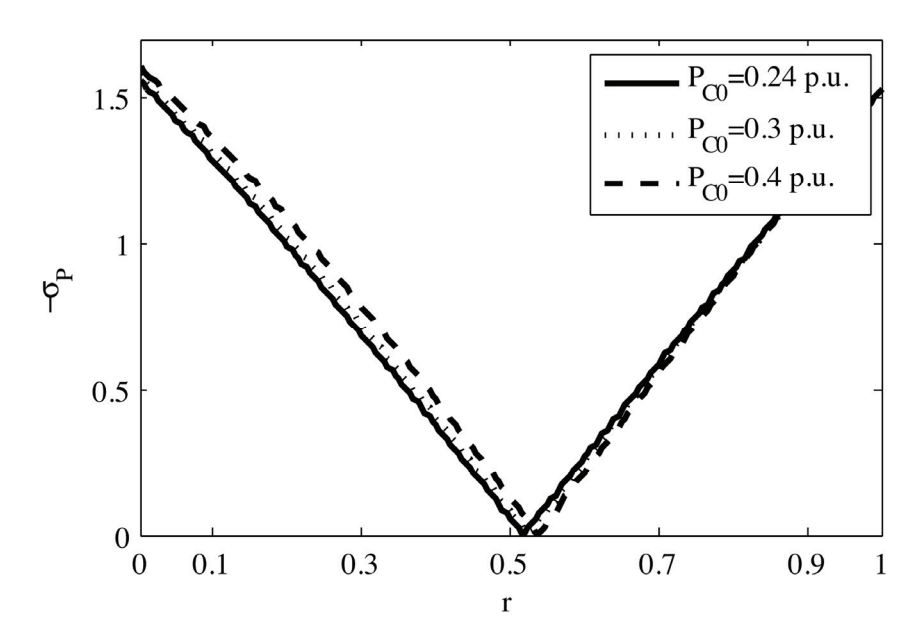


**Figure 4.8** Dependence of  $-\sigma_P$  on "r" and  $P_{C\theta}$  (wind farm). ( $P_I$ =0.8 pu,  $Q_{C\theta}$ =0.0 pu,  $|K_P|$ =20)

# $4.5.3 Reactive\ Power\ Modulation$

Setting  $P_C$ =(- $P_{C0}$ ) and  $Q_C$ =-( $K_Q \omega_{1-2}$ ), the damping  $\sigma_Q$  according to (4.31) is dependent on location factor of (1/ $S_{1-2}$ ) as shown in Figure 4.6-(a).

#### 4.5.3.1 Dependence on $P_1$ :

As shown in Figure 4.9,  $\sigma_Q$  is strongly dependent on  $P_1$  through  $\sin(\delta_{1-2})$ . In (4.31), the  $\sin(\delta_{1-2})$  term is multiplied by  $(1/S_{1-2})$ , whereas in Figure 4.7 it is multiplied by  $(1/S_{1-2})^2$  which is smaller.

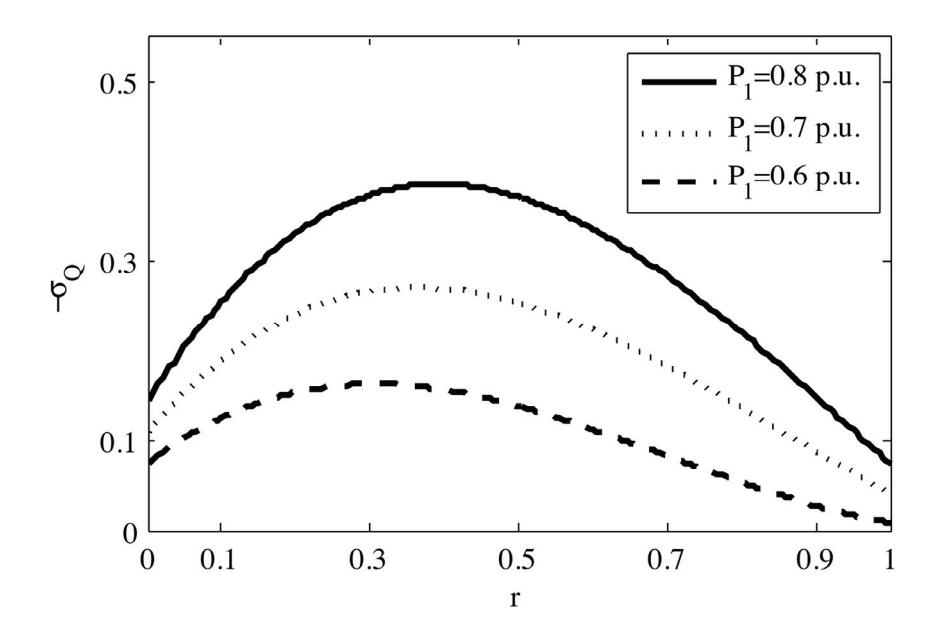
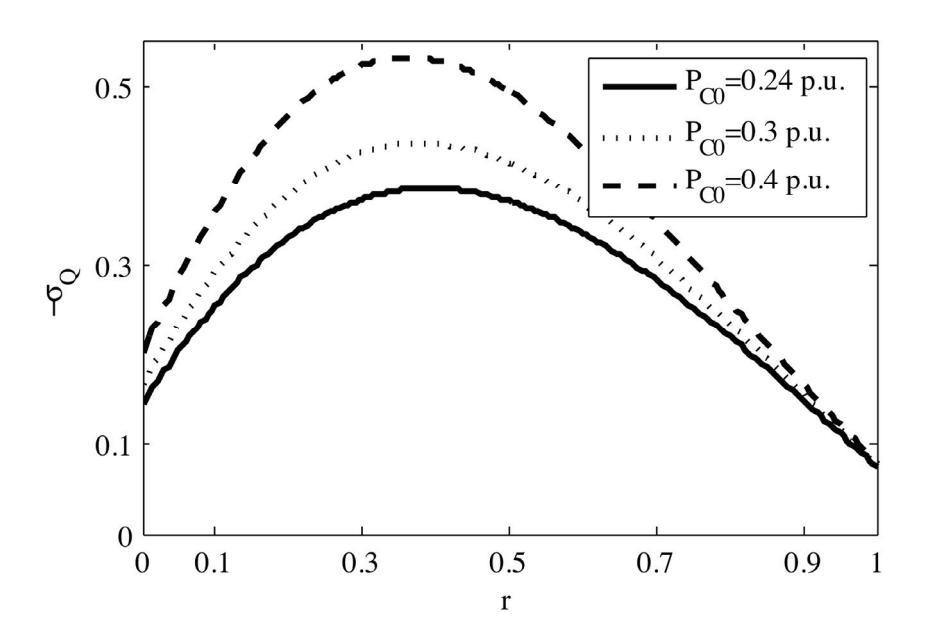


 Figure 4.9  $-\sigma_{_{Q}}$  as a function of "r" and  $P_{_{I}}(P_{_{C0}}\!\!=\!\!0.24$  pu,  $Q_{\!_{C0}}\!\!=\!\!0$  pu,  $K_{_{Q}}\!=\!\!20)$ 



**Figure 4.10**  $-\sigma_Q$  as a function of "r" and  $P_{C\theta}$  (wind farm power), (P1=0.8 pu,  $Q_{C\theta}$ =0 pu,  $K_Q$ =20)

#### 4.5.3.2 Dependence on $-P_{C0}$ :

The injected wind power  $-P_{C0}$  affects  $\sin(\delta_{1-2})$ . From (4.31),  $-\sigma_Q$  is dependent on  $\sin(\delta_{1-2})$ . Thus in Figure 4.10, there are 3 distinct curves of  $-\sigma_Q$ , one for each value of  $-P_{C0}$ . Comparing Figure Figure 4.7 and Figure 4.8 with Figure Figure 4.9 and Figure 4.10 (the same modulation gain  $K_P=K_Q$  have been used), the damping from reactive power modulation is lower than from active power modulation by a factor of about 1/3.

#### 4.5.3.3 Validation of Predictions

The graphs of Figure 4.7 to Figure 4.10 are in agreement with those in [65], which have already been validated by simulations using EMTDC-PSCAD, a commercial grade software.

#### 4.6 CONCLUSION

A synchronous generator swinging against an infinite bus is the model whose close form formulation is used to illustrate many properties of a power system. This chapter has presented Figure 4.3 as potentially usefully model which has (4.22) as a close form formulation. This model can have many applications. For instance, the load can be a positive complex power to model a large city.

In this chapter, the model has been applied to study the damping available from a sustainable energy technology (specifically wind energy).

The research gives an analytical explanation for the difference in effectiveness of damping by active and reactive power modulation based on the location factors, illustrated in Figure 4.6.

# CHAPTER 5

# NONLINEAR DAMPING OF NONLINEAR OSCILLATIONS BY RENEWABLE TECHNOLOGIES

#### 5.1 Introduction

Although the sustainable energy technology of chapter 4 has active and/or reactive power to help damp electromechanical oscillations in the power system, the amount of damping is limited by the MVA rating of the installation, irrespective of the active power feedback gain  $K_p$  and the reactive power feedback gain  $K_Q$ . Normally, "saturation blocks" are placed in the signal paths to prevent the MVA rating from being exceeded. The "saturation blocks" represent one form of nonlinearity. The other nonlinearity lies in the  $sin\delta$  term in (4.22) in chapter 4. Small perturbation linearization can get past the  $sin\delta$  nonlinearity but not the "saturation blocks".

In practice, when one uses low feedback gains to remain in the linear region, the damping is feeble. When high gains are used to obtain better damping, most of the operation lies in the saturated region. There is a need to know how the high damping is achieved during saturation.

In applying phase-plane diagrams to understand the damping process, the conclusion is quickly reached that nonlinear damping is more effective.

The research uncovers an interesting conclusion: (i) Nonlinear feedback damps linearly with time. (ii) Linear feedback damps exponentially with time (linearly with distance).

An explanation for the different damping rates is given using Energy functions. It should be stated that because (4.22) is complicated, an approximation to that

equation is used to define an energy function. The Energy functions used are related to the energy of simpler dynamic linear and nonlinear systems. Although lacking in mathematical rigour, the "proofs" reveal the physical mechanism of damping. In nonlinear damping, the rate of energy dissipation is proportional to power. In linear damping, the energy is dissipated as work.

This chapter is organized as follows:

Section 5.2 describes how the feedback gain,  $K_P$  (or  $K_Q$ ), interacts with the saturation limit in the phase-plane and why nonlinear damping is preferred to linear damping. It develops a theory based on Energy functions to explain the difference in their damping rates.

Hitherto, results have been obtained by using MATLAB to simulate(4.22). In order to strengthen the proof of principle, further simulations have been performed with HYPERSIM in Section 5.4.

Hitherto, high damping has been pursued without regard to operational constraints of the specific sustainable energy technology. Section 5.5 reviews what may be the reservations of wind turbine manufacturers and wind farm owners.

#### 5.2 Damping by A Mix of Linear and Nonlinear

#### **FEEDBACK**

#### 5.2.1 MVA Rating Constraints on Linear Control

The gain  $K_P$  in linear feedback of active power modulation is constrained by  $|S_{rating}|$ , the MVA rating of the renewable technology installation. As  $Q_{CO}=0.0$  in this study, the active power allowed is:

$$(-P_{C0} - K_P \omega_{1-2})^2 \le S_{rating}^{2} \tag{5.1}$$

Assuming that on clearing a fault, the permitted line frequency deviation is  $\omega_{I-2f}$ , the size of the linear gain is limited to

$$K_{P} = \frac{\left(\left|S_{rating}\right| - \left| -P_{C0}\right|\right)}{\omega_{1-2f}} \tag{5.2}$$

For reactive power modulation,

$$(-P_{C0})^2 + (-K_{Q}\omega_{1-2})^2 \le S_{rating}^{2}$$
 (5.3)

$$K_{Q} = \frac{\sqrt{S_{rating}^{2} - P_{C0}^{2}}}{\omega_{1-2f}}$$
 (5.4)

Simulations show that damping, under exclusive linear control, is weak because  $K_P$  and  $K_Q$  are not high enough because of the MVA rating constraint.

#### 5.2.2 Linear Control with "Saturation Blocks"

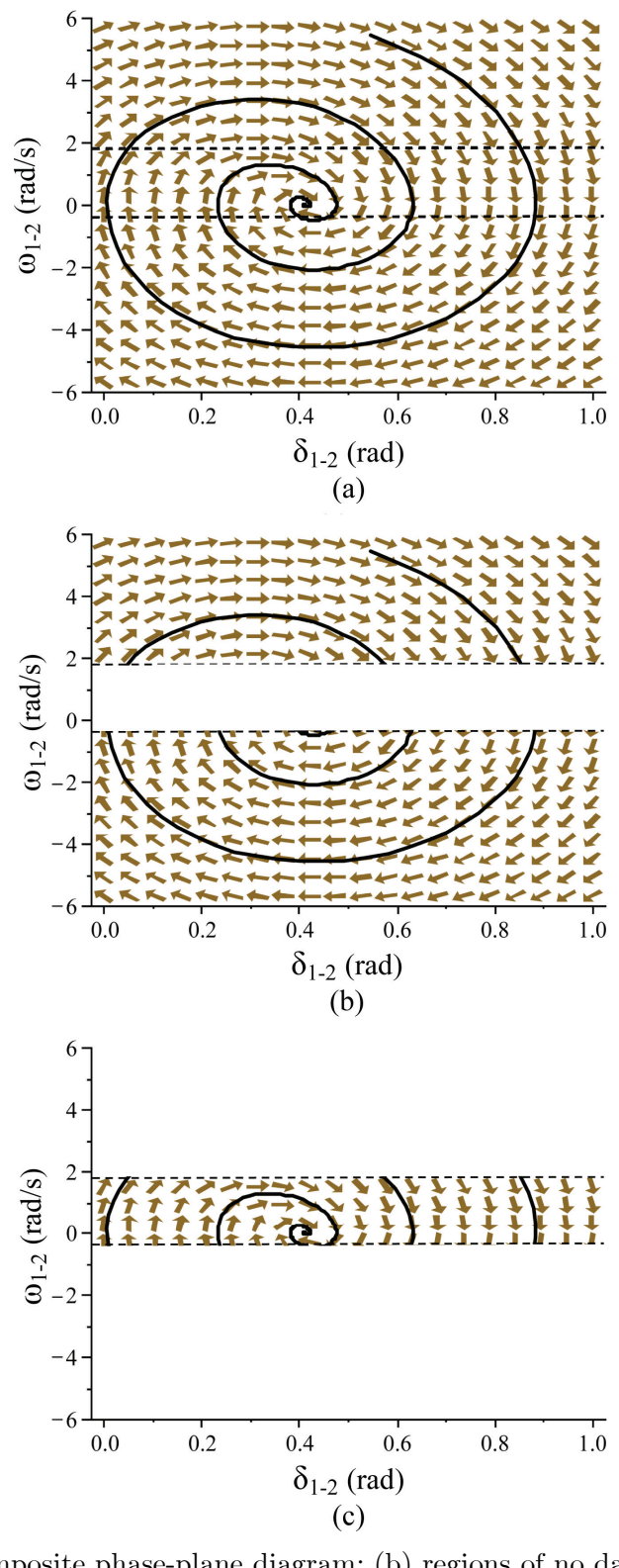
In control design which uses a high  $K_p$  gain, "saturation blocks" are placed in the signal paths to prevent the MVA rating from being exceeded. From (5.2), it follows that the excursion of  $\omega_{l-2}$  in the linear feedback range is very limited.

Figure 5.1 is the phase-plane picture for active power modulation when  $K_P=50$ . Linear feedback isrestricted to active power within the limits:  $P_{\it C,lower} < |\text{-}P_{\it C}| < P_{\it C,upper}$  . Figure 5.1 (a) consists of three regions: Figure 5.1 (b) shows the upper region  $|\text{-}P_{\it C}\>| > P_{\it C,upper}\>$  and the lower region and  $|\text{-}P_{\it C}\>| < P_{\it C,lower}\>$  . The equivalent frequency dependent damping gain in the regions are  $K_P = P_{C,upper}/|\omega_{1-2}|$  and  $K_P = P_{Clower}/|\omega_{1-2}|$ . The equivalent damping gain becomes lower for larger  $|\omega_{1-2}|$ .

Linear operation is restricted to the thin slice  $(K_P \text{ is large})$  of Figure 5.1(c). When the trajectory crosses the region of (c), although  $K_P$  is high,  $\omega_{I-2}$  is small and the amount of  $K_P\omega_{I-2}$  to rotate the gradients is small.

#### 5.3 Bang-bang Nonlinear Damping

This section investigates on the damping which is produced by setting the gain  $K_P$  or  $K_Q$  to be very large so that the slice of Figure 5.1(c) becomes infinitesimally thin. Therefore, damping comes almost entirely from the nonlinear regions of Figure 5.1(b). The injection of  $\Delta P_C$  (or  $\Delta Q_C$ ) is to its maximum limit  $\Delta P_{C,LIMIT}$  (or  $\Delta Q_{C,LIMIT}$ ):



**Figure 5.1\_**(a) composite phase-plane diagram; (b) regions of no damping; (c) region of heavy damping.

$$\Delta P_{C} = -\frac{\omega_{1-2}}{\left|\omega_{1-2}\right|} \Delta P_{C,LIMIT} \tag{5.5}$$

or

$$\Delta Q_C = -\frac{\omega_{1-2}}{|\omega_{1-2}|} \Delta Q_{C,LIMIT} \tag{5.6}$$

In order to develop a theory of nonlinear damping, the equations in (5.7) and later in (5.12) have been used as approximations to (4.22).  $P_{\Sigma}$ ,  $P_{\Lambda}$  and  $P_{\rho}$  are used to represent clusters of symbols in (4.22). In particular, the equation for  $Q_{C}=0$  and  $P_{C}=P_{C\theta}$  is of the form:

$$\frac{2H}{\omega_{_{0}}}\frac{d\omega_{_{1-2}}}{dt} = P_{_{\Sigma}} - P_{_{\Lambda}}\sin(\delta_{_{1-2}}) \tag{5.7}$$

#### 5.3.1 Limit Cycles

Multiplying (5.7) by  $\omega_{1-2}$ , and substituting  $d\delta_{1-2}/dt = \omega_{1-2}$ , one has

$$\frac{2H}{\omega_{0}}\omega_{1-2}\frac{d\omega_{1-2}}{dt} = P_{\Sigma}\frac{d\delta_{1-2}}{dt} - P_{\Lambda}\sin(\delta_{1-2})\frac{d\delta_{1-2}}{dt}$$
 (5.8)

On integration with respect to time from  $t_0$  to t, one has

$$\begin{split} &\{\frac{H}{\omega_{0}}[\omega_{1-2}(t)]^{2}-P_{\Sigma}\delta_{1-2}(t)-P_{\Lambda}\cos\delta_{1-2}(t)\}\\ &=\{\frac{H}{\omega_{0}}[\omega_{1-2}(t_{0})]^{2}-P_{\Sigma}\delta_{1-2}(t_{0})-P_{\Lambda}\cos\delta_{1-2}(t_{0})\} \end{split} \tag{5.9}$$

Defining an energy function E(t)

$$E(t) = \{ \frac{H}{\omega_0} [\omega_{1-2}(t)]^2 - P_{\Sigma} \delta_{1-2}(t) - P_{\Lambda} \cos \delta_{1-2}(t) \}$$
 (5.10)

Equation (5.9) becomes on substituting (5.10):

$$E(t) = E(t_0) \tag{5.11}$$

From (5.11), one sees that the limit cycles of Figure 4.4 represent conservation of energy (involving exchanges of kinetic and magnetic energy). The limit cycles never converge to the equilibrium point because there is no "mechanism" to reduce the initial energy storage,  $E(t_0)$ .

#### 5.3.2 Nonlinear Damping of Limit Cycles

Linear damping is produced by introducing a power term  $K_p\omega_{l-2}$  so that  $P_C=P_{C0}+K_p\omega_{l-2}$ . Equation (5.7), which is derived from (4.6), is basically a "torque" balance equation, except that power engineers prefer to use power terms by multiplying "torques" by  $\omega_0$ . The linear damping power  $K_p\omega_{l-2}$ , as a "torque" has to be divided by  $\omega_{l-2}$ . Using  $P_\rho$  as a cluster coefficient, the damping power  $K_p\omega_{l-2}$  becomes a "damping torque" so that (5.7) is modified as:

$$\frac{2H}{\omega_{0}}\frac{d\omega_{1-2}}{dt} = P_{\Sigma} - P_{\Lambda}\sin(\delta_{1-2}) - P_{\rho}K_{p}$$
(5.12)

In implementing Nonlinear Damping,  $P_C = P_{C0} + \Delta P_C$ .  $\Delta P_C$  has to be divided by  $\omega_1$  also. Equation (5.12) becomes

$$\frac{2H}{\omega_0} \frac{d\omega_{1-2}}{dt} = P_{\Sigma} - P_{\Lambda} \sin(\delta_{1-2}) - P_{\rho} \frac{\Delta P_C}{\omega_{1-2}}$$

$$(5.13)$$

On integrating (5.13) with respect to time by retracing the steps of (5.8)to (5.11), one has

$$E(t_{f}) = E(t_{0}) - P_{o}\Delta P_{C}(t_{f} - t_{0})$$
(5.14)

From (5.14), the initial energy  $E(t_0)$  is linearly depleted to  $E(t_f)=0$  by a constant power drain,  $P_{\rho}\Delta P_{C}$ , in the time span

$$t_{f} - t_{0} = \frac{E(t_{0})}{P_{\rho} \Delta P_{C}} \tag{5.15}$$

#### 5.3.3 Validation of Nonlinear Damping Theory

The results in Figure 5.2, which are obtained by numerical integration of (4.5) and (4.22), validate the theory. The real power setting is  $P_C = -(P_{C0} + \Delta P_C)$ . Only the full oscillation of  $\omega_{I-2}$  for  $\Delta P_C = 20$  MW is displayed. A straight line envelope passes over the peaks, showing agreement with (5.14). For clarity, only the envelopes for  $\Delta P_C = 40$  MW, 60MW and 80MW are shown.

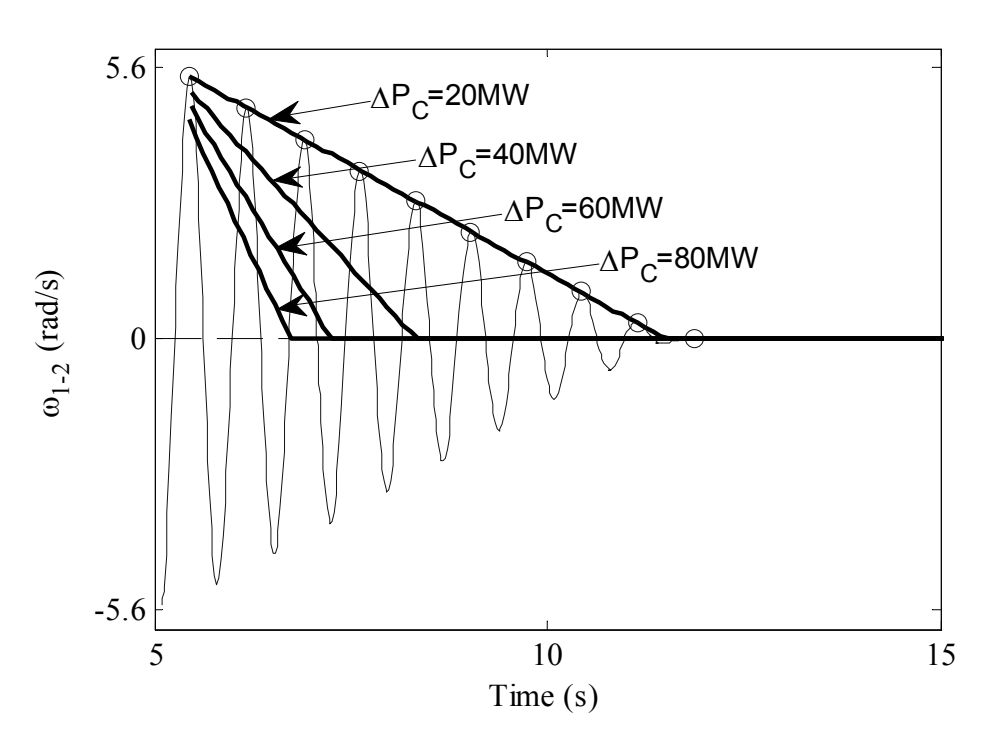


**Figure 5.2** Oscillation of  $\omega_{I-2}$  under Nonlinear Damping by Active Power:  $\Delta P_{\rm C} = 20, 40,$  60, and 80MW

Figure 5.3 is similar to Figure 5.2 except that it presents the results of nonlinear reactive damping. In Figure 5.2 and Figure 5.3, the intersections of the straight line envelopes and the time axis yield the final times  $t_f$  of the transients. Figure 5.4 shows that  $1/(t_f t_0)$  is linearly proportional to  $\Delta P_C$  and  $\Delta Q_C$  validating the formula derived in (5.15). The inverse time relation corresponds to the everyday notion that the larger the power drain, the faster the time for a fixed store of energy to be depleted. Damping by  $\Delta P_C$  is more effective than by  $\Delta Q_C$ .

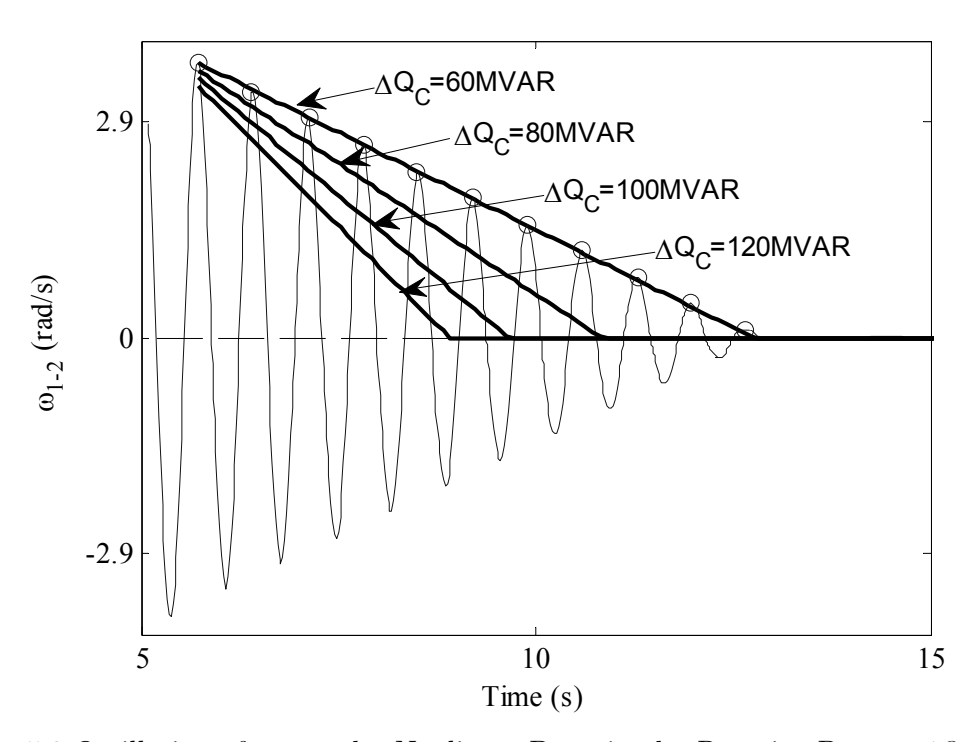


**Figure 5.3** Oscillation of  $\omega_{1-2}$  under Nonlinear Damping by Reactive Power  $\Delta Q_c = 60$ , 80, 100, 120 MVAR

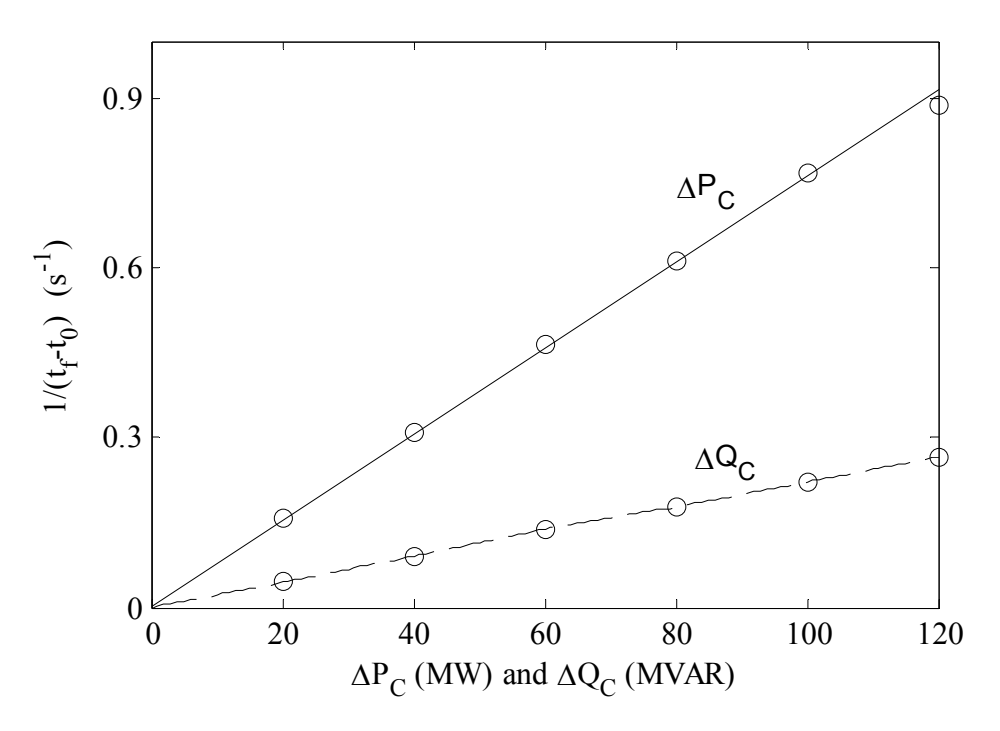


**Figure 5.4** Inverse damping time-vs- $\Delta P_C$  or  $\Delta Q_C$ 

## 5.3.4 Comparison with Linear Damping

For exclusive linear damping, the starting point of analysis is (5.12). Multiplying (5.12) by  $\omega_{l-2}$  and on integration with respect to time, one has an expression similar to (5.14),

$$E(t) = E(t_0) - P_{\rho} K_{P}(\delta_{f} - \delta_{0})$$
 (5.16)

except that depletion of the energy is by the work done by the "torque",  $P_{\rho}K_{P}$ , in traversing an angular distance  $\delta'_{1-2}$ , which is obtained from integrating:

$$\frac{d\delta'_{1-2}}{dt} = \left|\omega_{1-2}\right| \tag{5.17}$$

The angular distance  $\delta'_{1-2}$  is a monotonically increasing function of time, like the length of a thread wound around a spool.

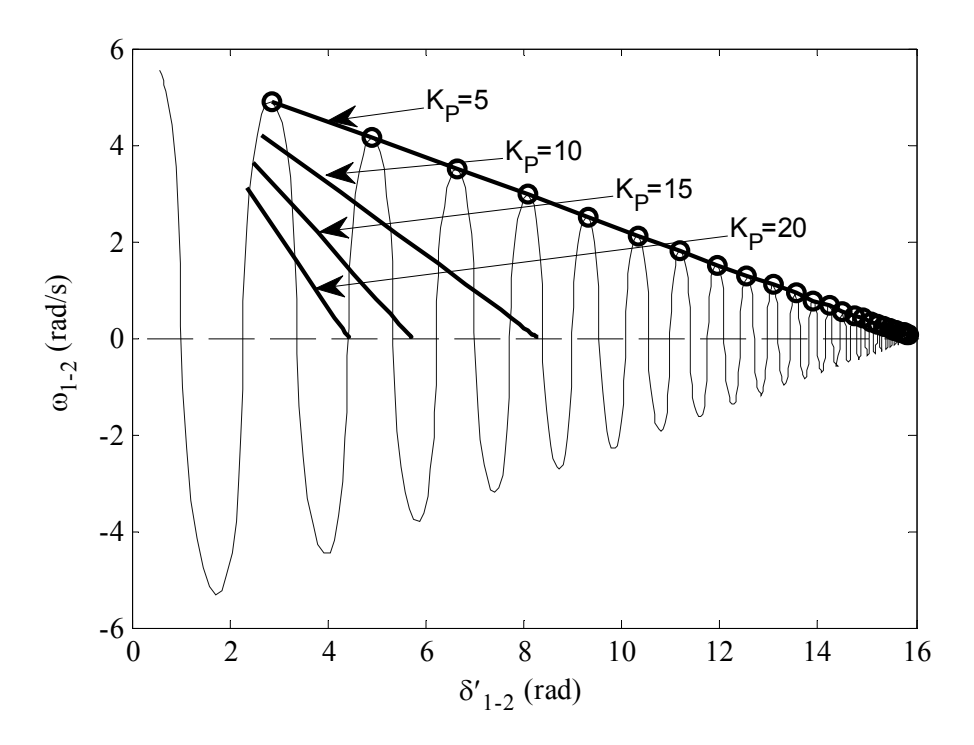


**Figure 5.5**  $\omega_{1-2}$ -vs- $\delta'_{1-2}$  the angular distance, under Linear Gain,  $K_P = 20, 40, 60, \text{ and } 80.$ 

In order to demonstrate the correctness of (5.16), the simulated  $\omega_{I-2}$  is plotted as a function  $\delta'_{I-2}$  in Figure 5.5. The peaks of  $\omega_{I-2}$  (for  $K_P=5$ ) fit a straight line. Only the straight line envelopes for  $K_P=10$ , 15 and 20 are displayed. Figure 5.5 is similar to Figure 5.2 except that the x-axis is not time but the angular distance  $\delta'_{I-2}$ .

The exponential decay with time is evident in the crowding of the oscillations close to the terminal distance  $\delta'_{1-2f}$ . Depending on Nonlinear or Linear Damping, the same amount initial energy  $E(t_0)$  is depleted linearly by one of the two mechanisms:

$$P_{\rho}\Delta P_{C}(t_{f}-t_{0}) = P_{\rho}K_{P}(\delta'_{1-2,f}-\delta'_{1-2,0})$$
 (5.18)

## 5.4 FURTHER PROOF OF PRINCIPLE BY SIMULATION

The simulation proof of principle in [65] made use of detail model of power electronic converters but very simplified models of generators, transformers and transmission lines were used. This section presents further proof by using Hypersim, a commercial grade simulation system of TransEnergie (Hydro-Quebec). The objective is to represent Figure 4.3 with detail models of generators, transformers and transmission line (see Appendix B), which are generally accepted by industry. The amortisseur windings and power system stabilizers (PSS) have been disenabled so as to highlight the damping from the renewable technology. The renewable technology is modeled by the S-modulator(Figure B.1).

## 5.4.1 Test Conditions

Appendix B lists the active power loads and the generator parameters of the tests. Each test consists of evaluating the system damping following the clearing of a 3-phase-to-ground fault at the location shown in Figure 4.3.

## 5.4.2 Tests on Active Power Modulation

The test results of Figure 5.6 and Figure 5.7 confirm the predictions of Figure 4.7 and [65] that damping by active power is excellent at r=0.0 and poor in the "electrical middle" of the transmission line (which is r=0.667 for the post-fault

system of Figure 4.3).

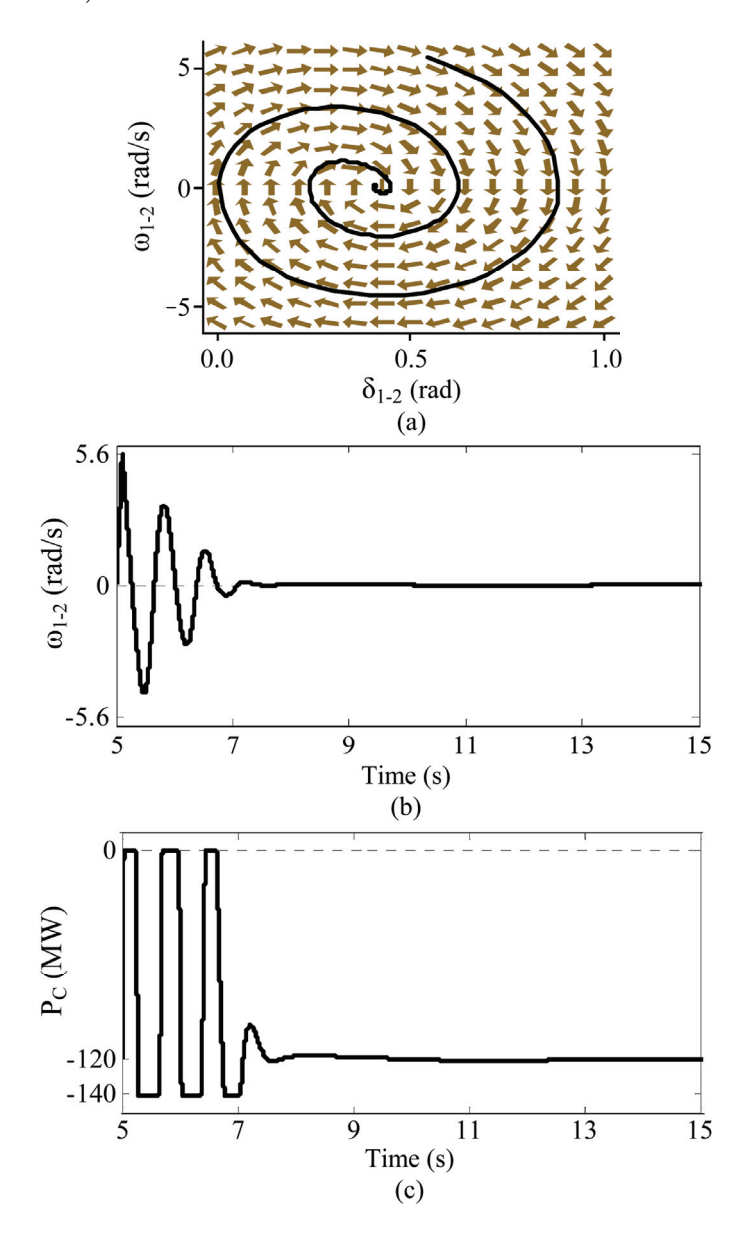


**Figure 5.6** Location r=0.0. Damping from active power modulation (a) phase-plane; (b) frequency deviation; (c) renewable energy active power.

The renewable technology output is  $P_{C0}=120$  MW and  $Q_{C0}=0.0$ . The gain is  $K_P=100$  and the bounds are  $0.0 < |-P_C| < 140$  MW. For such a high gain, the region of Figure 5.6 (c) is very thin and the damping comes almost entirely from

the regions of Figure 5.6(b) for which Nonlinear Damping of Section 5.3 applies. The asymmetrical bounds make use of the full capacity of the renewable technology whose rating is assumed to be  $S_{rating}$ =140 MVA.

#### 5.4.2.1 Renewable technology at End of Transmission Line near to G1

The number of oscillations required for the transient to be damped out is shown in the phase-plane of Figure 5.6(a) (predicted by (4.5) and (4.22)) and it agrees with the number from simulations by HYPERSIM in Figure 5.6(b) and (c). Figure 5.6(c) shows asymmetrical nonlinear injection of active damping power. When the damping power injections are asymmetrical, the average grid frequency can drift from the 60 Hz due to load-generation unbalance as simulations in [81] have shown. The drift is negligible in large systems. In any case, there is the AGC to keep the grid frequency regulated.

#### 5.4.2.2 Renewable technology in "Middle" of Transmission Line

The phase-plane diagram in Figure 5.7 shows that there is very little damping when the renewable technology is situated in the "electrical middle" of the transmission line. The simulations are terminated at t=15s and for this reason, the very lightly damped trajectory appears as a circular band in Figure 5.7. HYPERSIM simulations confirm the results.

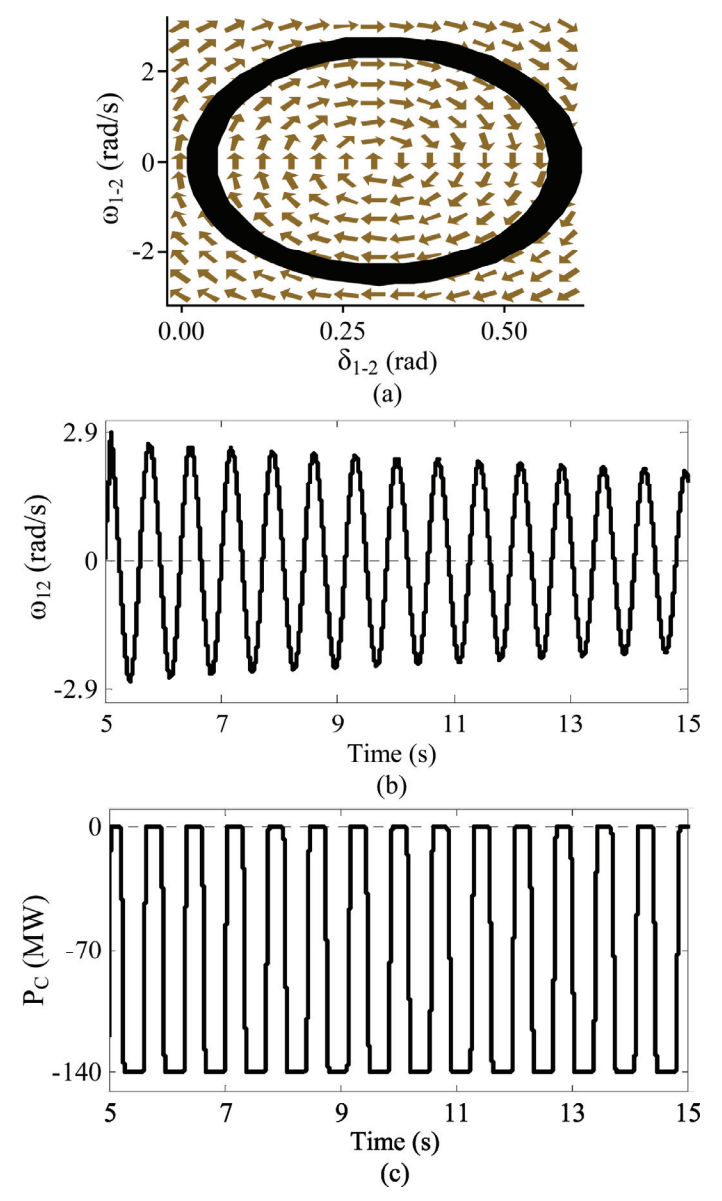
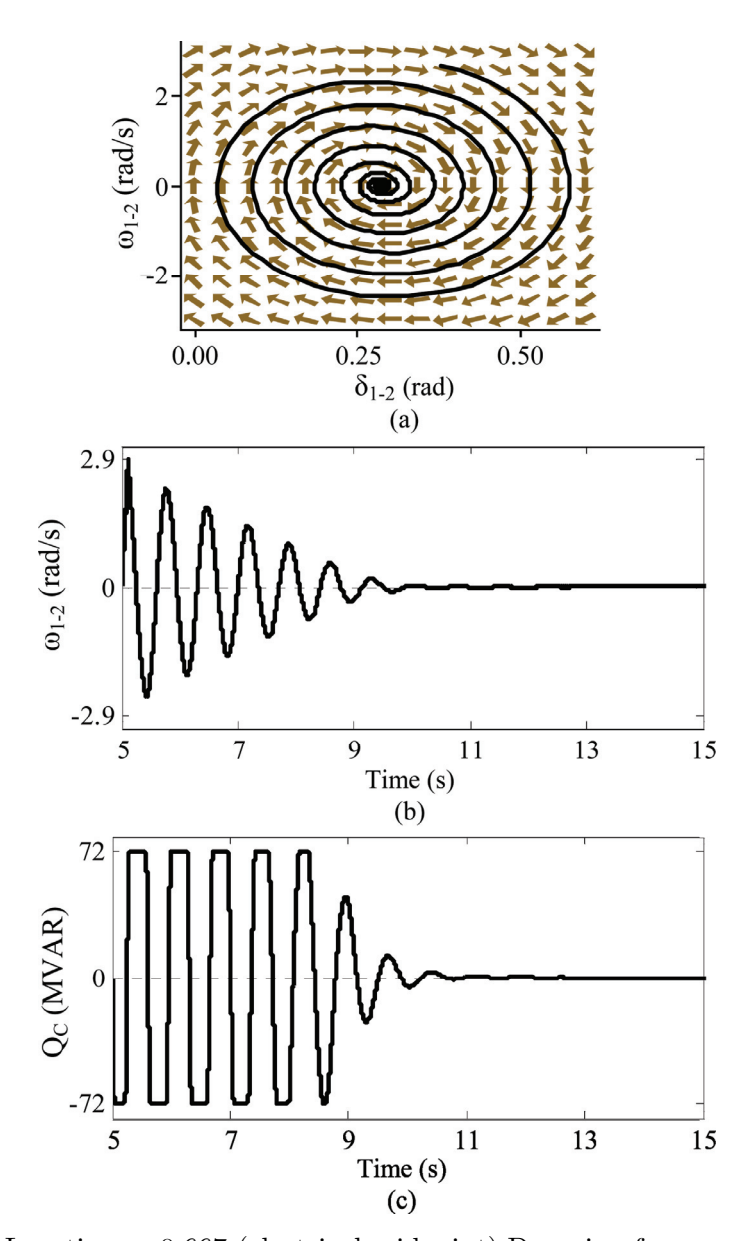


Figure 5.7 Location r=0.667. Damping from active power modulation (a) phase-plane; (b) frequency deviation; (c) wind farm active power.

#### 5.4.2.3 Tests on Reactive Power Modulation in "Middle" of Transmission Line

Figure 5.8 confirms that reactive power modulation can provide good damping in the "electrical middle" of a transmission line.



**Figure 5.8** Location r=0.667 (electrical midpoint). Damping from reactive power modulation(a)phase plane;(b)frequency deviation;(c)renewable technology reactive power.

The gain is  $K_Q$ =100. Although  $P_{C0}$ =120 MW, because of (5.4) and  $S_{rating}$ =140MVA, the reactive power constraint is -72 MVA <  $Q_C$  < 72 MVA. Good agreement in the predictions in Figure 5.8(a) with HYPERSIM simulation in (b) can be seen from the same number of oscillations required to damp the transient.

The peaks of the oscillations in (b) fit a straight line as in Figure 5.3. Saturation of reactive power is shown in (c).

## 5.5 Non-Electrical Engineering Limits

## 5.5.1 Limits from Wind-Turbine Manufacturers

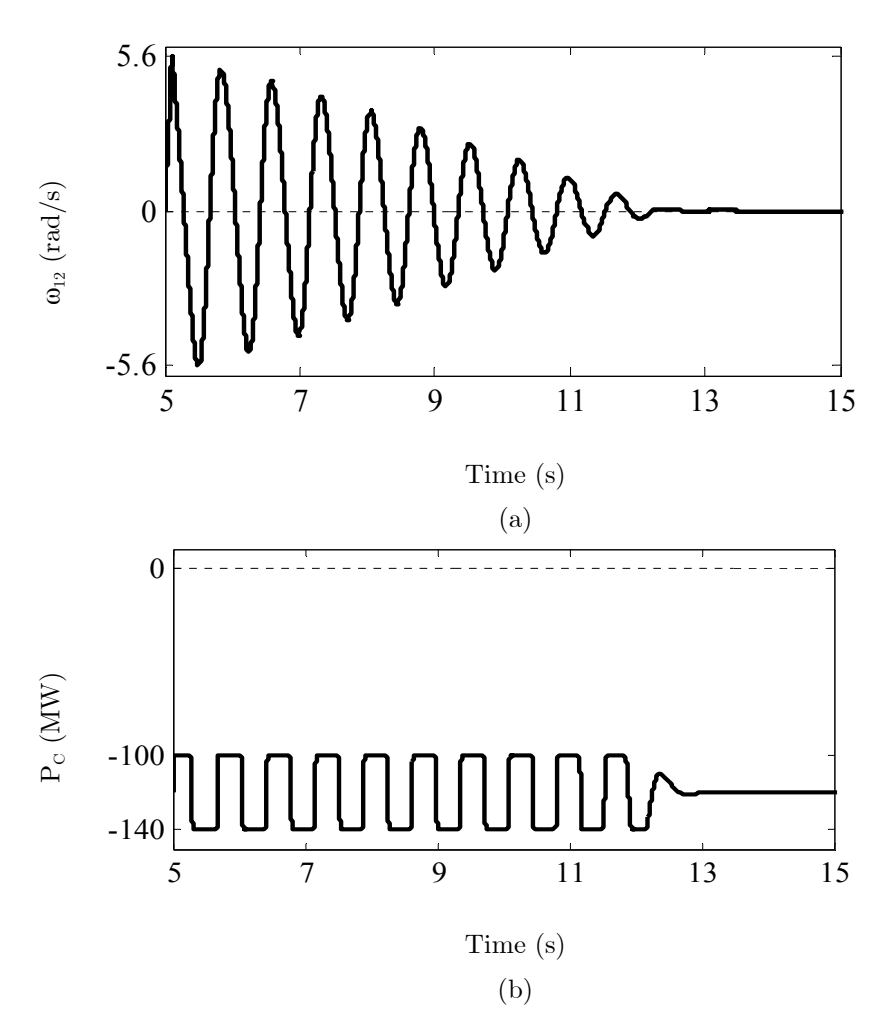


Figure 5.9 Active power modulation. r=0.0,  $K_P = 100$ : (a) frequency deviation; (b) wind farm power.

Up to this point, this chapter has addressed electrical engineering constraints

(MVA limit) only. Wind turbine manufacturers and wind farm operators would have their reservations and would want the active power deviation to be more restricted. Assuming that active power deviation of around 15% is acceptable, the damping achievable is shown in Figure 5.9. The gain is  $K_p=100$ .

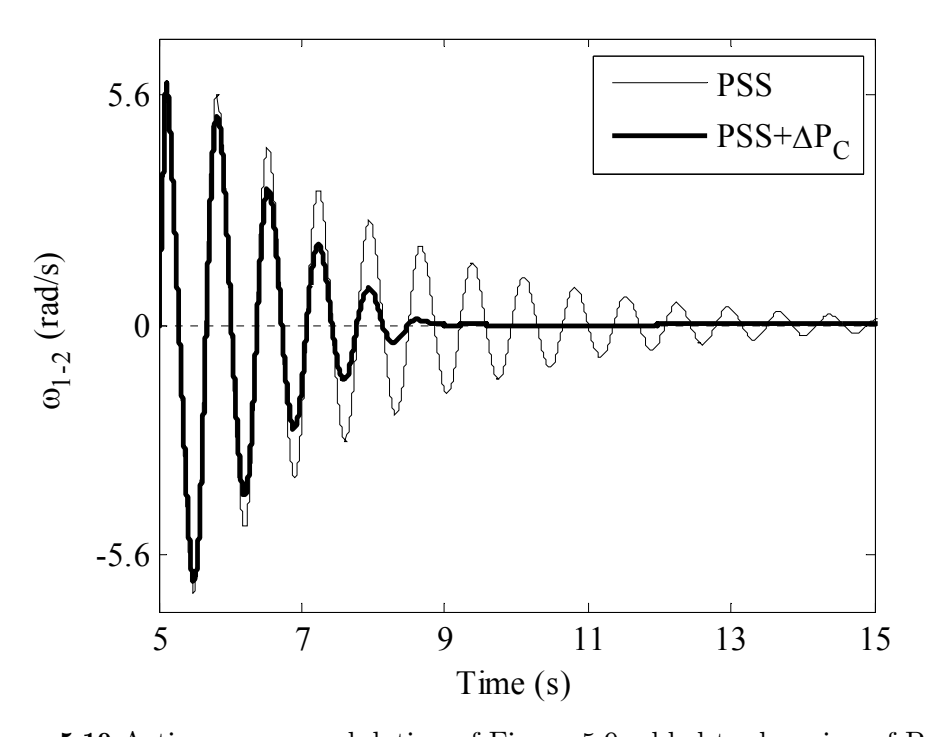


Figure 5.10 Active power modulation of Figure 5.9 added to damping of PSS.

The reduced damping does not have to be disappointing. This is because the damping from the wind farms is required only to augment the system damping. When the power system stabilizers (PSS) of the generators are activated, the simulations in Figure 5.10 show that active power modulation improves the damping.

In the middle of the line, the reactive power modulation of Figure 5.8 improves

the damping by the PSS as Figure 5.11 shows. Unlike active power which impacts on the mechanical system, the large reactive power constraint of -72 MVA < Q  $_{\rm C}<$  72 MVA is not likely to be objectionable to wind farm manufacturers or wind farm owners.

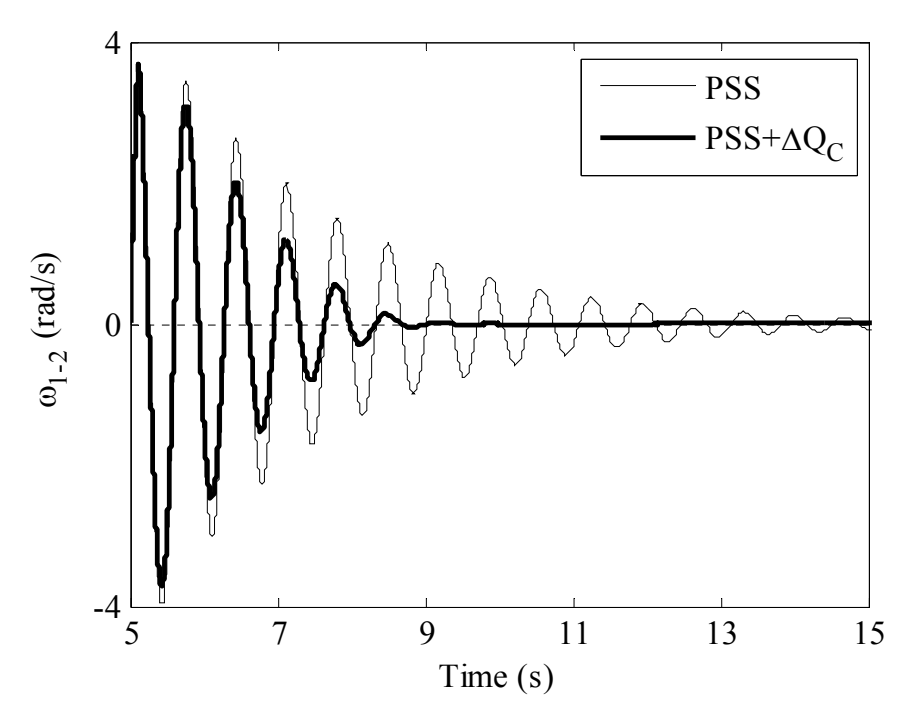


Figure 5.11 Reactive power modulation of Figure 5.8 added to damping of PSS.

## 5.6 CONCLUSIONS

Limit cycles in power systems are due to perpetual exchanges of kinetic energy and magnetic energy whose sum, the total energy, remains constant. Damping from linear feedback can be viewed as depletion of the total energy by work done by an opposing torque (proportional to the feedback gain  $K_p$ ) in the angular

distance  $\delta'_{I-2}$ . When  $K_P$  is constant, the system damps linearly with respect to  $\delta'_{I-2}$ . As damping from bang-bang nonlinear feedback depletes the total energy by a drain of active (or reactive) power, it is time dependent. This is because the time integral of power is energy. When the injected active (or reactive) power is constant, the damping attenuates linearly with time. The research points to the desirability of using a strategy based on using a very high gain  $K_P$  (or  $K_Q$ ) and operating to the limit of the MVA rating of the installation. The high  $K_P$  (or  $K_Q$ ) restricts linear operation to a small region so as to derive high damping from bang-bang nonlinear regions. On convergence near to the equilibrium, the exponential damping of linear feedback is free of "chatter".

CHAPTER 6

# SUMMARY AND CONCLUSION

#### 6.1 Introduction

The research of this thesis has been motivated by the concern that as more power grids continue to interconnect, for example the Trans-Canadian Grid, the electromechanical oscillations of the large interconnection will fall below the bandwidth of existing power system stabilizers (PSS). If the interconnection will be by HVDC, the system will retain the stability of the original small power grids thus avoiding the problem. However HVDC decoupling is expensive. This thesis examines the alternative of stabilization of the all-ac system by the Global PSS concept. The Global PSS makes use of a Central Controller which receives telecommunicated information of key generator stations bearing the GPS timestamped measurements of PMUs. Then from a stabilization algorithm in the Central Controller, and feedback control signals are telecommunicated back to the same key generator stations.

The thesis has proposed the Multiple Modal Selectivity Method of chapter 2 as the stabilization algorithm and presented proof of principles by simulations and eigenvalue evaluations in chapter 3. Noting that control signals must be backed by sufficient active and reactive power, chapter 4 has continued the on-going research on using the complex power of sustainable energy technologies to provide damping. The on-going research work has been based on small signal linearization. The thesis confirms that its conclusions apply also in large signal perturbations. Chapter 5 pursues the question of complex power availability to

greater depth. Given that there is always a MVA rating, the conclusion of chapter 5 is: "bang-bang damping" is the preferred strategy of every sustainable energy installation.

#### 6.2 CONCLUSIONS OF THESIS

From the engineering practice viewpoint, it can be concluded that:

- (i) the Multiple Modal Selectivity Method has the selectivity and robustness to be used in a Global PSS to damp electromechanical modes of a large all-ac power system;
- (ii) active power and reactive power from sustainable energy technologies can contribute to system damping. Active power is more effective when the sustainable energy technology is located at the ends of a transmission line. Reactive power is more effective when the location is in the middle of the line. These conclusions are no longer restricted to the assumptions of small signal linearization.
- (iii) "Bang-bang (nonlinear) damping" is more effective than linear feedback strategy.

From the engineering science viewpoint:

(i) the Multiple Modal Selectivity Method has analytical expressions which prove that in stabilizing the "targeted modes" the non-targeted modes

are never destabilized. In addition, the positive damping is not sensitive to parameter variations (such as: changes in loading, disconnection of a tie-line.)

- (ii) a new archetype model, consisting of a complex power load situated in a transmission line between two generators (Figure 4.3), has been presented with close form formulation of its dynamics (equation 4.22).

  The archetype model is used in the thesis to represent a sustainable energy technology installation. Because of the usefulness of a close form formulation, it will have many other applications in future research.
- (iii) the phase-plane enables damping in the linear and nonlinear regime to be understood. Although restricted to 2-dimensions, the concepts carry to high dimensions.
- (iv) Energy functions (similar to Lyapunov functions) have been used to explain that nonlinear damping attenuates linearly with respect with time, while linear damping attenuates linearly with respect to distance (exponentially with respect to time).

Having presented the conclusions in terse summaries, the paragraphs below outline some of the important features:

#### 6.2.1 Chapter 2

Upper most in mind in conceiving the innovative Multiple Modal Selectivity Method is that all the eigenvectors of very large systems are not readily available but a number of the lowest frequency (targeted) modes can be obtained by Lanczos-type method. Even if an algorithm is found which can damp the targeted modes, there is the possibility of destabilizing others. Therefore, the algorithm must have high selectivity. The Multiple Modal Selectivity Method takes advantage of the linear independence of eigenvectors  $\underline{\mathbf{u}}_k$  and its relationship with the reciprocal base vector,  $\underline{\mathbf{v}}_k$ , in  $\underline{\mathbf{v}}_j^{\mathrm{T}}$   $\underline{\mathbf{u}}_k = \delta_{jk}$  where  $\delta_{jk}$  is the Kronecker delta to establish three levels of selectivity:

- (i) by choice of the generator stations;
- (ii) by the spatial filter which screens the information received from the generator stations;
- (iii) by the relative weights of the commands sent back to the generator stations in feedback response

In addition to the three screenings, the gain, in the Central Control given as  $(2.26) \ \Delta \lambda_{ij(k)} = -\sigma_k(\hat{\underline{v}}_i^T \hat{\underline{u}}_k)(\hat{\underline{v}}_k^T \hat{\underline{u}}_j), \text{ ensures that the eigenvalues of non-targeted modes are shifted to the left of the s-plane, so that there is no possibility of destabilization. This adds a "fail safe" feature to the design which assumes that the non-targeted fast modes will be damped by conventional PSS.$ 

#### 6.2.2 Chapter 3

The claims of chapter 2 have been validated by simulations and eigenvalue analysis. The Multiple Modal Selectivity Method passes the demanding test of maintaining stability after one of the tie-lines of the 12-generator test system is opened.

### 6.2.3 Chapter 4

The archetype model of Figure 4.3 and its close form formulation of its dynamics (equation(4.22)) are applied to represent a sustainable energy technology installation situated in a transmission line between two generators. This research shows that the conclusions of the previous study [65] is not restricted by the assumptions of small signal linearization but are true for large signals as well. The study shows that the difference in damping characteristics of active and reactive power modulation is clearly written in equation(4.22).

## 6.2.4 Chapter 5

The phase-plane diagram identifies the extent of damping in the linear region and in the saturated region. Noting that damping in the linear region will inherently be small, the conclusion is reached that "bang-bang damping" should be the preferred strategy. The research further shows that in linear damping, the energy is dissipated as work (therefore, attenuated with distance). On the other

hand in the nonlinear damping strategy, the energy is depleted as power (therefore, attenuated linearly with time).

#### 6.3 FUTURE WORK

Because the Multiple Modal Selectivity Method is promising, it requires further exhaustive testing, especially by independent researchers. So far, proof of principle is based on 12 and 16-generator systems, as four generators are chosen to damp three selected modes. There is a long way to go to stabilize practical power grids which have thousand or tens of thousands of generators. How many generators should be chosen? What is the MVA requirement to provide adequate damping?

The archetype of Figure 4.3 and equation (4.22) represent a key to many theoretical questions. Numerical methods are powerful in yielding answers. Analytical continuity provides the glue to bond diverse facts.

## APPENDIX

#### APPENDIX A: INVESTIGATION ON GENERATOR MODELING

The purpose of this section is to identify the simplest generator model that can produce effective control strategies for damping inter-area oscillations.

The suitability of different generator models are judged based on the resulting inter-area mode eigenvectors. Four generator models are tested, starting from full model (with all sub-systems) and then removing sub-systems and the generator details, one at a time. By comparing the mode shapes, the simplest model that is still suitable for damping the inter-area oscillations is selected. The tests are separately done for round rotors and salient pole generators. The test system is a 2 area, 4 machines system of [3, 73], with the data taken from MatNetEig toolbox of Matlab [54].

#### Model Descriptions

- Model 1: Includes generator sub-transient reactances, Exciter system, and PSS.
- Model 2: Model 1, less the PSS
- Model 3: Model 2, less the Exciter system
- Model 4: Model 3, less the generator sub-transient reactance (classical model).

In the table below, variables defining generator internal dynamic for different models are listed.

Table A.1

State Name	Model 1	Model 2	Model 3	Model 4
Angle	X	X	X	X
Speed	X	X	X	X
$\Psi_f$	X	X	X	-
$\Psi_d$	X	X	X	-
$oldsymbol{\Psi}_{kq1}$	X	X	X	-
$oldsymbol{\psi}_{kq2}$	X	X	X	-
PSSst1	X	-	-	-
PSSst2	X	-	-	-
PSSst3	X	-	-	-
Transducer	X	X	-	-
$A VR_2$	X	X	-	-

## Mode Shape for Different Generator Models – Round Rotor (RR) Case:

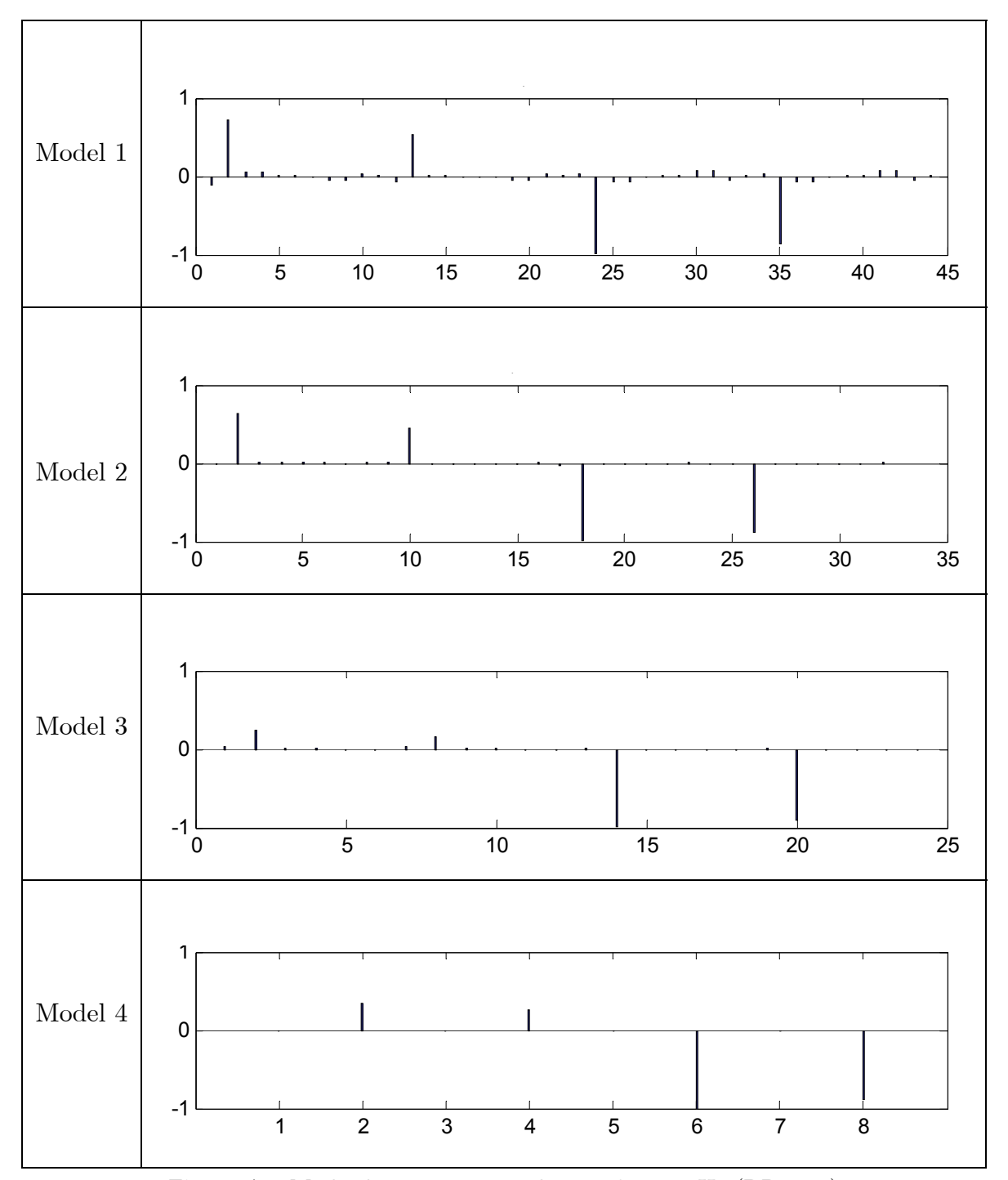


Figure A.1 Mode shapes corresponding to  $f_1$ =0.54 Hz (RR case)

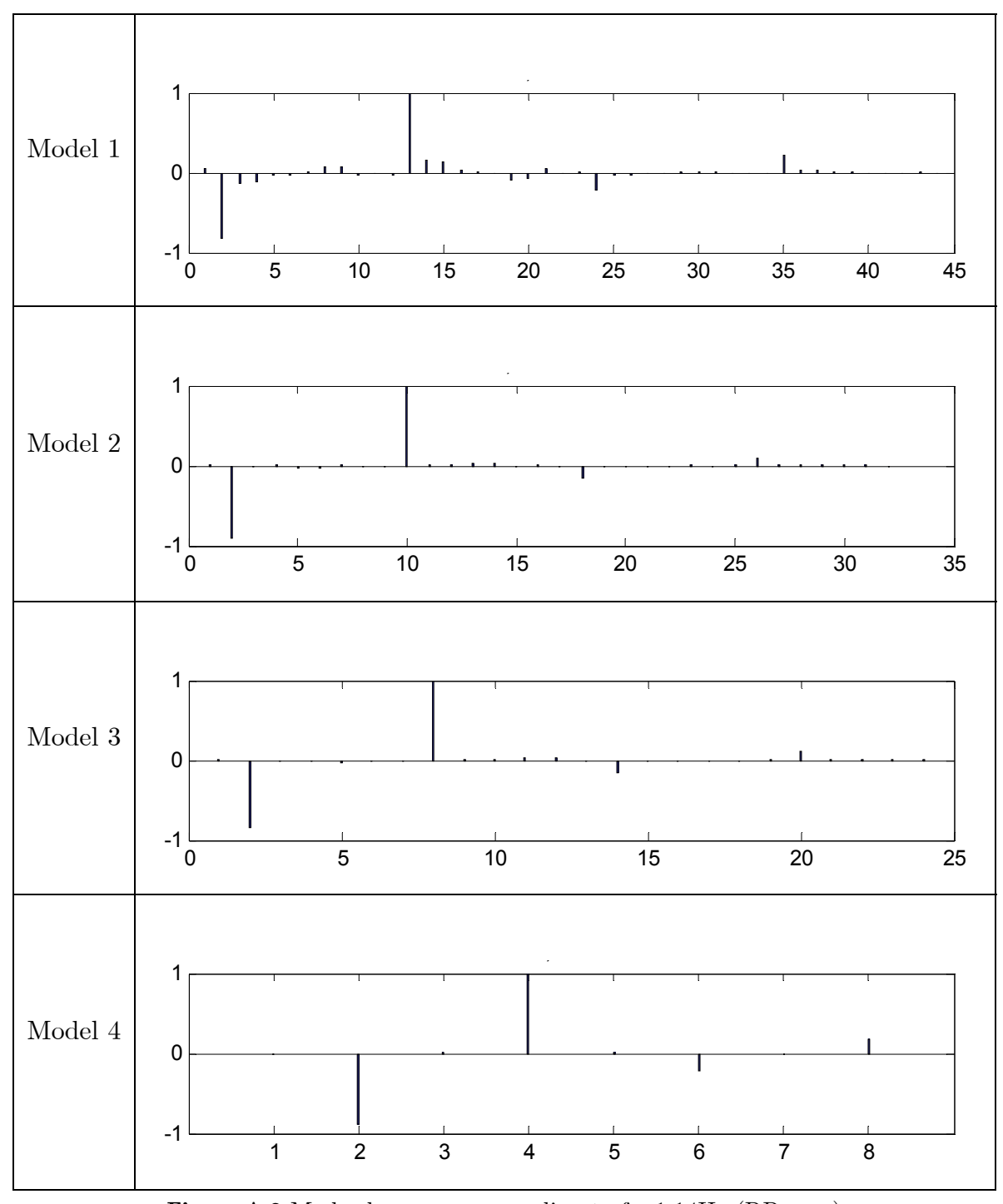


Figure A.2 Mode shapes corresponding to  $f_2=1.14 \mathrm{Hz}$  (RR case)

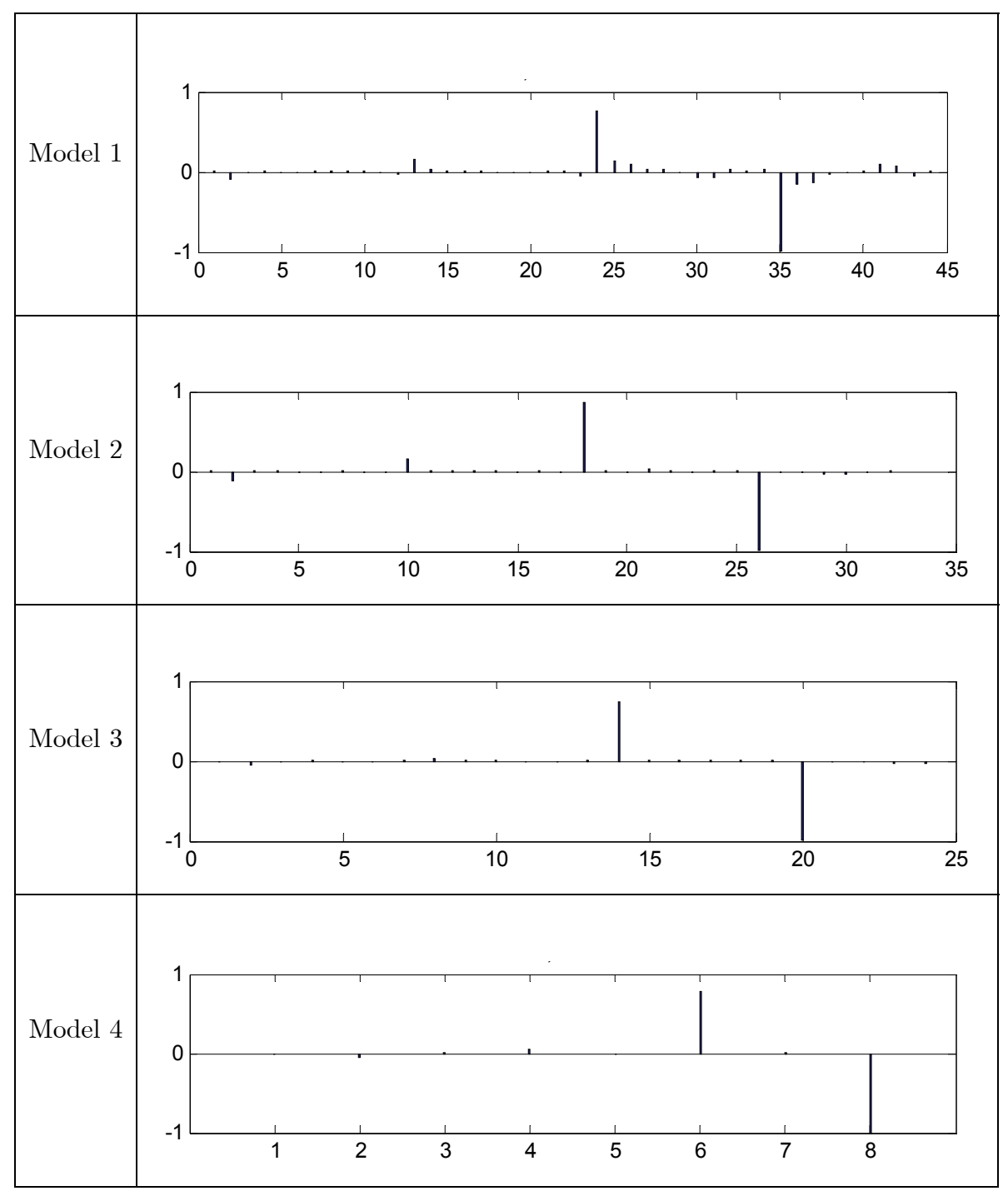


Figure A.3 Mode shapes corresponding to  $f_3=1.18~\mathrm{Hz}$  (RR case)

## Mode Shape for Different Generator Models – Salient Pole(SP) Case:

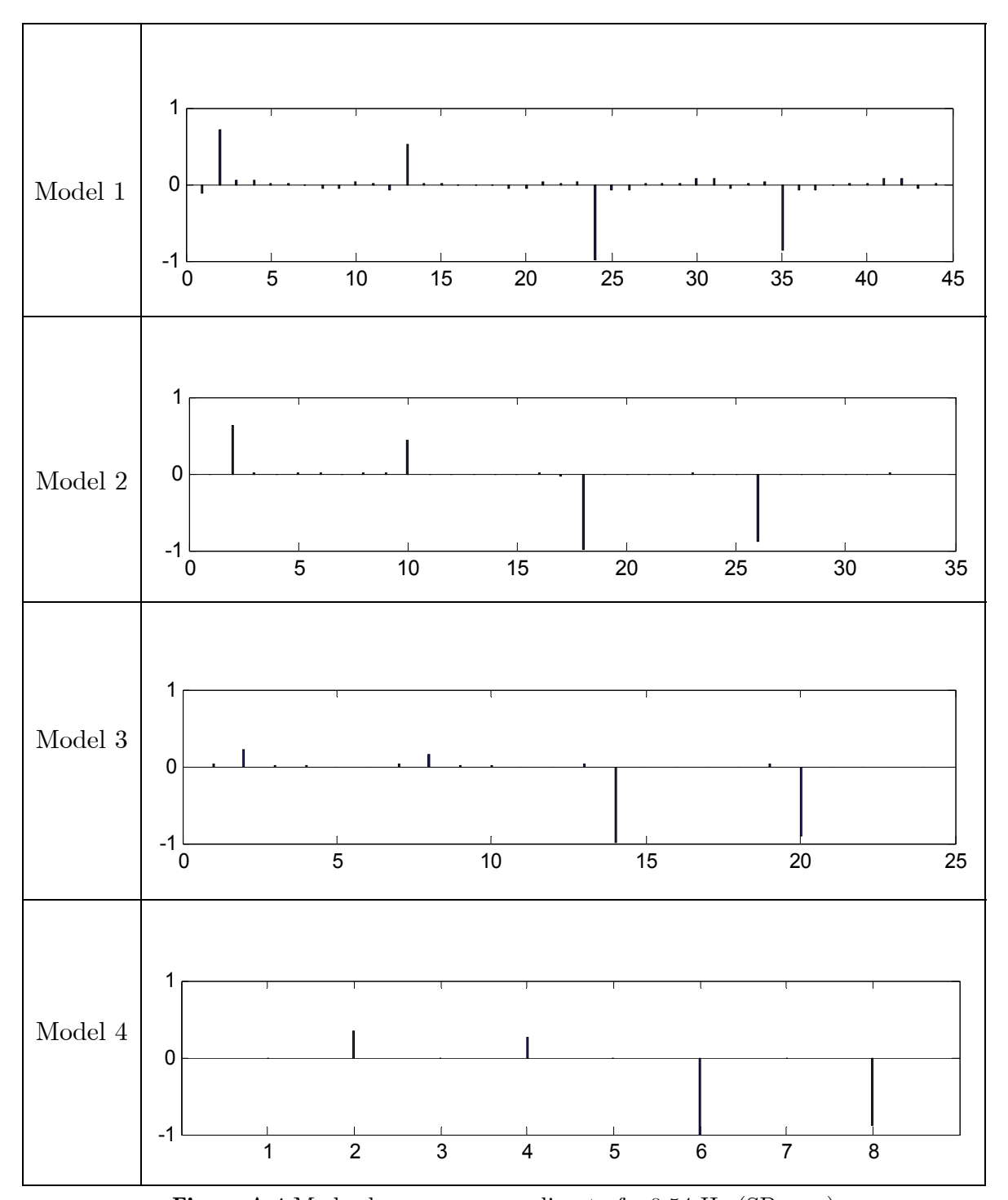


Figure A.4 Mode shapes corresponding to  $f_1$ =0.54 Hz (SP case)

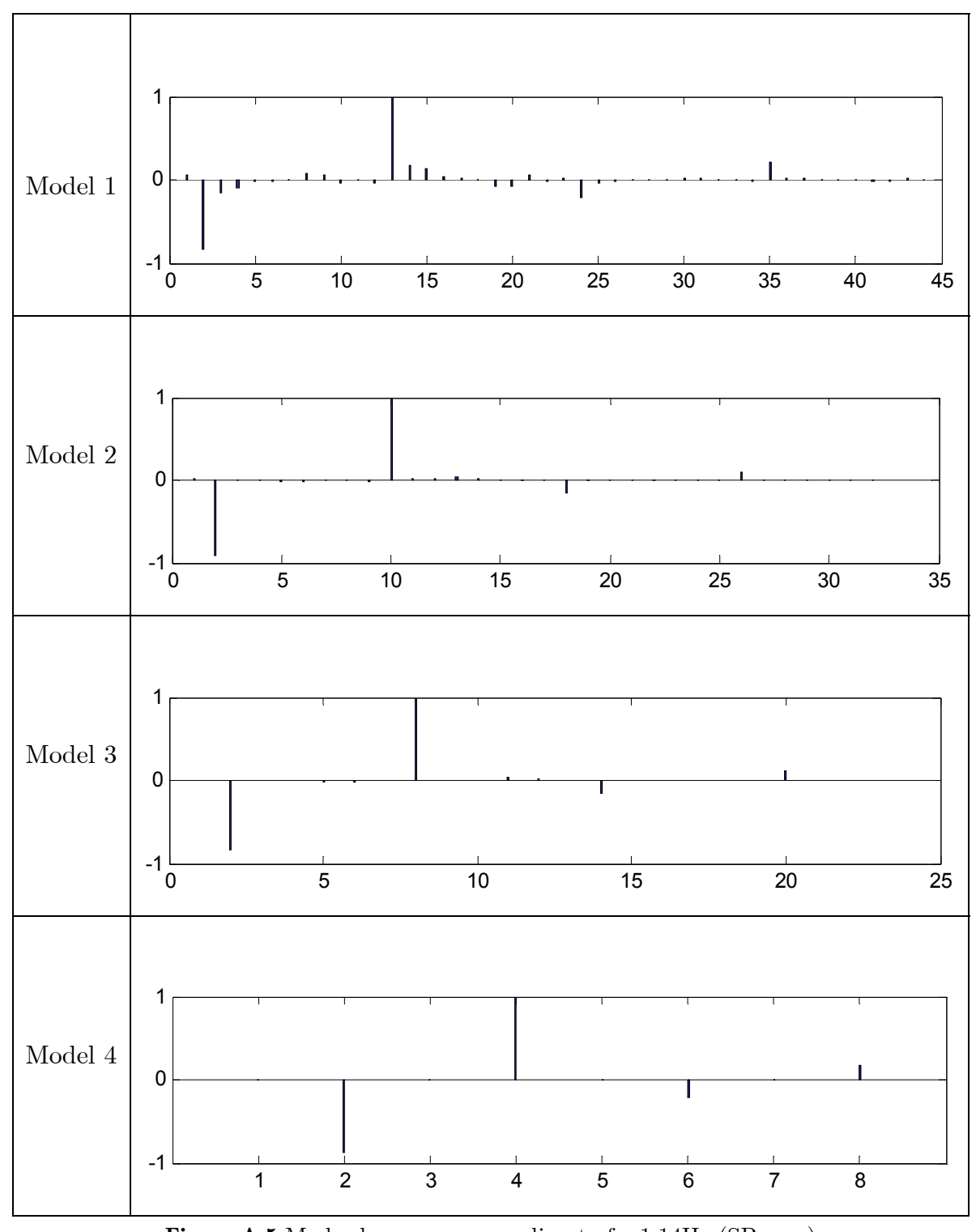


Figure A.5 Mode shapes corresponding to  $f_2=1.14 Hz$  (SP case)

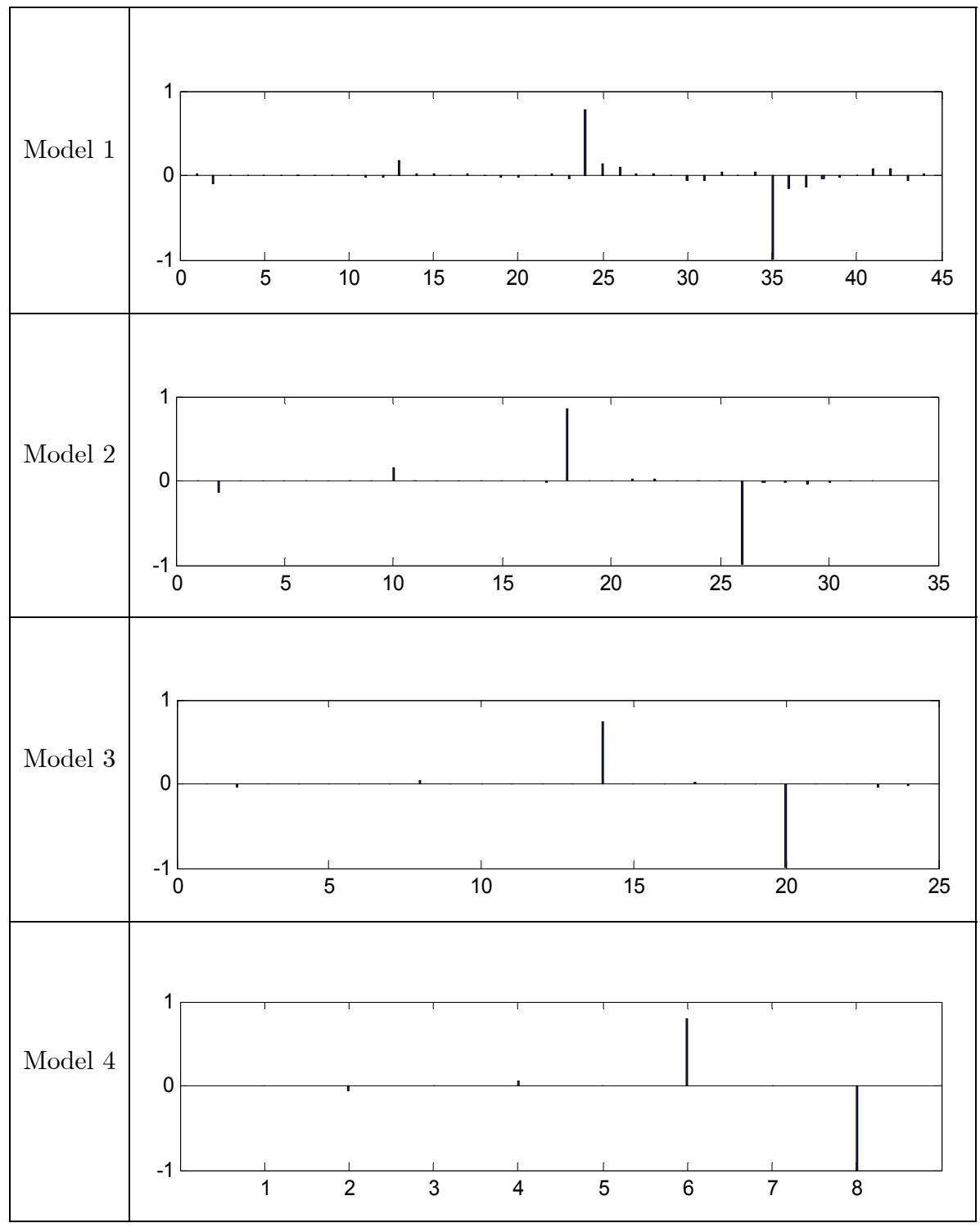


Figure A.6 Mode shapes corresponding to  $f_3{=}1.18~\mathrm{Hz}$  (SP case)

Comparing Figures Figure A.1 to Figure A.6 one can conclude:

- Regardless of the model used, components of the eigenvectors associated with rotor speeds are the dominant ones;
- For different models, relative magnitudes of the speed components change little;
- As expected, the generator rotor type (round or salient pole) has little impact on the results, as their associated damper windings respond only to fast transients.

The above results largely remain unchanged when the study is repeated with the participation factors.

## **APPENDIX B:** INFORMATION REGARDING VALIDATION TEST

 ${\bf Table~B.1~Generator~parameters}$ 

Base MVA	504	Base Voltage (kV)	20
H (s)	3.1	Ra (p.u.)	0.002
Xd (p.u.)	1.05	Xq (p.u.)	0.686
Xd' (p.u.)	0.25	Xq' (p.u.)	0.228
Xd" (p.u.)	0.15	Xq" (p.u.)	0.12
Td' (s)	7.6	Tq' (s)	0.85
Td" (s)	0.03	Tq" (s)	0.03

- Transformers: Primary voltage: 20kV, Secondary Voltage: 115kV, connection:  $\Delta/Y$ .

Table B.2 Generation and Load powers

Genera	ntion	Load		
$P_{m1}$ (MW)	400	${ m P}_{ m d1}~({ m MW})$	300	
$ ho_{ m m2}~({ m MW})$	80	${f P}_{ m d2}~({ m MW})$	300	
P <sub>C0</sub> (MW)	120	-	-	

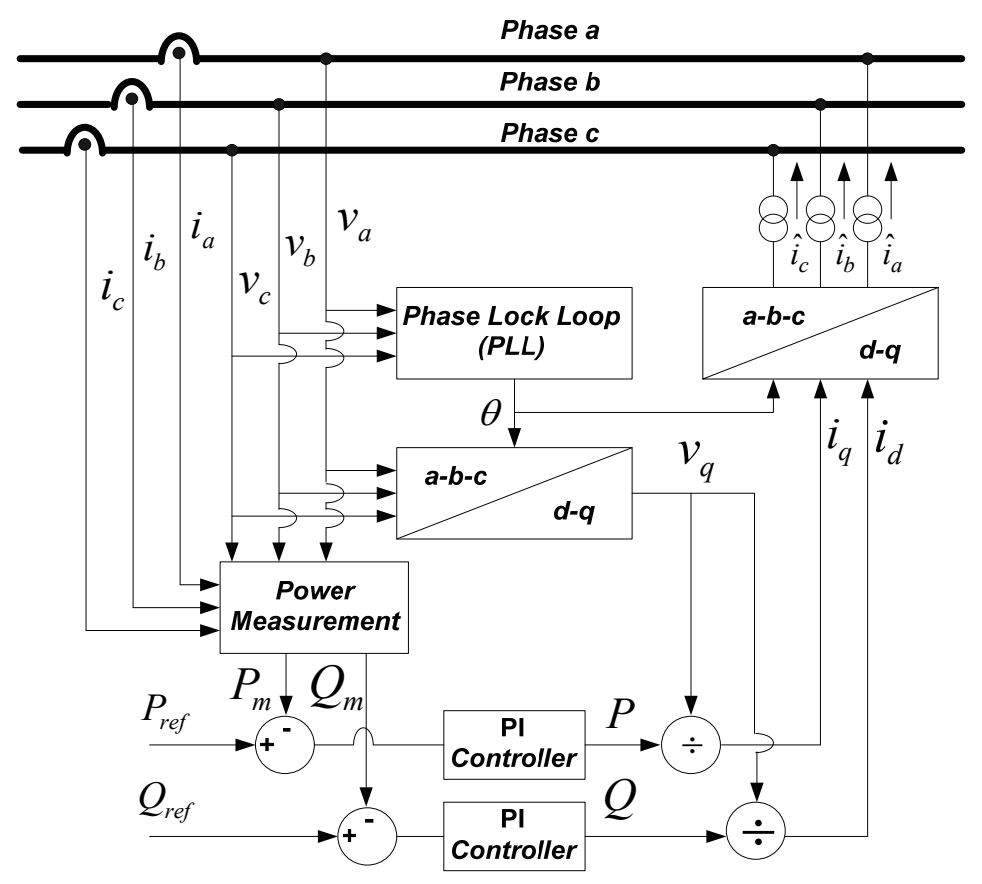


Figure B.1 Block diagram of S-Modulator

The S-Modulator [86], which models the wind farm, is integrated in HYPERSIM. The frequency deviation  $\omega_{1\text{-}2}$ , is measured by the Phase Lock Loop (PLL) of HYPERSIM. The feedback signal  $\omega_{1\text{-}2}$ , is applied to form the complex power references:  $P_{\text{ref}} = P_{\text{C0}} + K_{\text{P}}\omega_{1\text{-}2}$ , and  $Q_{\text{ref}} = Q_{\text{C0}} + K_{\text{Q}}\omega_{1\text{-}2}$ . Saturation limits can be set.

## REFERENCES

- [1] "First Report of Power System Stability," American Institute of Electrical Engineers, Transactions of the, vol. 56, pp. 261-282, 1937.
- [2] C. Concordia, "Steady-State Stability or Synchronous Machines as Affected by Voltage-Regulator Characteristics," American Institute of Electrical Engineers, Transactions of the, vol. 63, pp. 215-220, 1944.
- [3] G. Rogers, *Power system oscillations*: Kluwer Academic Pub, 2000.
- [4] A.J. Germond and R. Podmore, "Dynamic aggregation of generating unit models," *IEEE Transactions on Power Apparatus and Systems*, pp. 1060-1069, 1978.
- [5] M. Klein, G. Rogers, and P. Kundur, "A fundamental study of inter-area oscillations in power systems," *IEEE Transactions on Power Systems*, vol. 6, pp. 914-921, 1991.
- [6] B. Pal and B. Chaudhuri, *Robust control in power systems*: Springer Verlag, 2005.
- [7] V. Arcidiacono, E. Ferrari, R. Marconato, J.D. Ghali, D. Grandez, and DSRCRA ENEL, "Evaluation and improvement of electromechanical oscillation damping by means of eigenvalue-eigenvector analysis. Practical results in the central Peru power system," *IEEE Transactions on Power Apparatus and Systems*, pp. 769-778, 1980.
- [8] The integrated North American electricity market: Energy security: A
  North American concern [Online]. Available:
  http://www.canelect.ca/en/Pdfs/3395\_CEA\_NA\_paper\_EN\_Final.pdf
- [9] R. Piwko, R. DeMello, R. Gramlich, W. Lasher, D. Osborn, C. Dombek, and K Porter, "What comes first?," *IEEE Power and Energy Magazine*, vol. 5, pp. 68-77, 2007.
- [10] I. Kamwa, R. Grondin, D. Asber, J.P. Gingras, and G. Trudel, "Active-power stabilizers for multimachine power systems: challenges and prospects," *IEEE Transactions on Power Systems*, vol. 13, pp. 1352-1358, 1998.

- [11] J.H. Chow, J.J. Sanchez-Gasca, H. Ren, and S. Wang, "Power system damping controller design-using multiple input signals," *IEEE Control Systems Magazine*, vol. 20, pp. 82-90, 2000.
- [12] G. Asplund, "Application of HVDC Light to power system enhancement," in *Power Engineering Society Winter Meeting*, 2000. IEEE, 2000, pp. 2498-2503 vol.4.
- [13] Li Guo-Jie, Ruan Siye, Peng Lin, Sun Yuanzhang, and Li Xiong, "A novel nonlinear control for stability improvement in HVDC light system," in *Power Engineering Society General Meeting*, 2005. IEEE, 2005, pp. 837-845 Vol. 1.
- [14] N. Flourentzou, V. G. Agelidis, and G. D. Demetriades, "VSC-Based HVDC Power Transmission Systems: An Overview," *Power Electronics*, *IEEE Transactions on*, vol. 24, pp. 592-602, 2009.
- [15] Z. Huang, B. T. Ooi, L. A. Dessaint, and F. D. Galiana, "Exploiting voltage support of voltage-source HVDC," *Generation, Transmission and Distribution, IEE Proceedings*-, vol. 150, pp. 252-256, 2003.
- [16] W. Long and S. Nilsson, "HVDC transmission: yesterday and today," Power and Energy Magazine, IEEE, vol. 5, pp. 22-31, 2007.
- [17] V.K. Sood, HVDC and FACTS controllers: applications of static converters in power systems: Kluwer Academic Pub, 2004.
- [18] Y. Mansour, W. Xu, F. Alvarado, C. Rinzin, "SVC placement using critical modes of voltage instability," *IEEE Transactions on Power Systems*, vol. 9, pp. 757-763, 1994.
- [19] E.V. Larsen and J.H. Chow, "SVC control design concepts for system dynamic performance," *IEEE Power Engineering Society Publication* 87TH0187-5-PWR Application of Static Var Systems for System Dynamic Performance, 1987.
- [20] N. Martins, L.T.G. Lima, "Determination of suitable locations for power system stabilizers and static VAR compensators for damping electromechanical oscillations large scale power systems," *IEEE Transactions on Power Systems*, vol. 5, pp. 1455-1469, 1990.

- [21] S.E.M. De Oliveira, "Synchronizing and damping torque coefficients and power systemsteady-state stability as affected by static VAr compensators," *IEEE Transactions on Power Systems*, vol. 9, pp. 109-119, 1994.
- [22] M. O'Brien and G. Ledwich, "Placement of static compensators for stability improvement," *IEE Proceedings Generation, Transmission and Distribution* [see also IEE Proceedings-Generation, Transmission and Distribution], vol. 132, pp. 30-35, 1985.
- [23] R.M. Mathur and R.K. Varma, Thyristor-based FACTS controllers for electrical transmission systems: IEEE press, 2002.
- [24] N.G. Higorani and L. Gyugyi, "Understanding FACTS Devices," ed: IEEE Press, 2000.
- [25] P. Pourbeik and M.J. Gibbard, "Damping and synchronizing torques induced on generators by FACTSstabilizers in multimachine power systems," *IEEE Transactions on Power Systems*, vol. 11, pp. 1920-1925, 1996.
- [26] J. J. Sanchez-Gasca, "Coordinated control of two FACTS devices for damping interarea oscillations," Power Systems, IEEE Transactions on, vol. 13, pp. 428-434, 1998.
- [27] K. Clark, B. Fardanesh, and R. Adapa, "Thyristor controlled series compensation application study-control interaction considerations," *Power Delivery, IEEE Transactions on*, vol. 10, pp. 1031-1037, 1995.
- [28] E. N. Lerch, D. Povh, and L. Xu, "Advanced SVC control for damping power system oscillations," *Power Systems, IEEE Transactions on*, vol. 6, pp. 524-535, 1991.
- [29] M. M. Farsangi, Y. H. Song, and K. Y. Lee, "Choice of FACTS device control inputs for damping interarea oscillations," *Power Systems, IEEE Transactions on*, vol. 19, pp. 1135-1143, 2004.
- [30] L. Gerin-Lajoie, G. Scott, S. Breault, E. V. Larsen, D. H. Baker, and A. F. Imece, "Hydro-Quebec multiple SVC application control stability study," Power Delivery, IEEE Transactions on, vol. 5, pp. 1543-1551, 1990.

- [31] R. Mihalic, P. Zunko, and D. Povh, "Improvement of transient stability using unified power flow controller," *Power Delivery, IEEE Transactions* on, vol. 11, pp. 485-492, 1996.
- [32] L. Ippolito and P. Siano, "Selection of optimal number and location of thyristor-controlled phase shifters using genetic based algorithms," *IEE Proceedings-Generation, Transmission and Distribution*, vol. 151, pp. 630-637, 2004.
- [33] E.V. Larsen, J.J. Sanchez-Gasca, and J.H. Chow, "Concepts for design of FACTS controllers to damp power swings," *IEEE Transactions on Power Systems*, vol. 10, pp. 948-956, 1995.
- [34] B.K. Kumar, S.N. Singh, and S.C. Srivastava, "Placement of FACTS controllers using modal controllability indices to damp out power system oscillations," *Generation, Transmission & Distribution, IET*, vol. 1, pp. 209-217, 2007.
- [35] F.M. Hughes, O. Anaya-Lara, N. Jenkins, and G. Strbac, "A power system stabilizer for DFIG-based wind generation," *IEEE Transactions on Power Systems*, vol. 21, pp. 763-772, 2006.
- [36] G.L. Johnson, Wind energy systems: Prentice-Hall Englewood Cliffs (NJ), 1985.
- [37] G. Tsourakis, B. M. Nomikos, and C. D. Vournas, "Contribution of Doubly Fed Wind Generators to Oscillation Damping," *Energy Conversion*, *IEEE Transactions on*, vol. 24, pp. 783-791, 2009.
- [38] Y. Zhou, J. A. Ferreira, and P. Bauer, "Grid-connected and islanded operation of a hybrid power system," in *Power Engineering Society Conference and Exposition in Africa*, 2007. PowerAfrica '07. IEEE, 2007, pp. 1-6.
- [39] S. K. Chaudhary, R. Teodorescu, and P. Rodriguez, "Wind Farm Grid Integration Using VSC Based HVDC Transmission - An Overview," in Energy 2030 Conference, 2008. ENERGY 2008. IEEE, 2008, pp. 1-7.
- [40] DOE, NREL, AWEA, B&V et al, "20% Wind Energy by 2030.," DOE/GO-102008-2567, US Department of Energy, May2008.
- [41] L.L. Grigsby, Power system stability and control: CRC Press, 2007.

- [42] J.Y. Cai, Z. Huang, J. Hauer, and K. Martin, "Current status and experience of WAMS implementation in North America," 2005, pp. 1–7.
- [43] John Hauer, F. James Hughes, Daniel Trudnowski, Graham Rogers, John and Louis Scharf Pierre, and Wayne Litzenberger, "A Dynamic Information Manager for Networked Monitoring of Large Power Systems," BPA/PNNL Report WO 8813-01, 1998.
- [44] A.G. Phadke and J.S. Thorp, "History and applications of phasor measurements," 2006, pp. 331-335.
- [45] A.G. Phadke, "Synchronized phasor measurements in power systems," IEEE Computer Applications in Power, vol. 6, pp. 10-15, 1993.
- [46] I. Kamwa and R. Grondin, "PMU configuration for system dynamic performance measurement inlarge, multiarea power systems," *IEEE Transactions on Power Systems*, vol. 17, pp. 385-394, 2002.
- [47] I. Kamwa, R. Grondin, and Y. Hebert, "Wide-area measurement based stabilizing control of large powersystems-a decentralized/hierarchical approach," *IEEE Transactions on Power Systems*, vol. 16, pp. 136-153, 2001.
- [48] C.W. Taylor, D.C. Erickson, K.E. Martin, R.E. Wilson, and V. Venkatasubramanian, "WACS-wide-area stability and voltage control system: R&D and online demonstration," *Proceedings of the IEEE*, vol. 93, pp. 892-906, 2005.
- [49] A.A. Fouad and V. Vittal, Power system transient stability analysis using the transient energy function method: Prentice Hall PTR, 1992.
- [50] P.W. Sauer and M.A. Pai, *Power system dynamics and stability*: Prentice Hall, 1998.
- [51] P.V. Subramanian, K. Parthasarathy, and B.N.N. Iyengar, "Development of improved Lyapunov functions for transient power system stability study," *International journal of systems science*, vol. 1, pp. 143-151, 1970.
- [52] Simulink-Simulation and Model-Based Design. Available: http://www.mathworks.com/products/simulink/
- [53] SimPowerSystems5.2.Available: http://www.mathworks.com/products/simpower/

- [54] Available: http://www.eagle.ca/~cherry/MatNetEig.htm
- [55] P. Kundur, M. Klein, G. J. Rogers, and M. S. Zywno, "Application of power system stabilizers for enhancement of overall system stability," *Power Systems, IEEE Transactions on*, vol. 4, pp. 614-626, 1989.
- [56] IEEE Committee Report, "Proposed Excitation System Definitions for Synchronous Machines," *Power Apparatus and Systems, IEEE Transactions on*, vol. PAS-88, pp. 1248-1258, 1969.
- [57] "Dynamic models for fossil fueled steam units in power system studies," Power Systems, IEEE Transactions on, vol. 6, pp. 753-761, 1991.
- [58] IEEE Committee Report, "Dynamic Models for Steam and Hydro Turbines in Power System Studies," *Power Apparatus and Systems, IEEE Transactions on*, vol. PAS-92, pp. 1904-1915, 1973.
- [59] TransEnergie, Hydro-Quebec group, "HYPERSIM 8.9 reference guide manual," p. 208, June 2002.
- [60] G.J. Thaler and R.G. Brown, Analysis and design of feedback control systems: McGraw-Hill, New York, 1960.
- [61] G.H. Golub and C.F. Van Loan, *Matrix computations*: Johns Hopkins Univ Pr, 1996.
- [62] N. Uchida and T. Nagao, "A new eigen-analysis method of steady-state stability studies for large power systems: S matrix method," *IEEE Transactions on Power Systems*, vol. 3, pp. 706-714, 1988.
- [63] L. Rouco, "Eigenvalue-based methods for analysis and control of power systemoscillations," 1998, p. 3.
- [64] Weixing Lu and Boon-Teck Ooi, "Optimal acquisition and aggregation of offshore wind power by multiterminal voltage-source HVDC," *Power Delivery, IEEE Transactions on*, vol. 18, pp. 201-206, 2003.
- [65] S.Y. Ruan, G.J. Li, B.T. Ooi, and Y.Z. Sun, "Power system damping from real and reactive power modulations of voltage-source-converter station," Generation, Transmission & Distribution, IET, vol. 2, pp. 311-320, 2008.
- [66] IEEE Power System Engineering Committee, "Eigenanalysis and frequency domain methods for system dynamic performance," *IEEE Publication* 90TH0292-3-PWR, 1989.

- [67] B.T. Ooi and M. Nishimoto, "Analytical structures for eigensystem study of power flowoscillations in large power systems," *IEEE Transactions on Power Systems*, vol. 3, pp. 1609-1615, 1988.
- [68] C.M. Lin, V. Vittal, W. Kliemann, and A.A. Fouad, "Investigation of modal interaction and its effects on controlperformance in stressed power systems using normal forms of vectorfields," *IEEE Transactions on Power* Systems, vol. 11, pp. 781-787, 1996.
- [69] I.J. Perez-Arriaga, G.C. Verghese, and F.C. Schweppe, "Selective modal analysis with applications to electric power systems, Part I: Heuristic introduction," *IEEE Transactions on Power Apparatus and Systems*, pp. 3117-3125, 1982.
- [70] G.C. Verghese, I.J. Perez-Arriaga, and F.C. Schweppe, "Selective modal analysis with applications to electric power systems, Part II: The dynamic stability problem," *IEEE Transactions on Power Apparatus and Systems*, pp. 3126-3134, 1982.
- [71] I. Kamwa. Performance of three PSSs for Inter-area Oscillations. SymPowerSystems toolbox.
- [72] "Singular Perturbations, Coherency and Aggregation of Dynamic Systems," *GE final report*, pp. 6-42, July 1981.
- [73] P. Kundur, N.J. Balu, and M.G. Lauby, *Power system stability and control*: McGraw-Hill Professional, 1994.
- [74] R.D. Fernandez, R.J. Mantz, and P.E. Battaiotto, "Contribution of wind farms to the network stability," 2006, p. 6.
- [75] E. Muljadi, C.P. Butterfield, B. Parsons, and A. Ellis, "Effect of variable speed wind turbine generator on stability of a weak grid," *IEEE Transaction on Energy Conversion*, vol. 22, pp. 29-36, 2007.
- [76] N.R. Ullah and T. Thiringer, "Variable speed wind turbines for power system stability enhancement," *IEEE Transaction on Energy Conversion*, vol. 22, pp. 52-60, 2007.
- [77] J.F. Conroy and R. Watson, "Frequency response capability of full converter wind turbine generators in comparison to conventional generation," *IEEE Transactions on Power Systems*, vol. 23, p. 649, 2008.

- [78] J.B. Ekanayake, L. Holdsworth, X.G. Wu, and N. Jenkins, "Dynamic modeling of doubly fed induction generator wind turbines," *IEEE Transactions on Power Systems*, vol. 18, pp. 803-809, 2003.
- [79] Z. Lubosny and J. W. Bialek, "Supervisory Control of a Wind Farm," Power Systems, IEEE Transactions on, vol. 22, pp. 985-994, 2007.
- [80] D. Gautam, V. Vittal, and T. Harbour, "Impact of Increased Penetration of DFIG-Based Wind Turbine Generators on Transient and Small Signal Stability of Power Systems," Power Systems, IEEE Transactions on, vol. 24, pp. 1426-1434, 2009.
- [81] F. De Leon and B.T. Ooi, "Damping power system oscillations by unidirectional control of alternative power generation plants," in *Power Engineering Society Winter Meeting*, 2001. IEEE, 2001, pp. 747-752 vol.2.
- [82] Ping-Kwan Keung, Pei Li, H. Banakar, and Boon-Teck Ooi, "Kinetic Energy of Wind-Turbine Generators for System Frequency Support," Power Systems, IEEE Transactions on, vol. 24, pp. 279-287, 2009.
- [83] J. Morren, S. W. H. de Haan, W. L. Kling, and J. A. Ferreira, "Wind turbines emulating inertia and supporting primary frequency control," *Power Systems, IEEE Transactions on*, vol. 21, pp. 433-434, 2006.
- [84] B. Mwinyiwiwa, Z. Wolanski, and B.T. Ooi, "High power switch mode linear amplifiers for flexible ACtransmission system," *IEEE Transactions* on Power Delivery, vol. 11, pp. 1993-1998, 1996.
- [85] T. Smed and G. Andersson, "Utilizing HVDC to damp power oscillations," Power Delivery, IEEE Transactions on, vol. 8, pp. 620-627, 1993.
- [86] C. Luo and B.T. Ooi, "Frequency deviation of thermal power plants due to wind farms," *IEEE Transaction on Energy Conversion*, vol. 21, pp. 708-716, 2006.
- [87] H.G. Far; Banakar, H.; Pei Li; Changling Luo; Boon-Teck Ooi; , "Damping Interarea Oscillations by Multiple Modal Selectivity Method," Power Systems, IEEE Transactions on , vol.24, no.2, pp.766-775, May 2009.